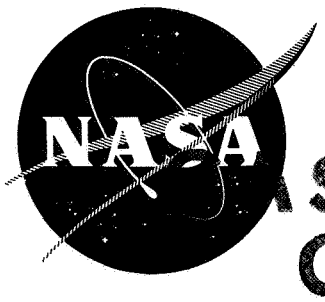

CONTRACTOR REPORT

THE EFFECT OF PERIODIC SHOCK-FRONTED PRESSURE WAVES ON THE INSTANTANEOUS HEAT FLUX AT THE END-WALL OF A TUBE

by

Raymond W. Goluba

prepared for

NATIONAL AERONAUTICS AND SPACE ADMINISTRATION

August 1, 1968

Contract NsG-601

Technical Management
NASA Lewis Research Center
Cleveland, Ohio
Chemistry and Energy Conversion Division
Paul R. Wieber

THE UNIVERSITY OF WISCONSIN
DEPARTMENT OF MECHANICAL ENGINEERING
Madison, Wisconsin

THE EFFECT OF PERIODIC SHOCK-FRONTED PRESSURE WAVES ON THE INSTANTANEOUS HEAT FLUX AT THE END-WALL OF A TUBE

Raymond W. Goluba

Under the Supervision of Associate Professor Gary L. Borman

ABSTRACT

Instantaneous heat flux rates were measured at the end-wall of a tube in which shock-fronted, longitudinal pressure waves were generated. Pressure oscillations with frequencies of 479-881 Hz, amplitudes up to 175 psi peak-to-peak, and average tube pressures from 40 to 190 psia were obtained. The heat flux was calculated from the surface temperature of the end-wall as measured by a thin platinum resistance film deposited on a Pyrex surface inserted into the end-wall.

The instantaneous flux was found to be large compared to the time average heat transfer rate. The instantaneous rates increased with increasing pressure ratio and were proportional to the square root of the product of the wave frequency and the time-averaged pressure of the oscillations.

A one-dimensional model was solved numerically for the case of zero net heat transfer to the end-wall. The calculations agreed with the experimentally observed trends and correctly predicted the shape of the periodic portion of the flux.

SUMMARY

This experimental investigation is concerned with the instantaneous heat flux rates at the end-wall of a tube in which shock-fronted, longitudinal pressure waves have been generated. Pressure oscillations in a frequency range of 479-881 Hz, with amplitudes up to 175 psi peak-to-peak, were obtained with time-averaged tube pressures from 40 to 190 psia.

The pressure waves were generated by periodically interrupting the inlet air flow to a resonant circular tube by means of a rotating siren disk so that periodic shock-fronted waves were formed. The air flow was bled from the periphery of the tube through a thin gap that was maintained between the open end of the tube and a flat plate located perpendicular to the tube axis. This plate forms the end-wall on which the instantaneous heat transfer was studied. The instantaneous heat flux at the center of the end-wall was calculated from the surface temperature oscillation as measured by a thin platinum resistance film deposited on a Pyrex surface inserted into the end-wall.

At the center of the end plate the fluid flow was not appreciably affected by the air bleed at the tube circumference. Therefore, the flow at the end-wall was similar to that which occurs at the end of a rarefaction wave tube, except that the wave was repetitive. The velocity fluctuations of the gas were assumed normal to the end-wall, and a one-dimensional analysis was performed to predict the instantaneous heat flux at the center of the end-wall.

The thermal boundary layer was thin, compared to the wavelength of the oscillation, permitting the pressure to be assumed independent of the distance from the end-wall and therefore a function of time alone. The pressure variation with time was provided from the experimental data. The thermophysical properties were assumed constant throughout the boundary layer. The gas temperature was assumed to fluctuate isentropically at the outer edge of the boundary layer and assumed to be constant at the end-wall surface.

The unsteady energy equation was numerically solved by a finite difference predictor-corrector method for the case of a zero net heat transfer at the end-wall. Both the theory and experimental data show that the instantaneous heat flux rates increase as the pressure ratio across the wave increases and are directly proportional to the square root of the product of the frequency and the time-averaged pressure of the oscillation. Both theory and experiment also showed that the maximum heat flux rate is concomitant with the pressure shock front and without measurable time lag between the two events. The theoretical calculations and experimental data were found to agree well for the range of conditions studied.

ACKNOWLEDGMENTS

This thesis would not have been possible without the efforts of many individuals and the financial support supplied by the National Aeronautics and Space Administration under Grant Number NsG-601. The author wishes to express his appreciation ...

To Professors G.L. Borman, P.S. Myers, and O.A. Uyehara, who obtained the NASA grant and initiated the project. Their advice throughout this project proved to be invaluable. Special recognition is due Professor Borman, who served as this author's major professor, for his supervision and encouragement. His suggestions with regard to the theoretical model were appreciated.

To P.R. Wieber of the Lewis Research Center, who acted as the NASA contract monitor.

To W.N. Hauser for maintaining the well-equipped machine shop in which this apparatus took form.

To M. Swenby, a skilled machinist, who was responsible for the machining of all the components of the experimental apparatus.

To J.M. Dunigan for his frequent assistance and advice concerning the experimental equipment.

To H.G. Weber, who helped with the instrumentation and all of the data taking, and in whose capable hands the author leaves the experimental apparatus.

To my wife Diane for her patience, understanding, and help throughout this undertaking.

And finally, to the many graduate students and faculty members in the Mechanical Engineering Department at the University of Wisconsin.

TABLE OF CONTENTS

CHAPTER PAGE

LIST OF FIGURES

FIGURE PAGE

FIGURE PAGE

FIGURE PAGE

NOMENCLATURE

a	speed of sound, ft/sec.
B	defined by Eq. 5-26, dimensionless.
BC	defined by Eq. 5-27, dimensionless.
c	specific heat for a solid, BTU/lb_m-°F.
C_l	a constant for a particular wave shape, dimensionless.
c_p	specific heat at constant pressure, BTU/lb_m-°F.
f	frequency, Hz.
g	plate gap thickness, in.
h	heat transfer coefficient, BTU/hr-ft^2-°F.
k	thermal conductivity, BTU/hr-ft-°F.
k_∞	thermal conductivity of the gas at the outer edge of the thermal boundary layer, BTU/hr-ft-°F.
ℓ	slab thickness, in.
L_r	resonant tube length, in.
$\dot{P}$	time rate of change of pressure (dP/dt), psi/sec.
P	instantaneous gas pressure, psia.
ΔP	amplitude of the pressure wave, psi.
$\bar{P}$	time-averaged tube pressure, psia.
P_m	maximum gas pressure in the cycle, psia.
P_0	minimum gas pressure in the cycle, psia.
P_r	pressure ratio across the wave (P_m/P_0), dimensionless.
P_s	upstream air pressure adjacent to the siren disk,psia.
P_{ti}	ratio of average tube pressure to average siren inlet pressure, dimensionless.

Q_{pos}	defined by Eq. 4-8, BTU/ft^2.
q_w	heat flux at the wall, BTU/sec-ft^2.
r	$\alpha\Delta t/(\Delta x)^2$, dimensionless.
r_t	tube radius, in.
$\mathcal{r}$	radius, in.
R	specific gas constant, ft-lb$_f$/lb$_m$-°R.
SPL	sound pressure level, db.
t	time, sec.
Δt	time increment, sec.
t_p	period of the pressure oscillation (1/f), sec.
T	temperature, °R.
$\bar{T}$	time-average of the surface temperature fluctuation, °R.
T_d	temperature defined in Fig. 6-8, °R.
T_0	minimum gas temperature in the cycle, °R.
T_q	an average gas temperature defined in Fig. 3-12, °R.
T_w	wall temperature, °R.
T_∞	isentropic gas temperature outside the thermal boundary layer, °R.
$\bar{T}_\infty$	average isentropic gas temperature outside the thermal boundary layer, °R.
u	gas velocity normal to the test plate, ft/sec.
x	distance measured from the test plate, in.
Δx	distance increment, in.
x_ℓ	control volume thickness, in.
$x_{\ell max}$	maximum control volume thickness, in.
y	$(T/T_0)(P/P_0)^{\frac{1-\gamma}{\gamma}}$, dimensionless.
z	x/δ, dimensionless.

Δz	normalized distance increment, dimensionless.
z_ℓ	normalized control volume thickness, dimensionless.
α	thermal diffusivity, $in.^2/sec.$
α_0	$k/(c_p\rho_0)$, $in.^2/sec.$
δ	defined by Eq. 5-14, in.
$\dot{\delta}$	time rate of change of δ ($d\delta/dt$), in./sec.
δ_0	defined by Eq. 5-15, in.
γ	ratio of specific heats (c_p/c_v), dimensionless.
ρ	gas density, lb_m/ft^3.
ρ_∞	gas density at the outer edge of the thermal boundary layer, lb_m/ft^3.
ρ_0	gas density evaluated at (T_0,P_0), lb_m/ft^3.
τ	normalized time (tf), dimensionless.
$\Delta\tau$	normalized time increment, dimensionless.
τ_c	normalized time in the cycle when the heat transfer rate is zero, dimensionless.

Subscripts

i	index for finite difference distance increment.
j	index for finite difference time increment.

INTRODUCTION

In recent years an interest has developed in understanding the effects of pressure oscillations on forced convection heat transfer. This interest has been motivated by the observed increase in the average heat transfer rates when pressure oscillations are imposed on the flowing fluid. For example, it has been found that the pressure oscillations in a rocket combustion chamber experiencing unstable combustion can cause as much as a three-fold increase in the average heat transfer rate to the combustion chamber walls.

The present heat transfer investigation was undertaken to provide information on the instantaneous heat flux from a gas in which the fluctuating pressure waves are of a shape and frequency encountered during combustion instability in rocket engines. It is therefore appropriate that the general problem of combustion instability be briefly discussed.

Combustion instability is characterized by extreme pressure oscillations in the combustion chamber that often are as large as ± 50-100 percent of the mean chamber pressure (Berman, Bollinger, Zucrow). The severe mechanical vibrations from these oscillations can structurally damage the rocket. In addition, the increase in the heat flux at the chamber walls may cause the wall temperature to reach the melting point. Pressure oscillations of this magnitude cannot be

tolerated in the operation of a rocket engine and must be eliminated before the engine can be used in flight.

The oscillations can occur at low frequencies (< 100 Hz, called "chugging"), as well as at high frequencies (> 500 Hz, called "screaming"). The pressure wave shapes are generally of two types - sinusoidal and steep-fronted. As might be expected, the steep-fronted waves are the more damaging. Such high frequency oscillations can occur in any one of four acoustic modes - longitudinal, transverse, radial, and mixed.

Low frequency instability is well understood as being caused by the interaction between the injection system dynamics and the dynamic response of the combustion chamber pressure to propellant flow variations (Barrere, Sutton). The high frequency instabilities are not as well understood, but have been found to be attributable to the combustion process itself (Priem; Crocco, 1964).

As far as this author is aware, all of the previous investigations into the effect of pressure oscillations on heat transfer have been concerned with measuring time-averaged heat transfer rates. However, for the purpose of studying the mechanisms which cause combustion instability, a knowledge of instantaneous heat transfer rates may be helpful. With this in mind, two investigations were undertaken at the University of Wisconsin under NASA sponsorship.

In the first investigation, Wendland measured the instantaneous heat flux at the end of a cylinder in which

pressure oscillations were imposed by a piston. The pressure oscillations were of a sinusoidal type with an amplitude of 400 psi and a frequency range of 15-58 Hz.

In the present investigation an apparatus was designed and built to generate longitudinal shock-fronted pressure waves in a tube at frequencies up to 1080 Hz. The standing pressure waves were produced in a resonant tube by periodically interrupting the air flow from a converging nozzle inlet by means of a rotating siren disk. The air flow was bled from the periphery of the tube through a thin gap that was maintained between the open end of the tube and a flat plate located perpendicular to the tube axis. This plate formed the end-wall on which the instantaneous heat flux was measured.

The text which follows begins with a survey of the literature on the effect of both small and large amplitude pressure waves on the time-averaged heat flux. This is followed by a description of the experimental apparatus that was used in the present investigation, along with a discussion of its performance. A theoretical model for predicting instantaneous heat transfer rates is then described, the resulting solutions are compared with the experimental data, and the conclusions are discussed. Finally, recommendations for future work are presented.

CHAPTER ONE

SURVEY OF THE LITERATURE

The purpose of this chapter is to acquaint the reader with the literature pertinent to this investigation that exists concerning heat transfer in oscillating flows. For a more detailed treatment, the reader is referred to a recent publication by Bogdanoff which contains an extensive survey of the literature. The chapter concludes with a short discussion of the similarities in the flow conditions at the end-wall of a shock tube and a rarefaction wave tube to the flow conditions in the present investigation.

1-1 FORCED CONVECTION - SMALL PRESSURE AMPLITUDES

A substantial amount of heat transfer data has been obtained at pressure amplitudes on the order of one psi peak-to-peak for both internal flows (inside tubes) and external flows (over flat plates). Hwu acoustically induced pressure oscillations in a double pipe heat exchanger at frequencies from 198-322 Hz, with Reynolds numbers of 800-6000. The heat transfer coefficient was found to increase (up to 50 percent) with the frequency and amplitude of the pressure fluctuations. Chalitbhan obtained a 100 percent increase in the heat transfer coefficient by

introducing the pulsations from two air compressors into a double pipe heat exchanger. Although the frequency of the oscillations was low (3-15 Hz), the Reynolds number range was large (7000-200,000).

Investigations at the Georgia Institute of Technology by Spurlock, Jackson, Eastwood, Purdy, and others have been extensive. Sinusoidal pressure oscillations were imposed on air flowing at near atmospheric pressure in a resonant isothermal tube by pointing a driver and horn into the downstream end of the tube. Frequencies in the range of 150-350 Hz were used - with pressure amplitudes on the order of one psi peak-to-peak. The local heat transfer coefficient was found to vary periodically between the nodes and antinodes of the resonant sound wave. Two regimes of heat transfer were discovered. In the first regime, which occurred at Reynolds numbers less than 20,000, the maximum coefficient occurred at the velocity antinodes - while the minimum heat transfer coefficient occurred at the velocity nodes. Until a certain critical sound pressure level (SPL) was reached (155 db at 222 Hz and a Reynolds No. = 20,000), no effect on the local heat transfer coefficient could be observed; after this, an increase in the SPL resulted in an increase in the local Nusselt number. The maximum overall increase in the average Nusselt number was 20 percent.

There was a gradual transition region as the Reynolds number was increased - until at 40,000 and greater, the maximum heat transfer coefficient occurred at the velocity nodes. In this regime the pressure waves were found to suppress the heat transfer coefficient; and an increase in the SPL reduced the average Nusselt number. An analysis by Purdy et al. for laminar flow predicted the formation of vortices - which was later confirmed by experiment. Evidently, a change in the vortex pattern at the larger Reynolds numbers explains the existence of the two regimes of heat transfer.

The critical sound pressure levels, below which there was no observed effect on the local Nusselt number, were investigated by Eastwood et al. The existence of a critical SPL indicated that the secondary flows did not dominate the flow field until the pressure disturbance reached a critical level.

Bayley et al. studied the effect of pressure oscillations on the heat transfer from an electrically heated flat plate. Pressure oscillations of 10-100 Hz were produced in a duct by rotating a butterfly valve at the outlet of a six-stage blower. As was observed for internal flow in a tube, no increase in the average heat transfer coefficient was observed until a certain critical pressure amplitude was reached. Bayley et al. believed that the critical pressure amplitude corresponded to the point at which flow

reversal occurred on the plate. The maximum increase in the heat transfer rate was 50 percent.

Feiler and Yeager produced pressure oscillations at 34-680 Hz in a duct by means of a siren located upstream. The heat transfer from a flat plate placed in the duct parallel to the air stream was studied. It was found that the resulting velocity fluctuations produced an effect on heat transfer from the plate similar to that caused by an increase in the free stream turbulence intensity. High-speed schlieren photographs of the thermal boundary layer indicated that the outer edge of the layer was irregular in shape. Flow reversals in the boundary layer were observed, and fragments of the layer were dissipated in the main stream. This mechanism accounted for the observed increase in heat transfer.

Each of the above authors presented correlations for their data, but the usefulness of the correlations is questionable due to the limited range of data upon which each was based. However, it has been demonstrated that secondary flows play an important role in determining the heat transfer rate. Several authors have found that the pressure oscillations must be of sufficient strength to develop secondary flows. Feiler and Yeager found that the imposed pressure oscillations had an effect on heat transfer similar to that caused by an increased amount of free stream turbulence. Because of this similarity, their results were

correlated using the turbulence intensity as a parameter.

1-2 FORCED CONVECTION - LARGE PRESSURE AMPLITUDES

During the past ten years, Harrje, Saunders, Marec, Bogdanoff, and others at Princeton University have studied the effect of large amplitude (50 psi peak-to-peak) steep-fronted pressure waves on the heat transfer in tubes. Pressure waves were generated in a resonant tube by a siren located at the downstream end of the tube. The tube was of sufficient length so that the pressure waves had steepened by the time they reached the test section, which was a heated nichrome ribbon mounted in the wall of the tube. Heat flux increases of up to 200 percent have been obtained in this apparatus. The increase in heat flux was found to be a function of: (1) the amplitude of the local velocity oscillations, (2) the frequency of the oscillations, (3) the time-averaged gas pressure, and (4) the Mach number. The investigations were performed in fully developed turbulent flow at frequencies from 50-500 Hz. Maximum heat transfer rates occurred at the velocity antinodes. By use of an axially traversing heater section, it was also found that the degree of flow reversal was important (Marec and Harrje).

Recently, Bogdanoff performed an investigation into the importance of viscous dissipation, acoustic streaming, and the turbulence structure on heat transfer in an

isothermal tube. It was shown that the most important mechanism by which the pressure oscillations increase the heat transfer is through the generation of "abnormal" turbulence in the boundary layer. Viscous dissipation and acoustic streaming were found not to be important in most cases.

Investigations at both small and large pressure amplitudes have shown that turbulence plays an important role in heat transfer in oscillating flows. Thus, as progress is made toward an understanding of the mechanism of turbulence, so will progress be made in this area of heat transfer.

1-3 SHOCK TUBES AND RAREFACTION WAVE TUBES

Because of the geometrical similarities in the heat transfer situation at the end of shock tubes and rarefaction wave tubes to that of the present situation, a short discussion of these areas of research is included. The primary difference is that, in the above cases, the flow is not periodic; whereas in the present case it is. The investigations at the end of shock tubes (Clarke, Busing, Frieman, Peng, Lauver) are intended to determine the gas thermal conductivities and surface accommodation coefficients at elevated gas pressures and gas temperatures. The reflection of the shock wave from the end of the tube provides a stagnant gas from which heat is transferred to the end wall. From the instantaneous surface temperature measurement, the

thermal conductivity of the gas and surface accommodation coefficients can be calculated by a one-dimensional analysis.

The analysis of the end-wall heat transfer in a rarefaction wave tube (Levy, Chao) is more directly applicable to the present investigation than the shock tube work. The expansion process is similar to that which occurs during one cycle in this author's apparatus. Many of the basic assumptions concerning the thin thermal boundary layer are the same for both cases. However, their analyses differ in that the boundary condition at the outer edge of the thermal layer is non-periodic. As would be expected, the end-wall heat flux decreases rather sharply as the expansion of the gas progresses. The heat flux rates obtained were more than an order of magnitude below those obtained in the present analysis, although the form was similar.

CHAPTER TWO

EXPERIMENTAL APPARATUS

This chapter is a description of the experimental apparatus used in this investigation. First, the mechanical components of the apparatus are described in detail, followed by a description of the instrumentation used. At the end of the chapter, the operating procedure used during each test run is briefly discussed.

A schematic diagram of the experimental apparatus is presented in Fig. 2-1.[1] Pressure oscillations in the resonant tube are obtained by periodically interrupting the upstream air flow by rotating the siren disk at a frequency which corresponds to the resonant frequency of the tube. The air is supplied from a bank of air cylinders pressurized to 2500 psia. After each test run the air supply is replenished by use of a high pressure air compressor. A pneumatic control valve maintains the air pressure at the siren inlet constant during a test run. After the air passes through the resonant tube, the pressure of the air is reduced to nearly atmospheric before the flow rate is measured by a sharp edged orifice located in the discharge line. The resonant tube section of the schematic diagram is shown expanded in Fig. 2-2.

---

[1]Figures are located at the end of each chapter.

Siren Assembly

The siren assembly, as shown in Fig. 2-3, consists of three basic components: (1) the siren disk, which periodically interrupts the air supply to the tube and thus generates the pressure waves in the tube, (2) the inlet nozzle, which limits the mass flow rate in the tube, and (3) the labyrinth type seals, which minimize air leakage from the apparatus. It was found convenient to construct the siren assembly from an existing steam turbine. The turbine wheel was replaced by the siren disk, and a boss was welded onto each side of the upper turbine housing to provide mounting surfaces for the other components.

The siren disk is twenty-three inches in diameter, with eighteen equally spaced holes located as shown in Fig. 2-4. In order to minimize vibration of the disk, as caused by the alternate closing and opening of the air supply to the resonant tube, the disk was made 0.88 in. thick. For a stationary disk of this size, the natural frequency is calculated to be greater than 2500 Hz (Timoshenko and Young). However, when the disk is rotating, centrifugal force will resist any deflection of the disk and thereby increase its natural frequency. An additional benefit obtained by having a thick disk is that it makes an effective flywheel. Therefore, although there is alternate loading of the siren disk as it interrupts the air flow,

its speed remains constant. The siren disk shaft is connected to a 30 Hp, AC motor by a series of V-belts. The motor speed is constant at 3600 rpm, and the siren shaft can be driven at four speeds so that pressure waves at frequencies of 479, 694, 881, and 1080 Hz can be generated. The critical speed for the shaft with the siren disk mounted is 7000 rpm (Baumeister). This assembly was dynamically balanced before installation.

The siren disk was fabricated from "T-1" Type A constructional alloy steel with a 100,000 psi yield strength. With this high strength steel, the burst speed of the disk is 11,000 rpm (Roark). Therefore, there is a safety factor of three at the maximum operating speed of 3600 rpm.

The converging inlet nozzle has an elliptical entrance profile followed by a straight bore section. Several nozzles with different throat diameters were used. The desired operating conditions for the run determined which nozzle was installed in the apparatus.

Two labyrinth type seals are used to minimize air leakage from the apparatus. The labyrinth seals consist of a series of concentric lips which are adjusted to within a few thousandths of an inch from the surface of the siren disk. When contact with the steel siren disk does occur, such as during wear-in of the seals, the thin lip of the seal quickly wears away, since it is made of Asarcon 773 bearing bronze (SAE designation 660).

The siren assembly components are designed for an inlet air pressure of 600 psia. The housing which encloses the siren disk is not pressurized. The air leakage into the housing is discharged to the atmosphere through a sharp edged orifice by which the rate of air leakage is monitored.

Tube Assembly

The tube assembly consists of three components: (1) the telescoping assembly, (2) several spacers, and (3) the main tube. These components enable the tube length to be adjusted to a resonant length prior to each test run. All of the components are made of brass. The apparatus as viewed from the tube end is shown in Fig. 2-5. The test plate has been removed and is shown on the right.

The telescoping assembly as shown in Fig. 2-6 provides for a continuous length adjustment of 1.25 in. The feather section is tapered so that there is a gradual transition in the inside diameter of the tube assembly from 0.907 to 0.957 in., where the tip thickness is 0.005 in. Since the inside diameter of the remainder of the tube is 0.968 in., there is an abrupt change in the tube I.D. of 0.011 in. This small abrupt change in the tube I.D. was not detrimental to the shape of the pressure wave generated. Figure 2-7 is a view of the upper siren housing with the air inlet on the left and the telescoping assembly on the right.

One inch incremental changes in tube length are obtained by inserting several lengths of spacers in series. The spacers are piloted so that the step in the I.D. of the tube is maintained at less than 0.001 in. at each interface. With the use of different main tube lengths, the total tube length can be adjusted from 20 to 117 in.

Test Section

The air, with superimposed pressure oscillations, flows down the length of the tube and is radially discharged at the tube end through the gap between the test plate, which forms the tube end-wall, and the test plate holder (see Fig. 2-8). This configuration forms a converging-diverging nozzle with the throat located at the tube diameter and with the diverging portion being formed by the gap between the test plate and its holder. The test section consists of a one inch diameter Pyrex insert mounted in the test plate. Since vibration of the test plate caused by the impacting pressure waves could affect the heat transfer at the plate, the vibration was minimized by using a cast iron plate 1.125 in. thick.

2-2 INSTRUMENTATION

The nature of this investigation requires that cyclic surface temperature measurements and cyclic gas pressure measurements be obtained. This imposes a stringent requirement on the instrumentation since the oscillations occur at such a high frequency (479-881 Hz). The location of the instrumentation which is installed near the test section is shown in Fig. 2-9.

Surface Temperature

The cyclic surface temperature measurement was difficult since the amplitude of the temperature oscillation was quite low (0.25 - 2.0°F), in addition to being at a high frequency. Currently, there are three techniques available by which the surface temperature oscillation could have been accurately measured. All three techniques utilize evaporated thin films on the surface whose temperature is to be measured. Thin film thermocouples in which two evaporated films are overlapped have been developed by Hackemann, Bendersky, and others. These are commonly used for interior surface temperature measurements in internal combustion engines (Bennethum, Pless, Overbye).

Thin film resistance thermometers are extensively used in shock tube work where microsecond response is necessary (Bogdan, Hall, Hartunian, Miller, Vidal). Hall gives a

good historical account of the development of the thin film thermocouple and the resistance thermometer. The thin film resistance thermometer was chosen for this investigation because, when placed in a bridge circuit, its output sensitivity is greater than that of the thin film thermocouple. Because of the greater sensitivity of thin resistance films, thin film thermocouples have largely been abandoned in shock tube applications.

The third technique is a recent development - within the last year - whereby thin film thermistors have been produced in a thickness range of 500 Å - 950 Å (Victory Engineering Co.). This technique seems quite promising because of the great sensitivity of thermistors to temperature changes. However, this author is not aware of any references in which transient surface temperatures have been measured by a thin film thermistor.

In order to obtain measurable surface temperature oscillations, it was necessary to use a low thermal conductivity surface - thereby minimizing the thermal penetration depth. Since thin film resistance sensors deposited on No. 7740 Pyrex substrate were commercially available,[1] it was decided to make the test surface from No. 7740 Pyrex. The sensor used was a 0.062 in. thick disk, 0.190 in. in diameter, with a 0.020 in. wide platinum film 1000 Å thick deposited on its surface. The thin film sensor was mounted

---

[1] Astro-Space Laboratories, 2104 Memorial Parkway, Huntsville, Alabama 35801.

in a one inch diameter disk of Pyrex as shown in Fig. 2-10. This assembly was then mounted in the test plate as shown in Fig. 2-9.

The sensor was bonded to the Pyrex disk with a 0.001 in. thick layer of epoxy around its edge. This was cured, and the remaining cavity behind the sensor was filled with epoxy and cured once again. The surfaces were flush within 0.001 in., so that any disturbance to the air flow was minimized. Both the sensor substrate and the disk in which it was mounted were of the same material (No. 7740 Pyrex) - insuring that there would be no disruption in the surface temperature distribution due to dissimilarities in thermal properties. The platinum is chemically bonded to the Pyrex, insuring good thermal contact. A protective silicon monoxide overcoating, 1000 Å thick, was applied to the platinum film. With this coating, the response time of the sensor was approximately 10 microseconds. The electrical leads are attached to the rear of the sensor, and hence do not disturb the surface temperature distribution. Before attachment of these leads, a thin film connecting the platinum strip with the rear of the sensor was deposited. A photograph of the sensor as mounted in the test plate is shown in Fig. 2-11.

The platinum thin film was placed in the constant current Wheatstone bridge circuit shown in Fig. 2-12. In order to insure that the joule heating of the thin film was negligible, the current through the thin film was limited to two milliamperes. The bridge sensitivity was

approximately 0.2 mv/°F and linear in its operating range. The output signal from the bridge was amplified one thousand times before being displayed on an oscilloscope. The amplified signal was then passed through a low pass filter so that the average surface temperature rise could be recorded on a Brush chart recorder. The resistance versus temperature calibration of the thin platinum film is linear, as shown in Fig. 2-13.

Pressure

The oscillating gas pressure was measured with a Kistler (601L) piezoelectric pressure transducer with a rise time of three microseconds and a resonant frequency of 130,000 Hz. The transducer was used in conjunction with a Kistler (No. 566) charge amplifier. The signal output from this system was linear over the operating range. This transducer was chosen because of its small size (0.25 in. diameter by 0.6 in. long), and it was mounted in the side of the tube 0.5 in. from the test surface (see Fig. 2-9). The recess resulting from the mounting of the pressure transducer was filled with RTV adhesive/sealant to minimize disturbance to the air flow. A Bourdon pressure gauge with a pulsation snubber in the connecting instrument line was used to monitor the average gas pressure in the tube.

Gas Temperature

The thermocouple probe used to measure the average gas temperature was placed in the center of the tube, 0.5 in. from the test surface, as shown in Fig. 2-9. The thermocouple was supported by a 0.008 in. diameter stainless steel sheath approximately 0.5 in. long. The small size was chosen to minimize any disturbance to the air flow. The thermocouple wires were 0.001 in. diameter, with a 0.003 in. diameter exposed bead. As with the pressure transducer installation, the recesses in the tube wall due to the mounting of the probe were filled to minimize the disturbance to the air flow.

Mass Flow Rate

After the air was discharged from the end of the tube and its pressure reduced to nearly atmospheric, it passed through a sharp-edged orifice. From the measurement of the pressure drop across the orifice, the average mass flow rate was calculated.

Frequency

The frequency of the pressure oscillation was measured by means of an electromagnetic pickup, which produced eighteen pulses per revolution of the siren shaft. Since there are also eighteen holes in the siren disk, the frequency at which the pressure waves were produced could be measured by an electronic counter. The electronic counter was cycled every ten seconds during a test run, and this showed that the frequency remained constant within ± 0.5 Hz during each test run.

2-3 OPERATING PROCEDURE

The experimental apparatus is located in a test cell adjacent to the control room. This arrangement is desirable since during a test run the operating personnel are separated from the high speed rotating siren disk, the high pressure air, and the intense noise level. Figure 2-14 is an overall view of the control room, to which all the test data were transmitted and recorded during a test run.

A test run was begun by first starting the siren disk. Once the siren disk had reached a constant speed, the inlet air pressure was gradually increased until the desired average tube pressure was reached. The inlet pressure (and consequently the average tube pressure) was then maintained constant by the upstream control

valve, and the data were recorded. The data were taken as quickly as possible because of the limited air supply, a typical run taking from sixty to ninety seconds. The air flow was then stopped, and the power to the siren disk shut off.

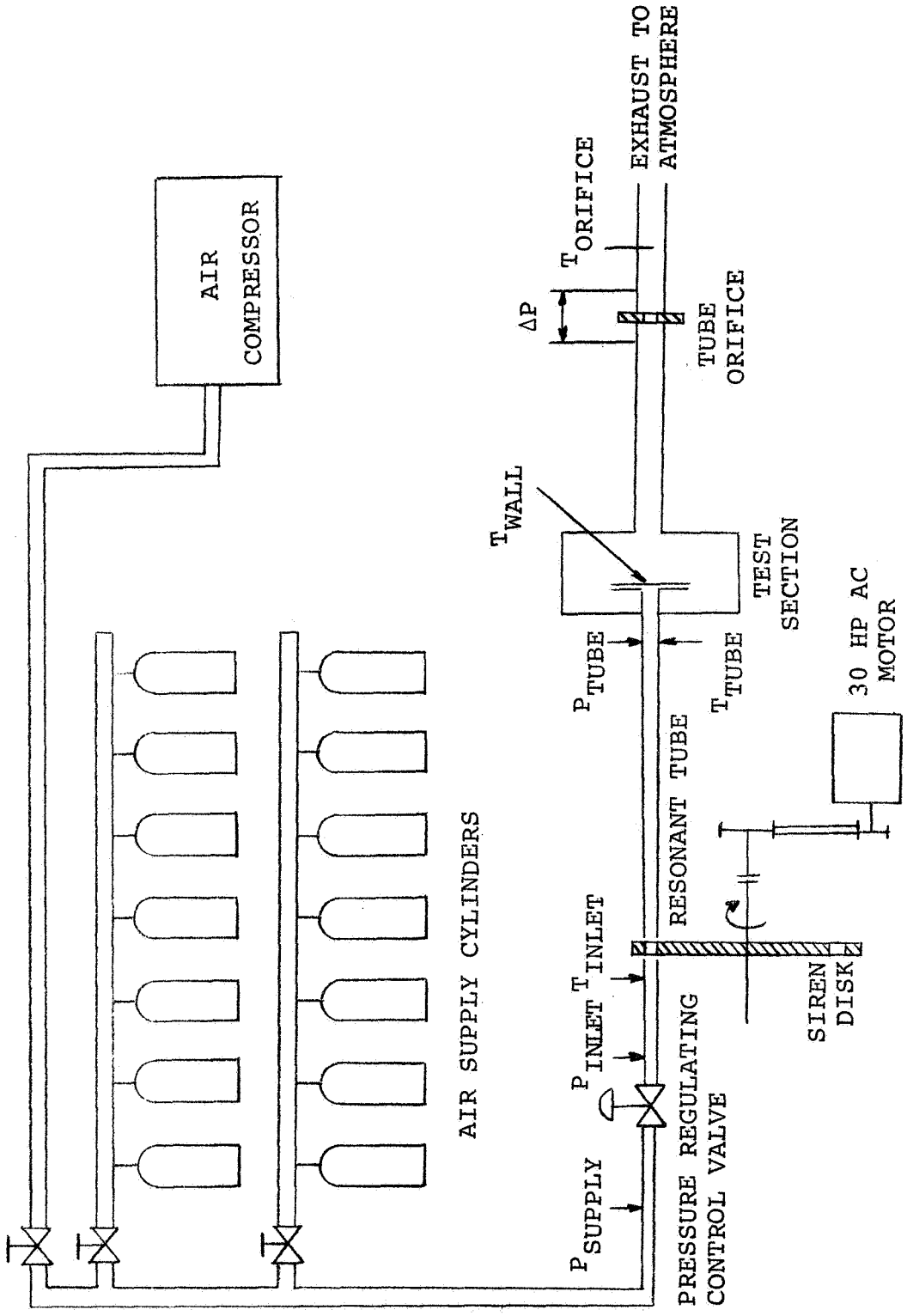

Fig. 2-1 Schematic Diagram of Experimental Apparatus

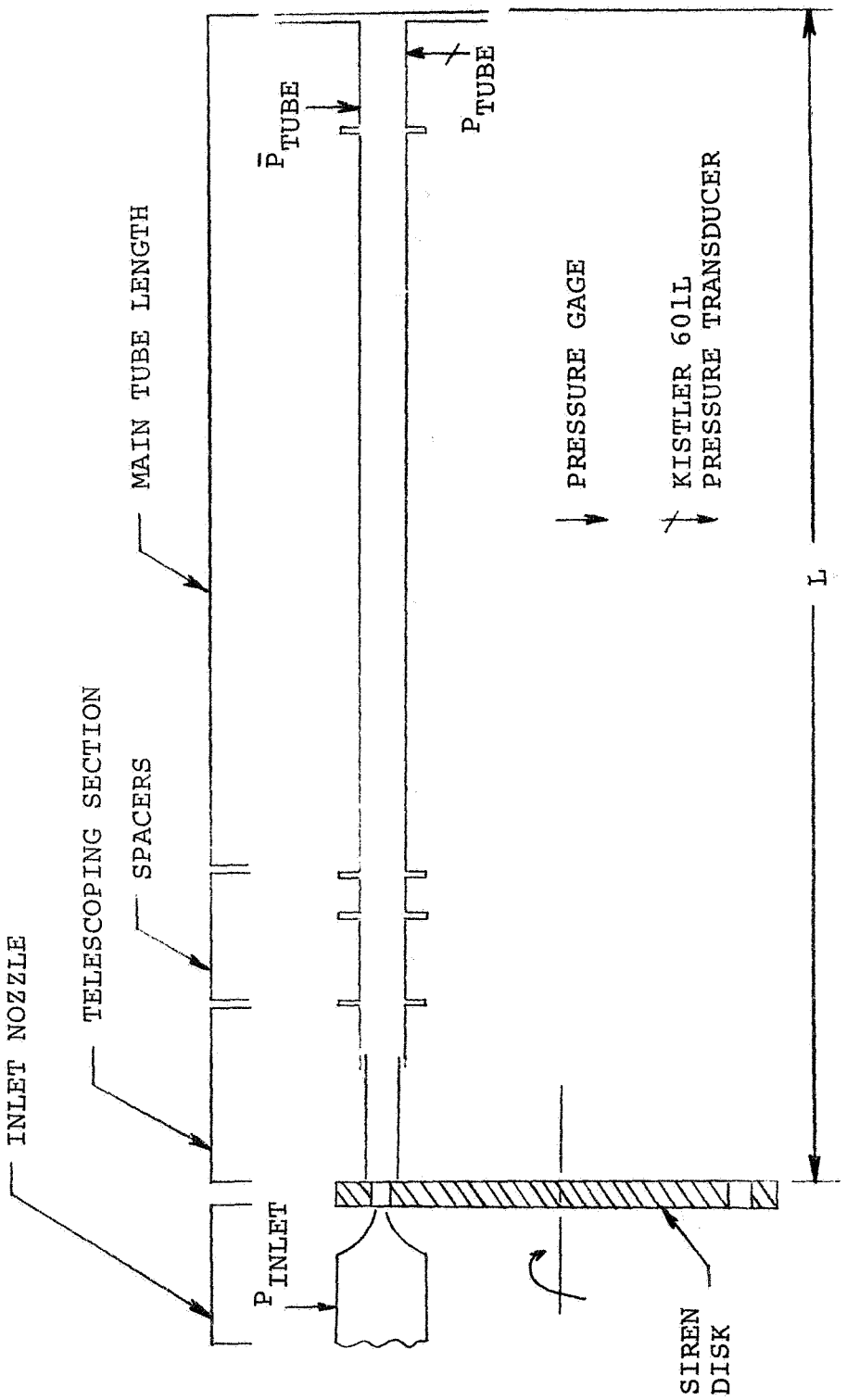

Fig. 2-2 Schematic Diagram of Resonant Tube

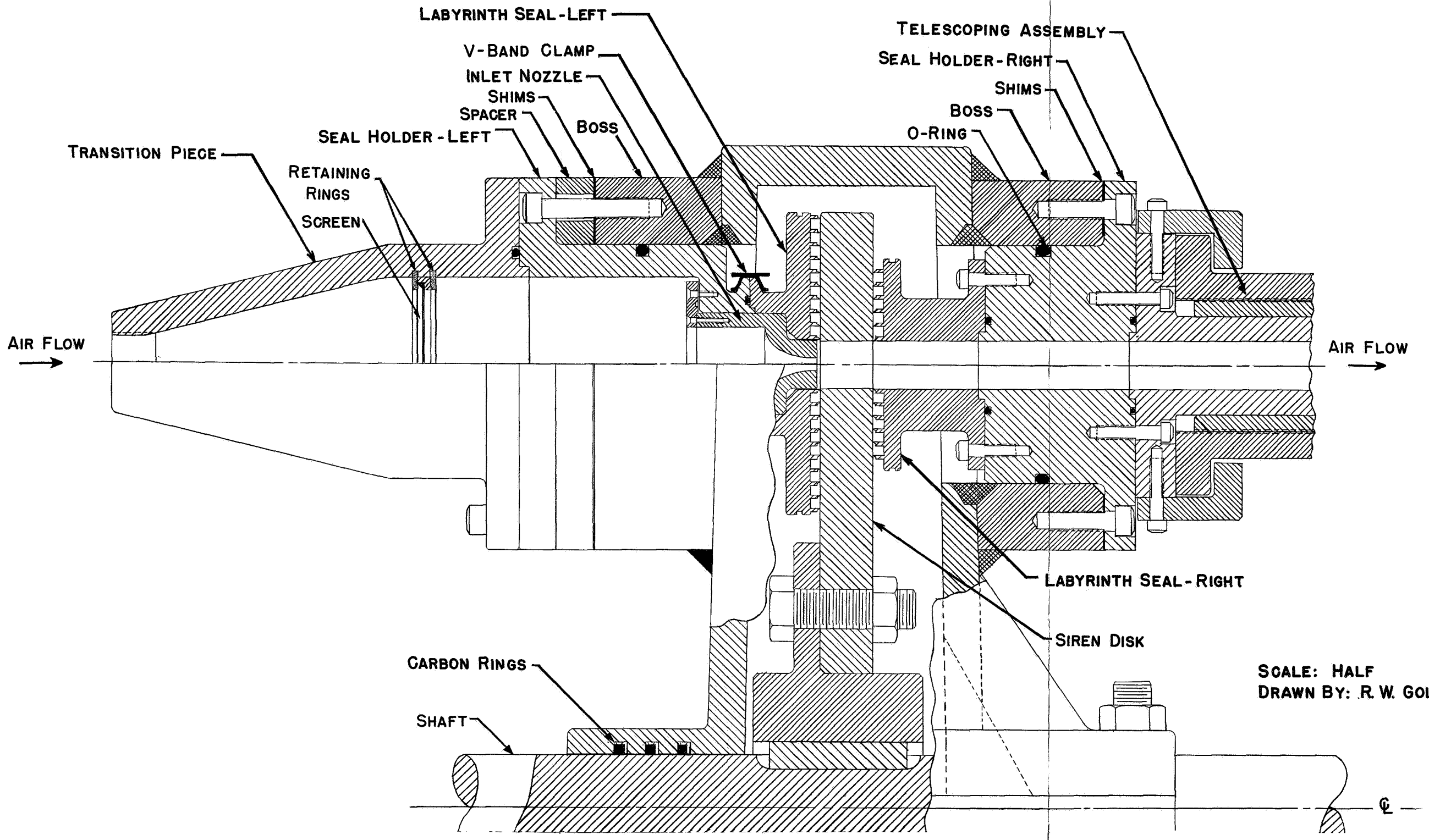

FIG. 2-3 SIREN ASSEMBLY

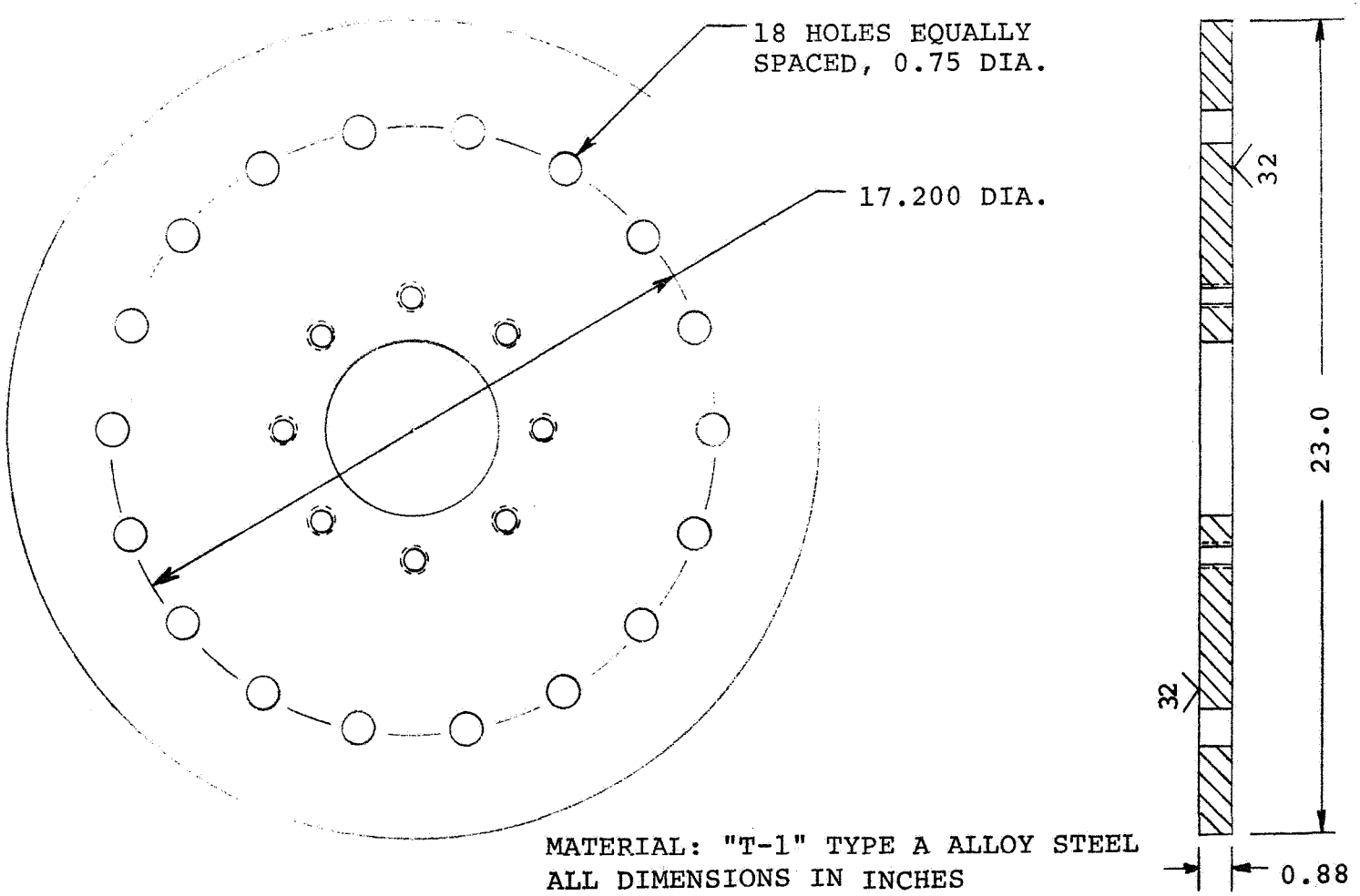

Fig. 2-4 Siren Disk

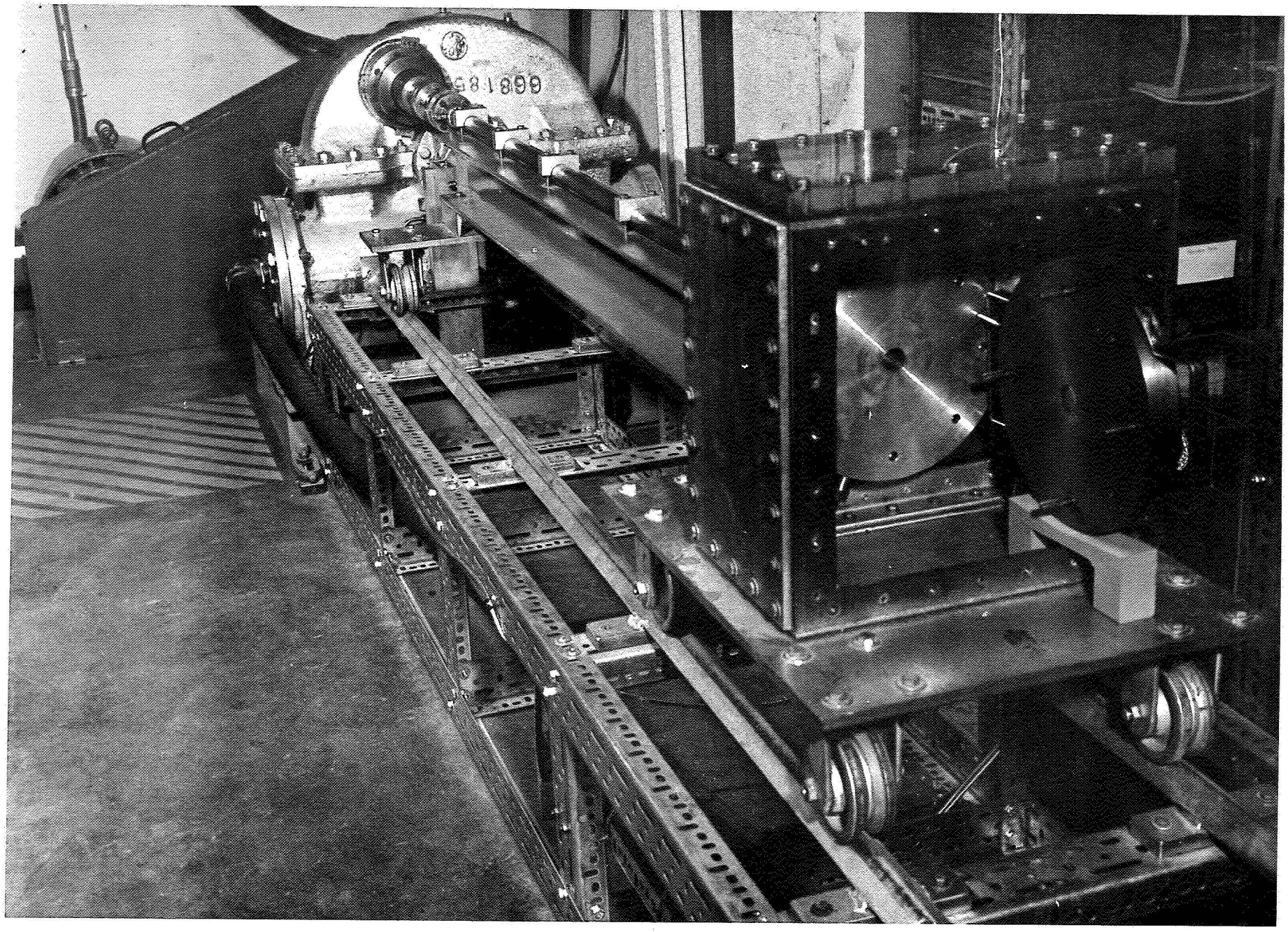

Fig. 2-5 Overall View of Siren

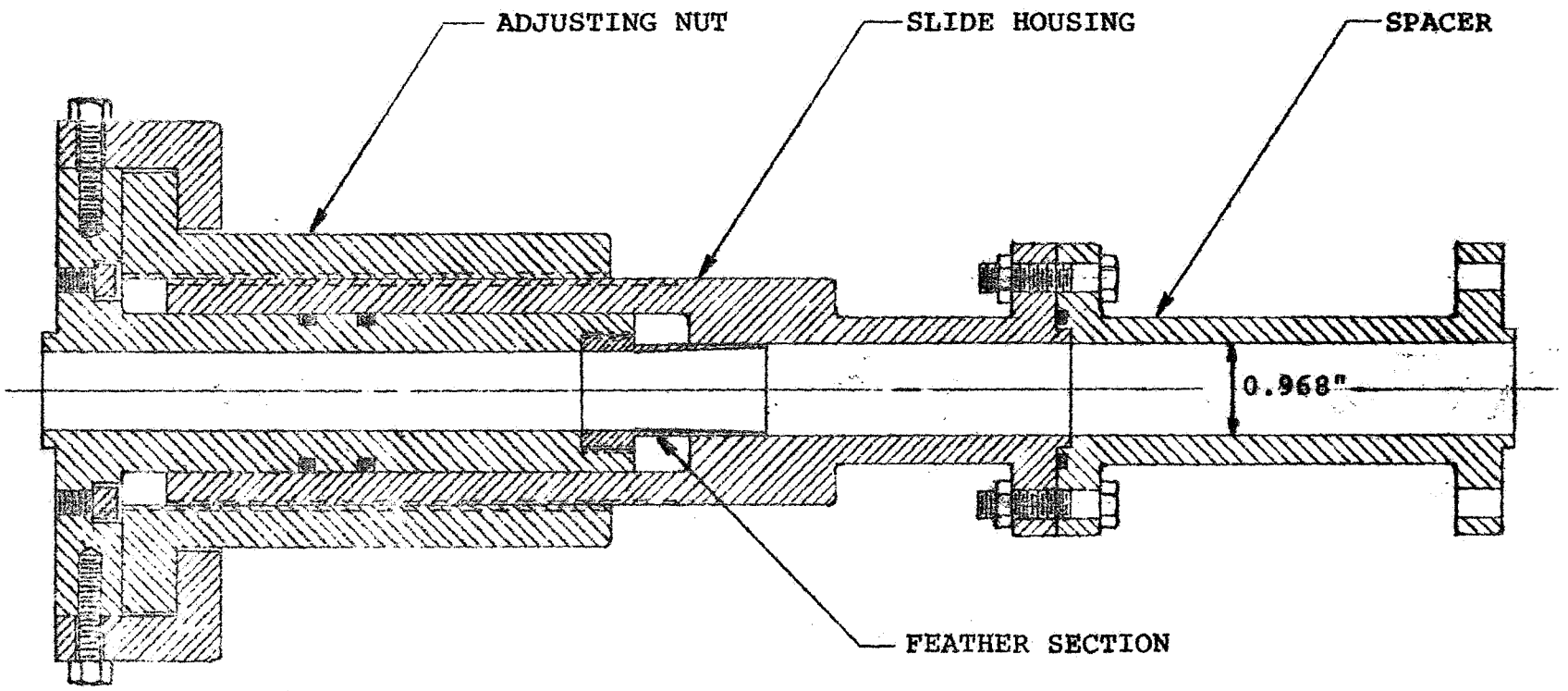

SCALE: HALF

Fig. 2-6 Telescoping Assembly

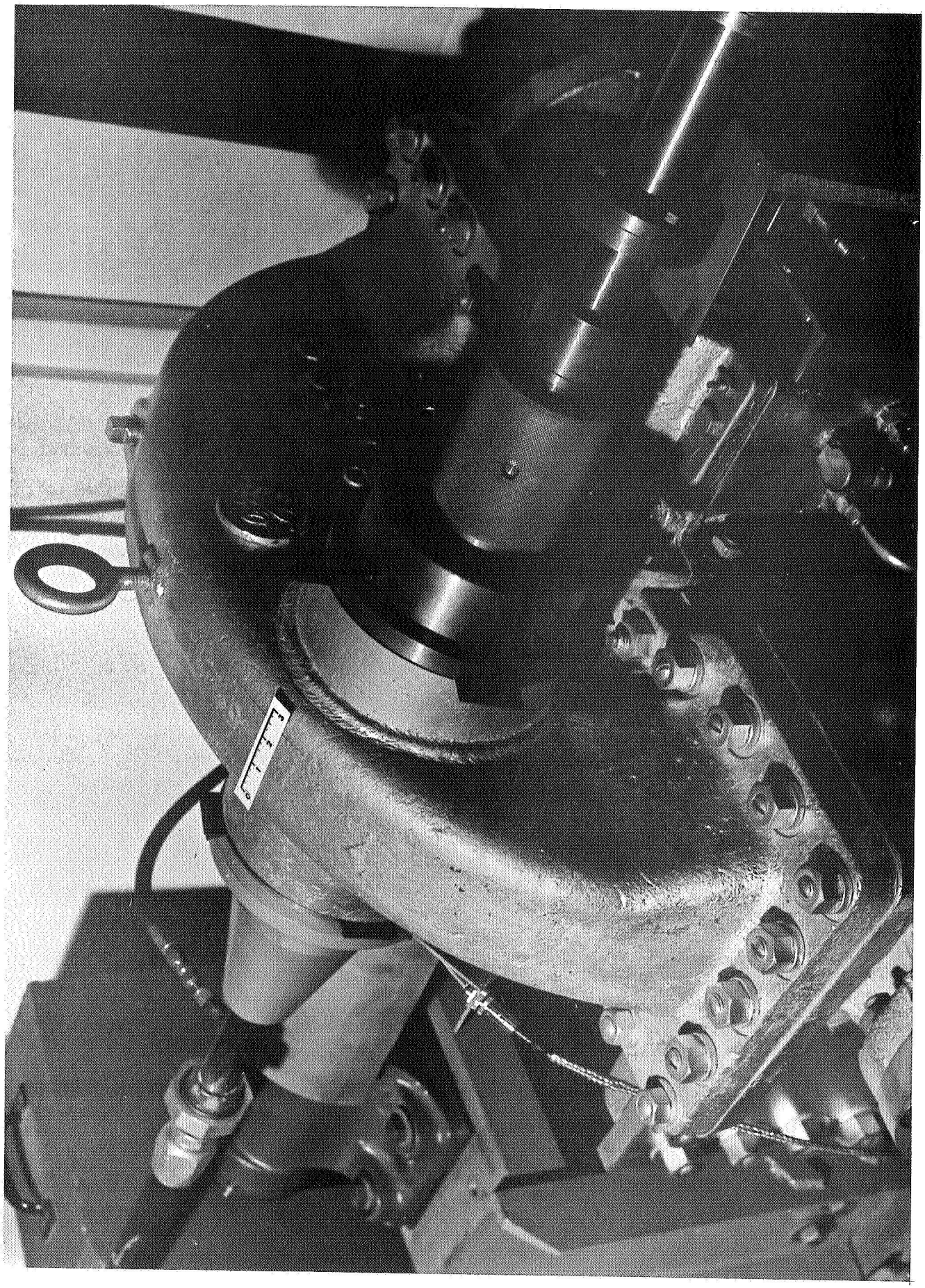

Fig. 2-7 Siren Housing

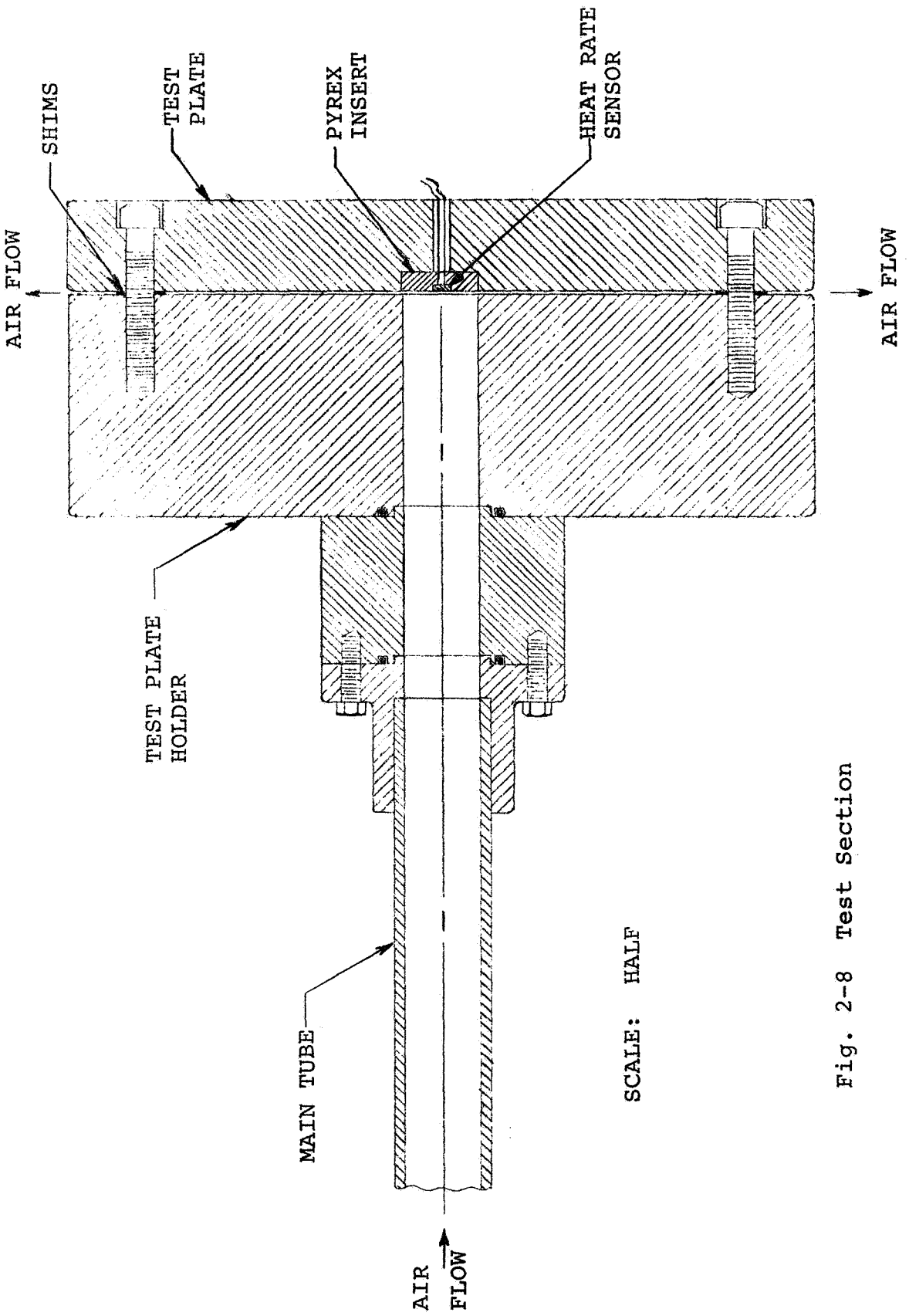

Fig. 2-8 Test Section

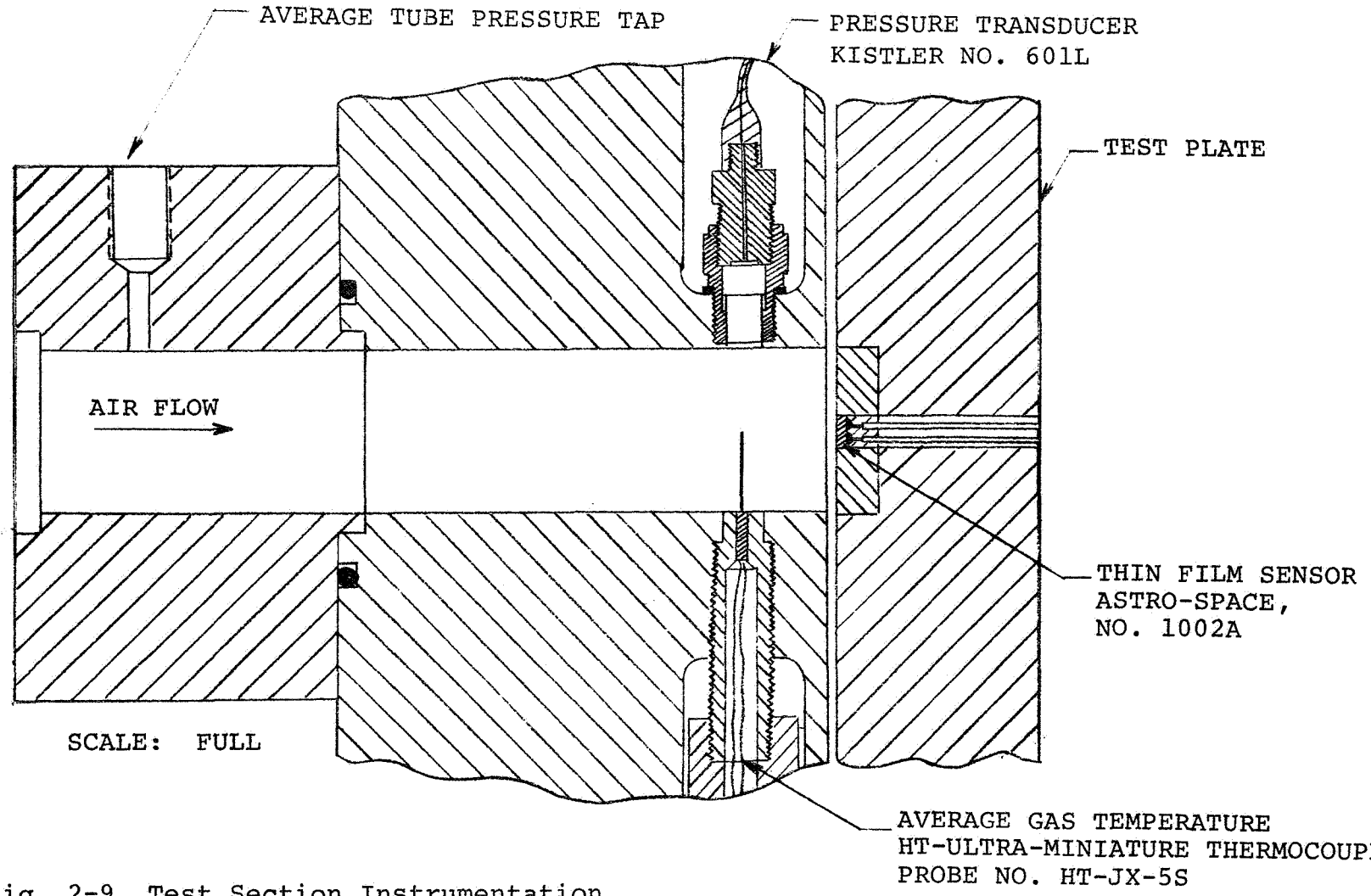

Fig. 2-9 Test Section Instrumentation

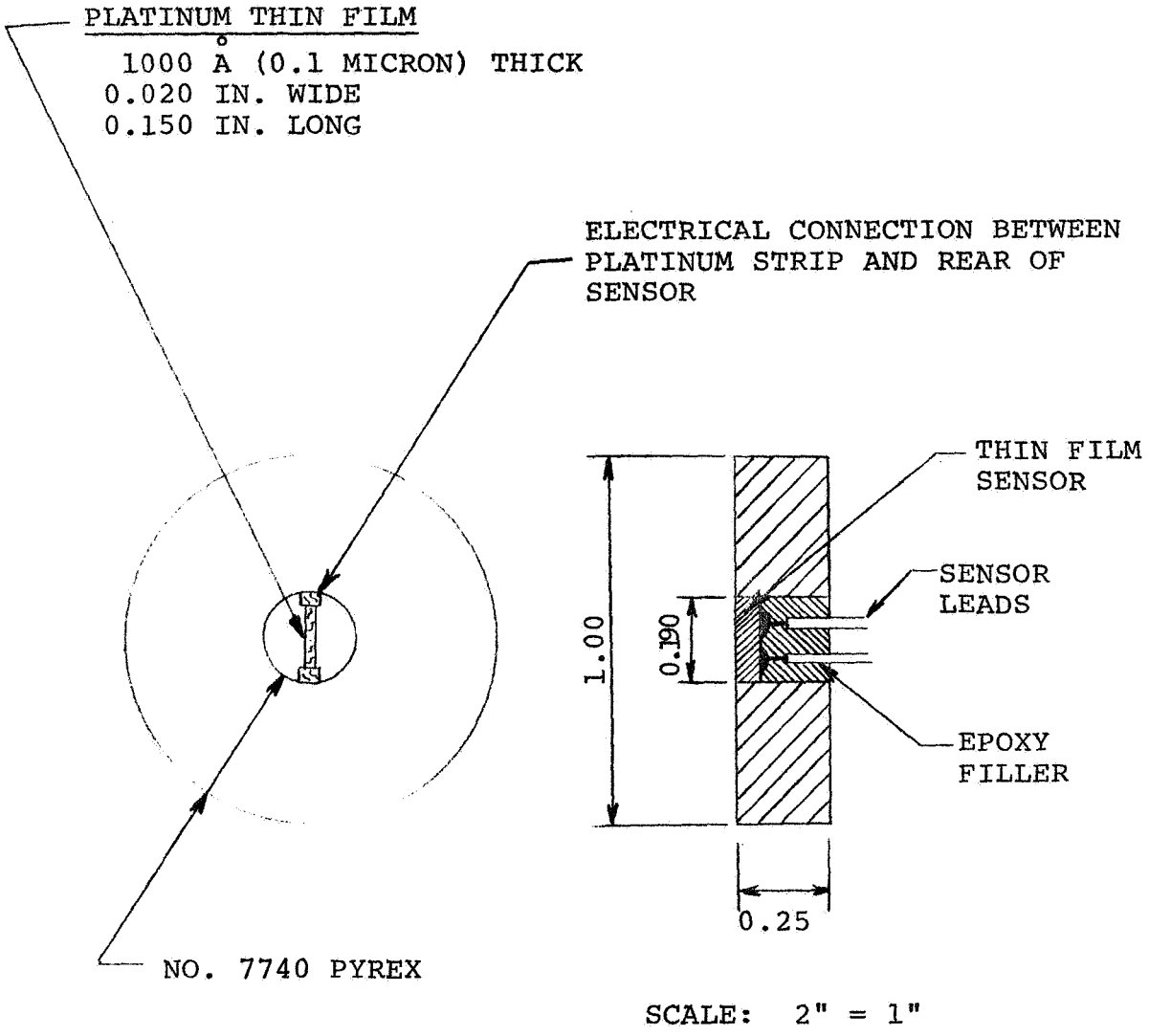

Fig. 2-10 Pyrex Insert with Thin Film Sensor Mounted

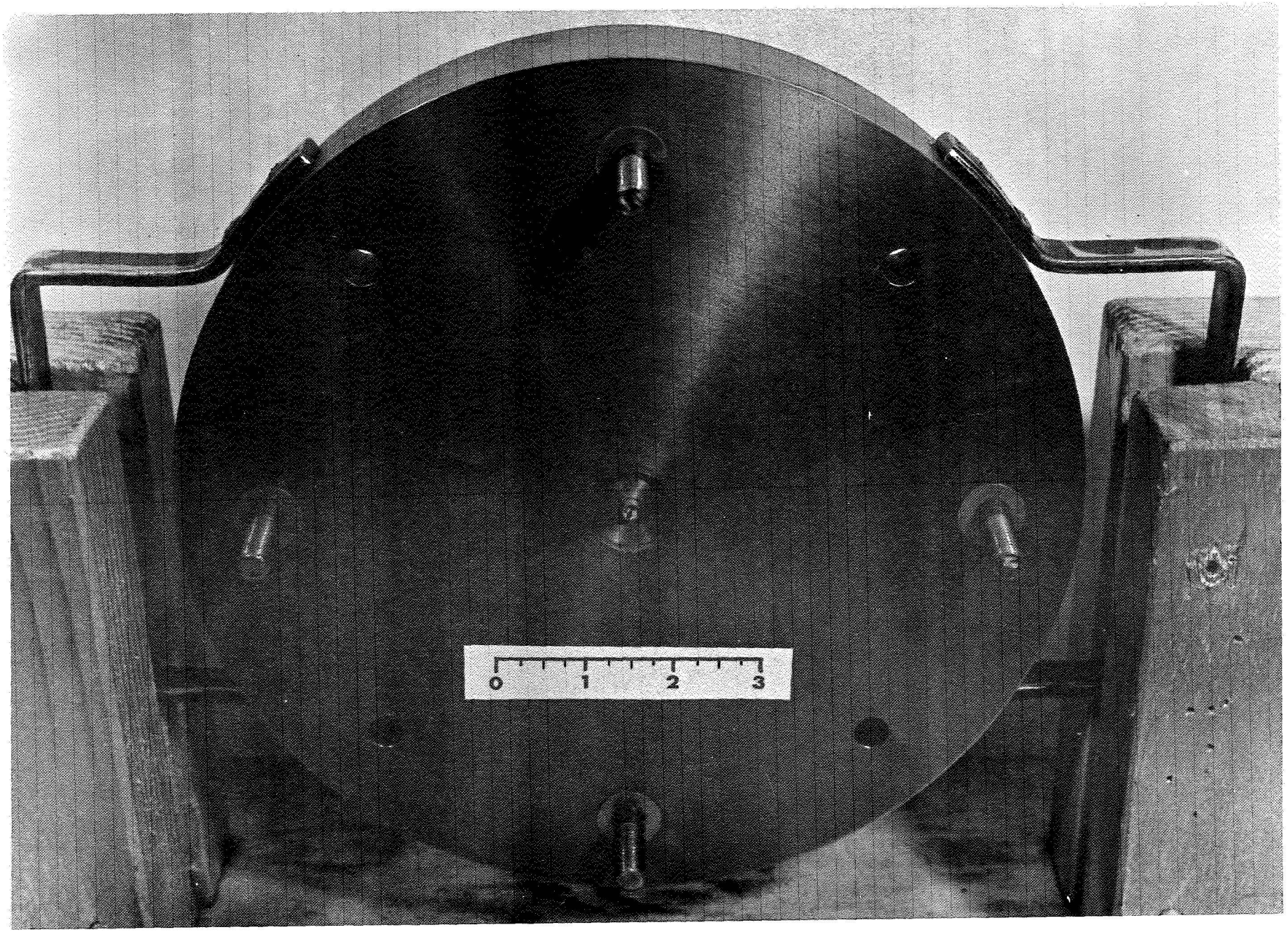

Fig. 2-11 Test Plate with Pyrex Insert Mounted

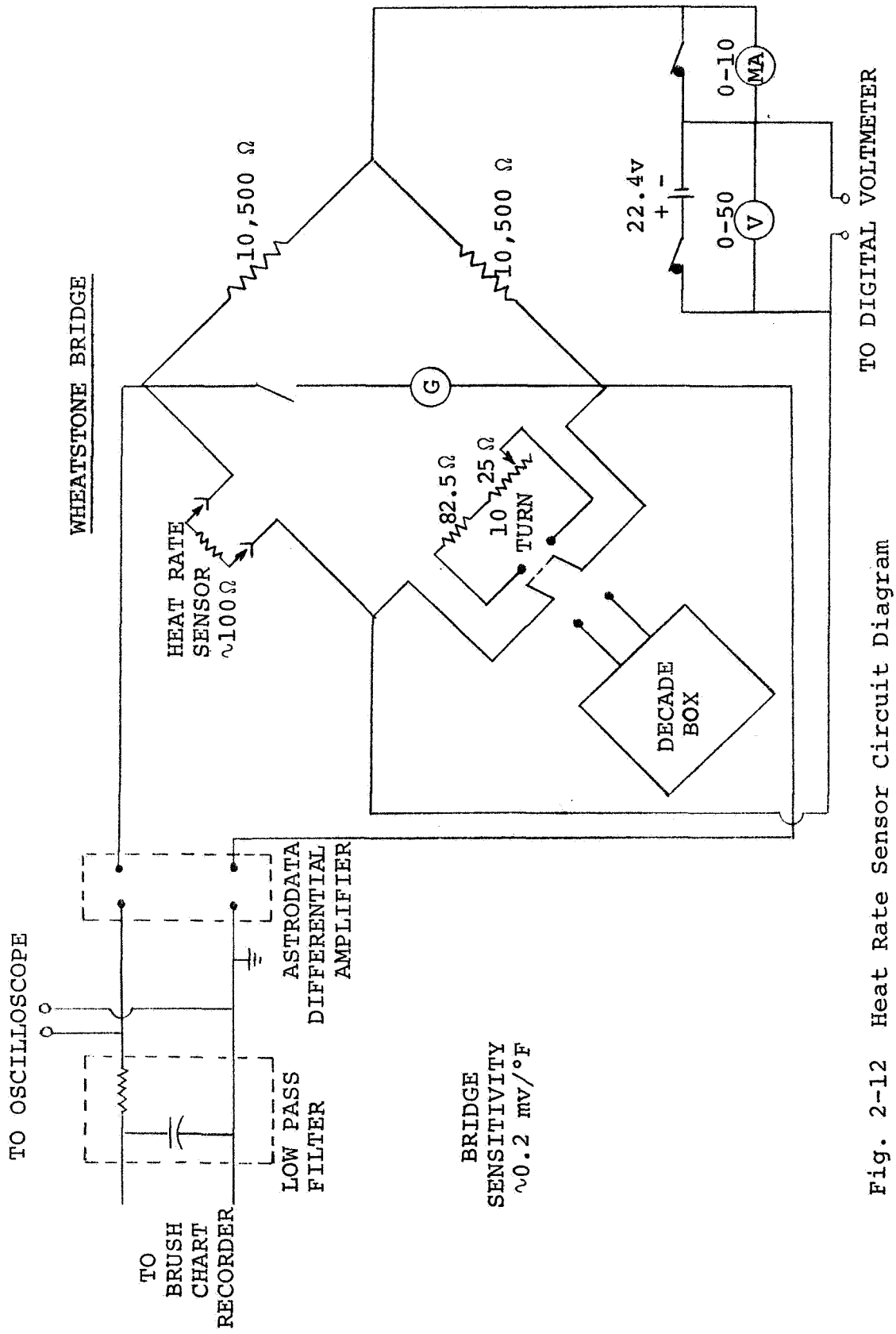

Fig. 2-12 Heat Rate Sensor Circuit Diagram

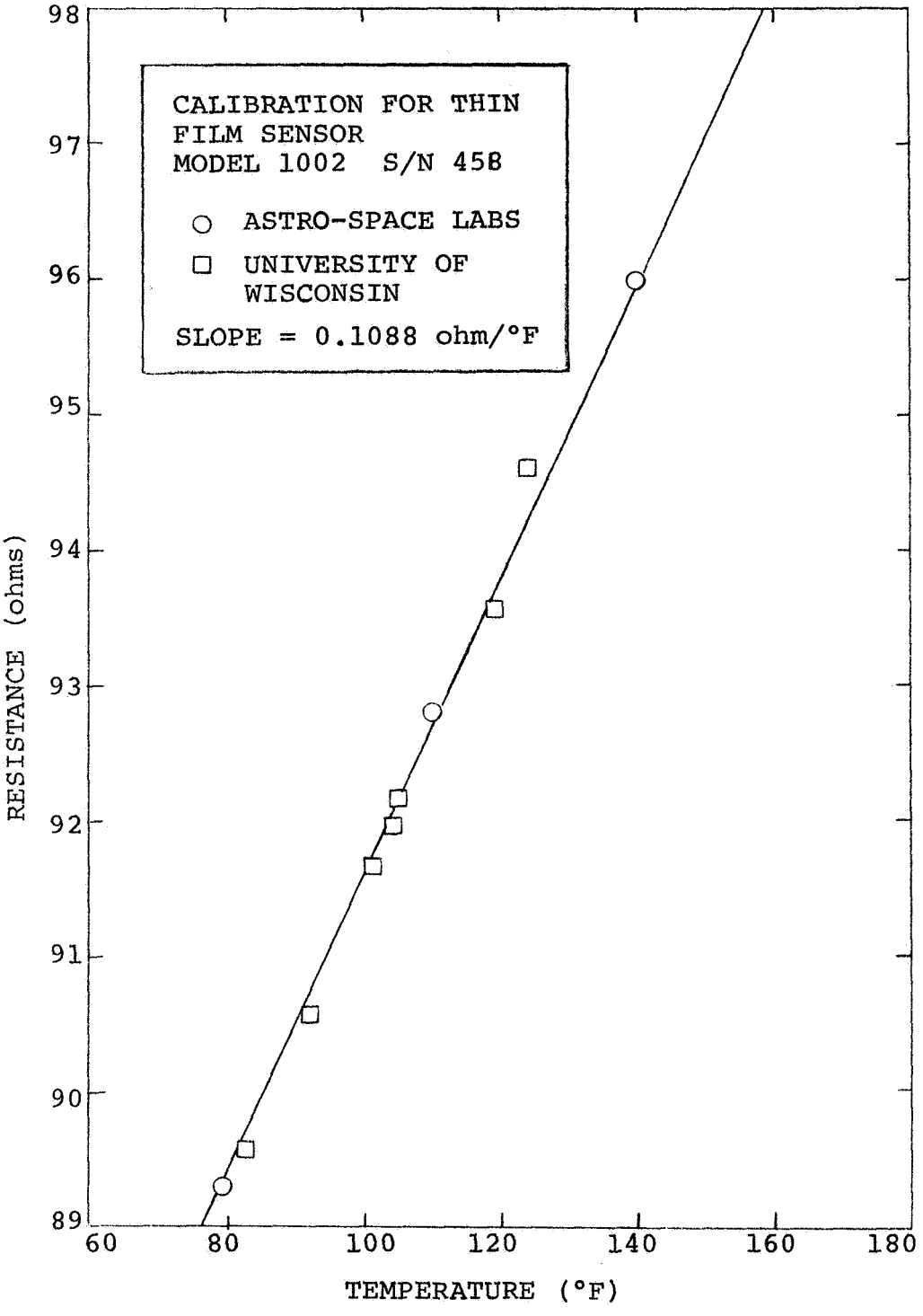

Fig. 2-13 Calibration Curve for Platinum Thin Film Resistance Sensor

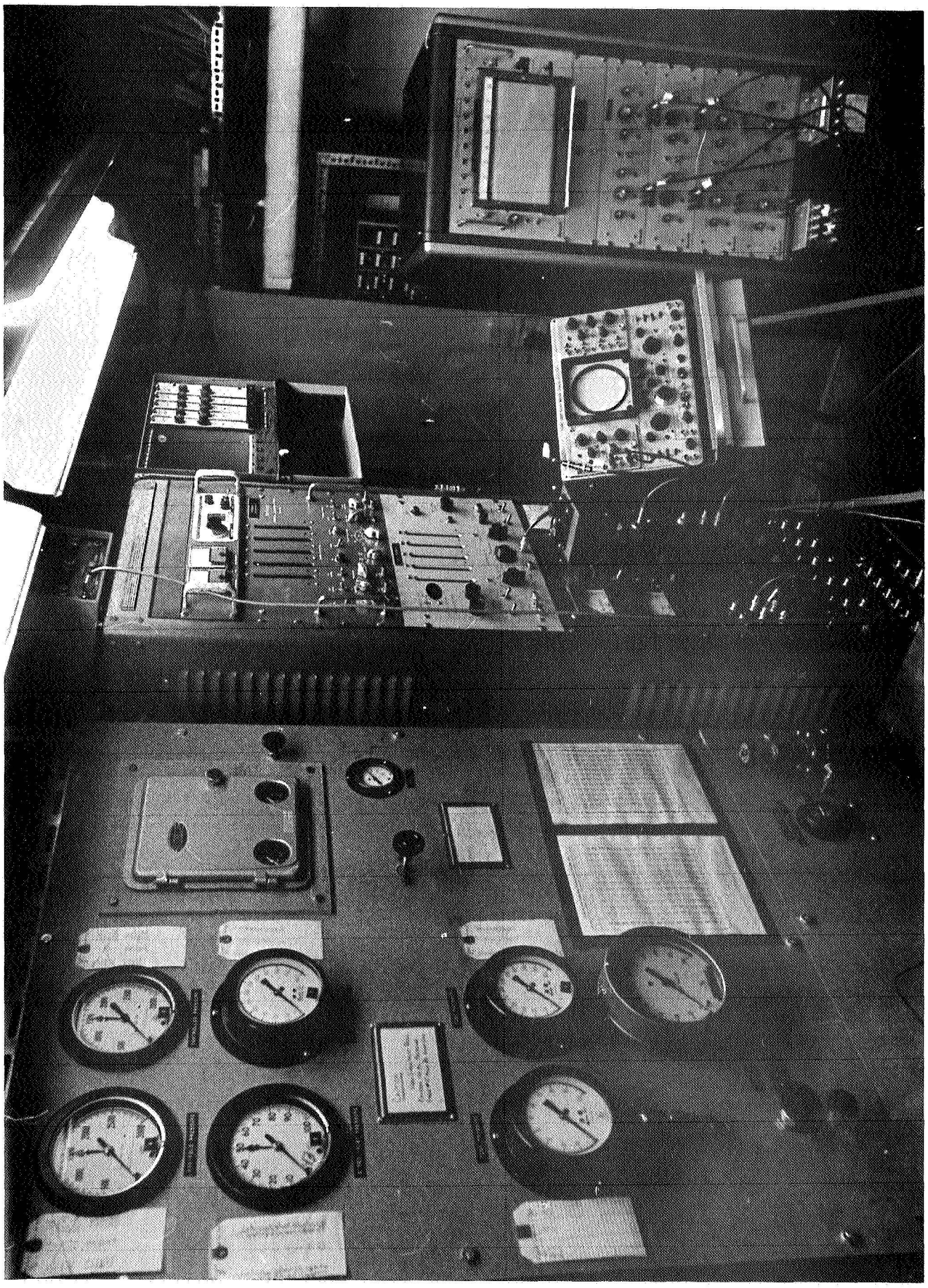

Fig. 2-14 Control Room

CHAPTER THREE

PERFORMANCE OF THE APPARATUS

A discussion of the performance of the apparatus as affected by the operating conditions is included in this chapter. The shape of the pressure wave and its amplitude are of greatest interest and are discussed in detail. The increase in the stagnation temperature of the gas in the resonant tube, which results from the action of the pressure waves, is discussed; and the chapter concludes with the results of a brief flow visualization study which was undertaken at the test section.

3-1 EFFECT OF OPERATING VARIABLES ON THE WAVE PRESSURE RATIO

The amplitude of the pressure waves generated by the apparatus is a function of: (1) the ratio of average[1] tube pressure to the average inlet pressure, P_{ti}, (2) the inlet nozzle throat area, (3) the frequency, and (4) the resonant tube length. The temporal pressure wave shape that is obtained at the test plate is similar to that shown in Fig. 3-1 and differs slightly from that measured by the pressure transducer mounted 0.5 in. upstream from the plate.

---

[1] In the text which follows, all averages refer to time-averages.

The difference in the shapes is discussed further in Sec. 3-2. The pressure ratio across the wave is defined in Fig. 3-1 as $P_r = P_m/P_0$ where P_m is the maximum pressure of the oscillation and P_0 is the minimum pressure of the oscillation.

The operation of the apparatus is much like that of a shock tube in that the siren disk suddenly exposes the high inlet pressure to the lower tube pressure. This action generates a shock of moderate strength. However, unlike the shock tube, the siren disk next shuts off the air supply for a short period of time before reopening. During this time the upstream air cavity, shown outlined in Fig. 3-2, undergoes a filling process. The air pressure in the cavity, P_s, increases until either equilibrium with the inlet reservoir pressure is attained or the siren reopens - whichever occurs first. In the case of higher frequencies, the siren reopens before pressure equilibrium with the inlet reservoir is attained and the air pressure in the cavity, P_s, is decreased. This decrease in P_s results in a lowering of the pressure ratio across the wave generated. Likewise, a decrease in the inlet nozzle throat area retards the filling of the air cavity and also results in a lowering of P_s. As before, this lowers the pressure ratio across the wave. These trends are evident in the performance data that are presented in Figs. 3-3 and 3-4. The frequency of the pressure waves in the tube

is determined by the number of times per second the inlet pressure is repeatedly exposed to the tube pressure.

As would be expected, the pressure ratio across the wave increases as the ratio of the tube pressure to the inlet pressure, P_{ti}, decreases (see Figs. 3-3 and 3-4). For these figures the tube length is fixed (100 in. at 479 Hz and 98.5 in. at 694 Hz). Comparison of Figs. 3-3 and 3-4 shows that, for a given P_{ti}, the smaller nozzle results in a lower value of P_r. It can also be seen from these figures that an increase in the frequency decreases P_r - as was previously explained.

Lower P_{ti} values than shown can be obtained by increasing the average inlet pressure or decreasing the average tube pressure. Both of these adjustments require that the test plate gap be enlarged. However, it was found that when test plate gaps greater than 0.075 in. were used, P_r began to decrease with decreasing P_{ti}. This decrease is caused by a significant portion of the pressure wave being reflected from the test plate and transmitted to the outside atmosphere through this gap. This was evidenced by an increase in the noise level in the test cell when large plate gaps were used. All the data presented here were obtained at test plate gaps of less than 0.050 in.

In order to obtain a shock-fronted pressure wave at the test plate similar to that shown in Fig. 3-1, it is necessary that the tube length be adjusted to a resonant length. The tube resonates as if it were closed at both

ends, and the resonant lengths can be calculated from the simple organ pipe formula:

$$L_r = \frac{an}{2f} \qquad n = 1,2, \ldots, N \qquad (3\text{-}1)$$

where

L_r = resonant length

a = speed of sound

f = frequency.

For a tube closed at both ends the resonant lengths are integral multiples of the half wave length. At the short tube lengths ($1\frac{1}{2}$ wave lengths or less) the length of the tube had to be adjusted to within 0.1 in. or resonance would not occur. These lengths could not be accurately calculated, although they were always found to be within 0.5 in. of those calculated by Eq. 3-1. With the tube in a non-resonant condition, the pressure wave measured at the plate would exhibit a step in the shock-front as shown in Fig. 3-5. At the longer tube lengths, the adjustment of the tube length was not as critical (within 0.5 in.) and could always be calculated by Eq. 3-1.

As the resonant tube length is decreased, with all of the other operating variables fixed, the amplitude of the pressure wave is increased. The amplitude and shape of the pressure wave at any point in the tube is a sum of the pressure waves which were generated at the siren and all of their subsequent reflections from the tube ends. Because of the reduced frictional attenuation at the

shorter tube lengths, the amplitude of the pressure wave is increased. There were no means provided for maintaining the shape of the pressure wave constant from one run to another. Consequently, the pressure wave shape varied slightly from one run to another. Although the majority of runs had pressure shapes similar to that shown in Fig. 3-6a, the runs made at lengths of two wavelengths or less exhibited the shape shown in Fig. 3-6b. The ratio of P_r divided by the P_r obtained at a tube length of 100 in. is plotted in Figs. 3-7, 3-8, and 3-9. These figures show that a 50 percent increase in P_r can be obtained by reducing the tube length. As before, the effects of the inlet nozzle area, frequency, and the ratio of the average tube pressure to the average inlet pressure are apparent.

3-2 PRESSURE WAVE SHAPE AT DIFFERENT TUBE LOCATIONS

A series of tests was undertaken to determine the shape of the pressure wave with time at various locations along the length of the tube when the total tube length is fixed at a resonant length. The results of these tests are shown in Figs. 3-10 and 3-11. In Fig. 3-10, as one moves away from the test plate at $x = 0$ (a pressure antinode), a step appears in the pressure rise of the wave as is pointed out in the figure. The width of the step, as defined in Fig. 3-10, grows with distance, until at the pressure node, the amplitude of the pressure wave has been

reduced by approximately one-half. At this point, the step width has increased until the pressure wave now exhibits a frequency double that at the antinode. As one continues down the tube, the step width gradually recedes and finally disappears at the next antinode at x = 14.2 in. A similar situation occurs at greater distances from the test plate, as shown in Fig. 3-11, although the pressure shapes are not identical with those in Fig. 3-10. At this distance, the pressure tap locations were such that an entire one-half wave length could not be traversed. However, from Fig. 3-10 it would seem that locations could be found where there would be no step in the pressure wave shape.

3-3 ALTERNATE OPERATING GEOMETRY

In an alternate method of operation, the end of the tube can be completely closed, and the air flow through the apparatus maintained by bleeding air from the tube at a point far upstream. The pressure wave shape is the same as that obtained in the open end configuration. However, the resonant length was found to be approximately one percent larger than that calculated from Eq. 3-1. This alternate geometry was not used in this investigation since the apparatus was originally designed for the open end mode of operation.

3-4 AVERAGE GAS TEMPERATURE IN THE TUBE

The action of the pressure waves in the tube increases the stagnation temperature of the tube gas above that of the gas in the upstream reservoir. The behavior of the average gas and plate surface temperatures is shown in Fig. 3-12. Initially, the tube is at atmospheric conditions. With the siren disk rotating, the air flow is started at time zero. As the tube pressure rises, the average gas temperature increases sharply as a result of the filling process. Then the average gas temperature rapidly decreases for two reasons: (1) heat is transferred to the tube walls and (2) the air that was initially compressed during the filling process is exhausted to the atmosphere through the plate gap. In the absence of the pressure waves the average gas temperature would decrease to the original inlet temperature of 70°F. The reason that the average gas temperature only decreases to a value T_q is not well understood. A possible explanation is that there is a net energy addition per cycle to the gas, via work, as a result of the action of the pressure wave. For equilibrium, this energy addition per cycle must be balanced by a net heat transfer per cycle to the tube walls; therefore, the average gas temperature must be greater than the temperature of the tube walls. The average gas temperature gradually increases from T_q with time as the plate and tube wall temperatures rise. As shown in Fig. 3-12, the average

surface temperature of the test plate rapidly increases until at τ = 40 sec. a steady gradual increase is established. The stagnation temperature of the tube gas was found to increase 15-20°F from the upstream reservoir temperature at a frequency of 479 Hz. The stagnation temperature increased approximately 30°F at the higher frequency of 881 Hz as more pressure work per unit time is done on the gas.

3-5 FLOW VISUALIZATION

To learn about the fluid flow pattern near the test plate, two flow visualization methods were tried. In the first method smoke was injected into the air stream. The smoke, however, diffused into the flow so rapidly that streamlines could not be distinguished. A surface oil technique proved to be more satisfactory. With this technique a mixture of kerosene and lampblack was placed onto the surface of the test section. The air flow was maintained until all of the kerosene had been blown from the plate and only the dried lampblack pattern remained. Shutdown of the airflow did not disturb this pattern. The pattern was photographed and projected onto a screen at a magnification of 30. With this magnification a great amount of detail could be discerned. A typical flow pattern obtained is shown in Fig. 3-13. Near the center portion of the pattern no streaking was observed, indicating that

the shear stresses there were small. Definite streaking could be observed on the test plate near the tube I.D. where the air velocity increases as the air escapes to the atmosphere. Examination of the slides did not disclose any non-radial flow, leading one to believe that there were no strong secondary flows present. Comparison of the experimental data with the theoretical model in Chapter Six showed that the air near the center of the plate can be considered to have only a velocity component normal to the plate - as was indicated by this visualization study.

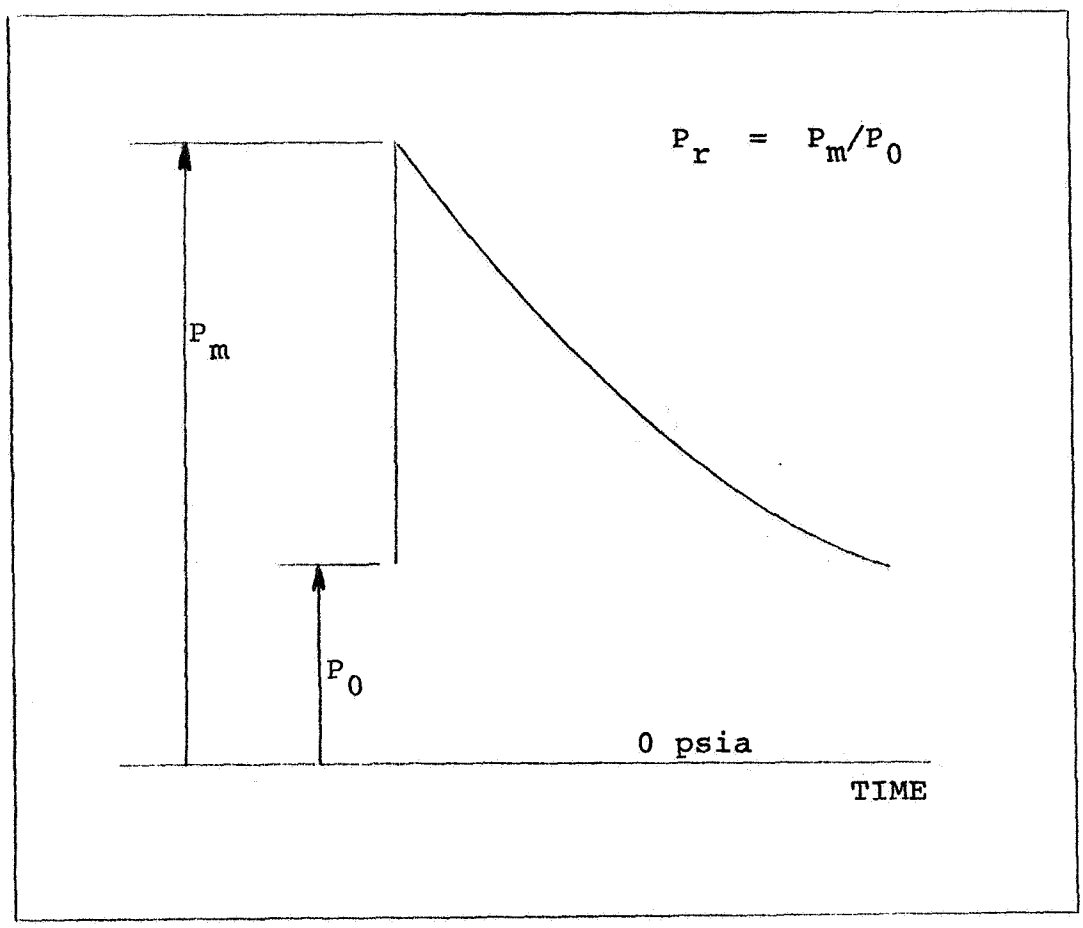

Fig. 3-1 Pressure Shape at the Test Plate

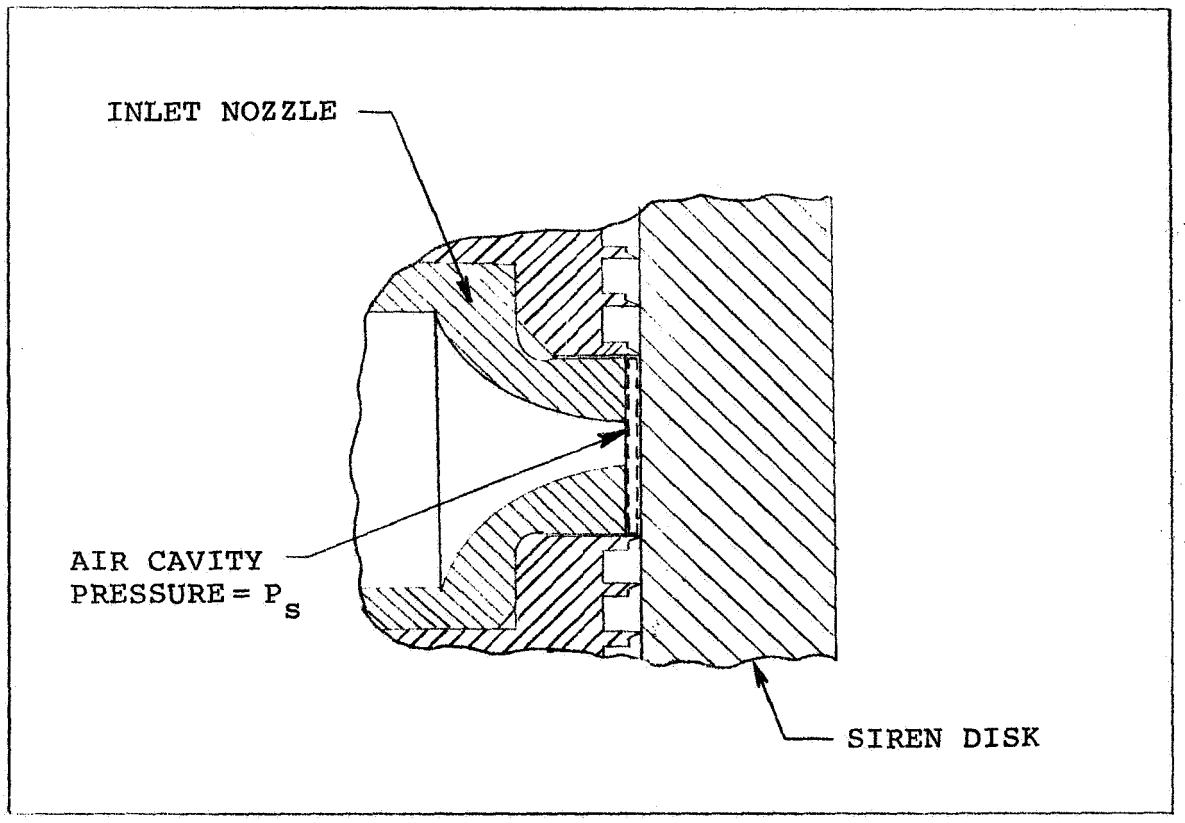

Fig. 3-2 Siren Disk in Closed Position

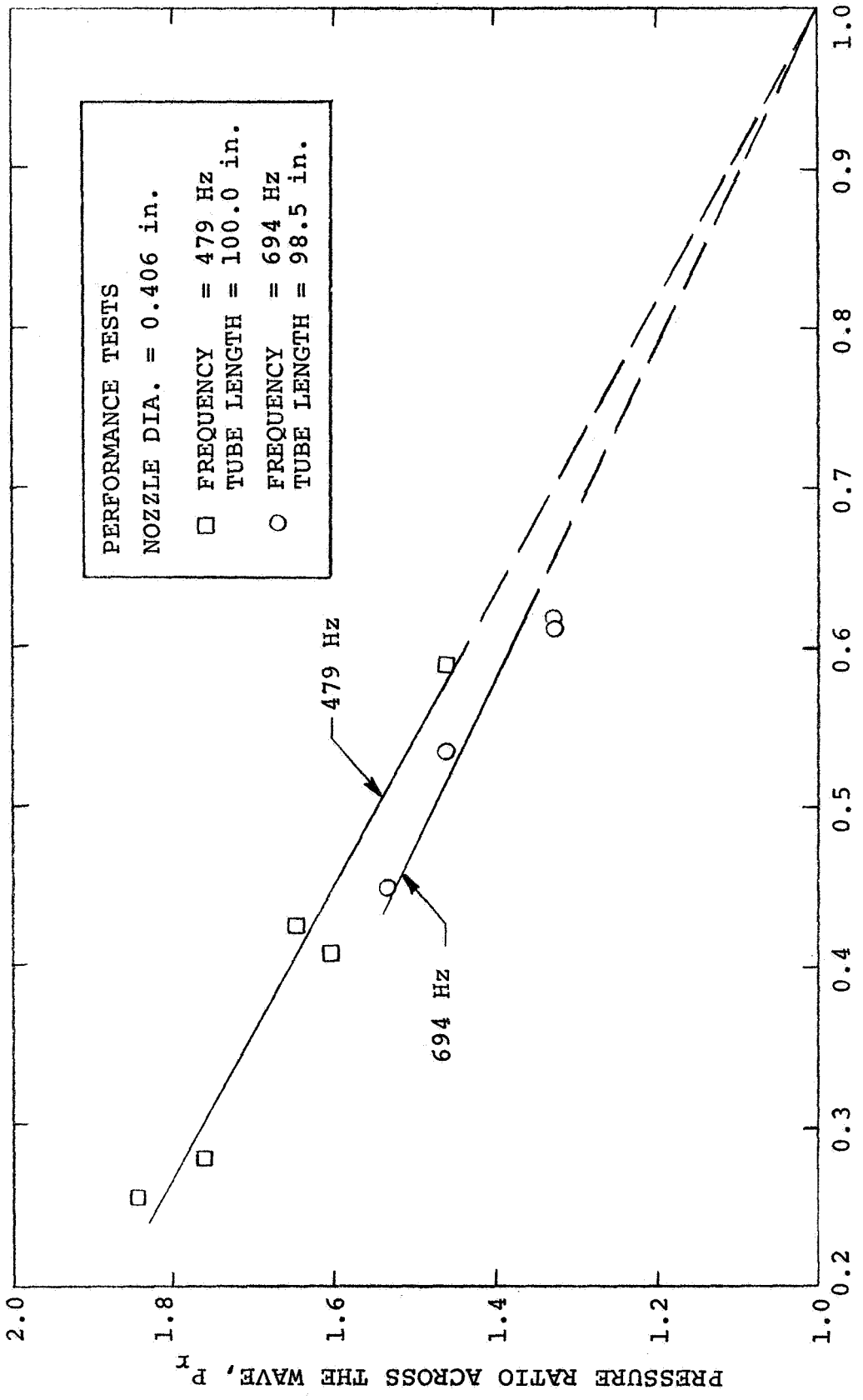

Fig. 3-3 Pressure Ratio Across the Wave Plotted Versus P_{ti} at 479 and 694 Hz with a 0.406 in. Diameter Nozzle

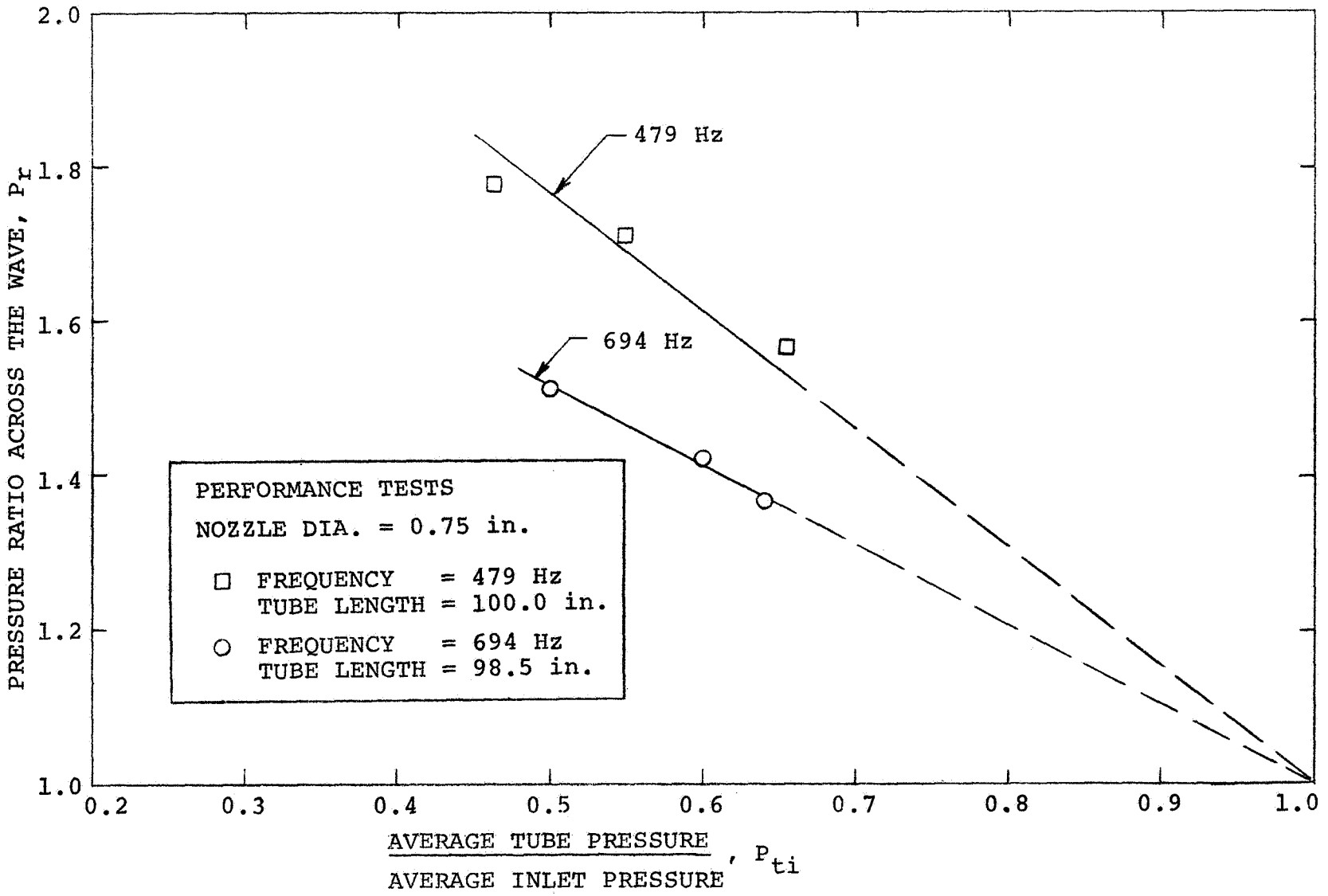

Fig. 3-4 Pressure Ratio Across the Wave Plotted Versus P_{ti} at 479 and 694 Hz with a 0.750 in. Diameter Nozzle

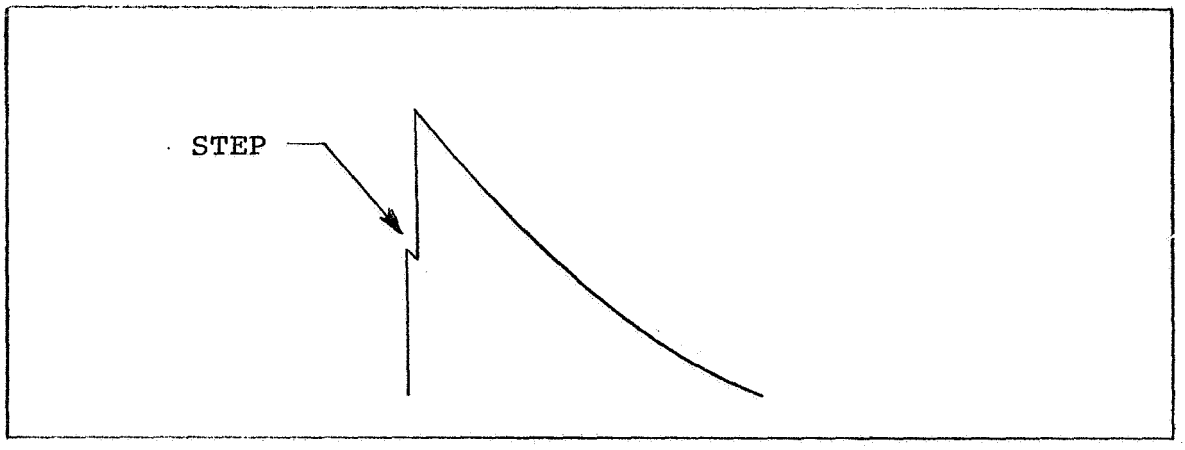

Fig. 3-5 Pressure Wave at the Test Plate - Non-resonant Condition

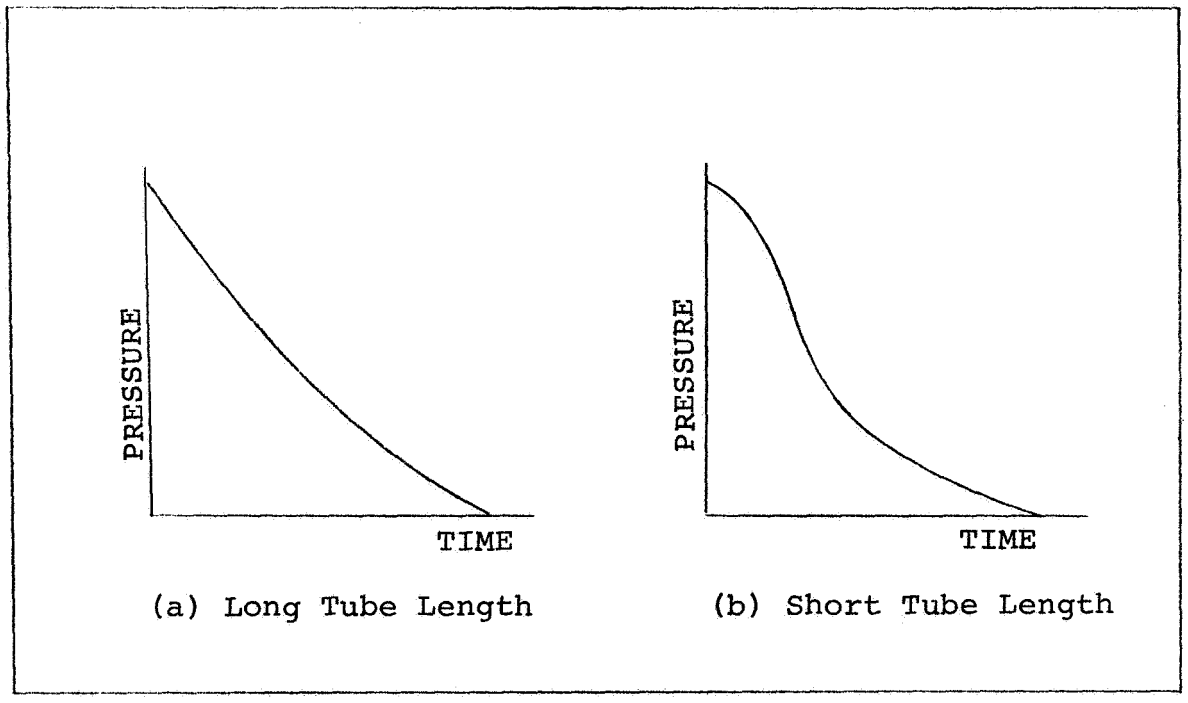

(a) Long Tube Length (b) Short Tube Length

Fig. 3-6 Pressure Wave Shape at the Plate for Long and Short Tube Lengths

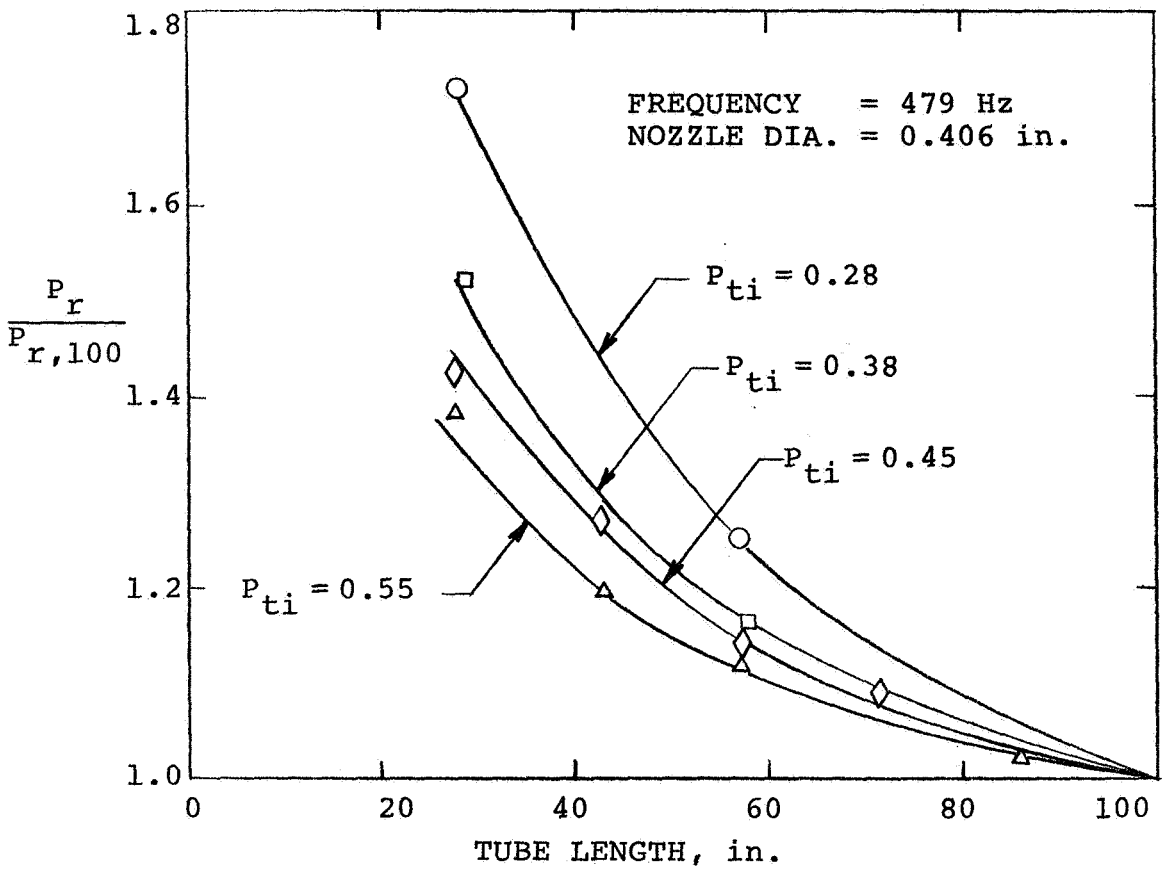

Fig. 3-7 Effect of the Resonant Tube Length on the Pressure Ratio Across the Wave for Various P_{ti} Values

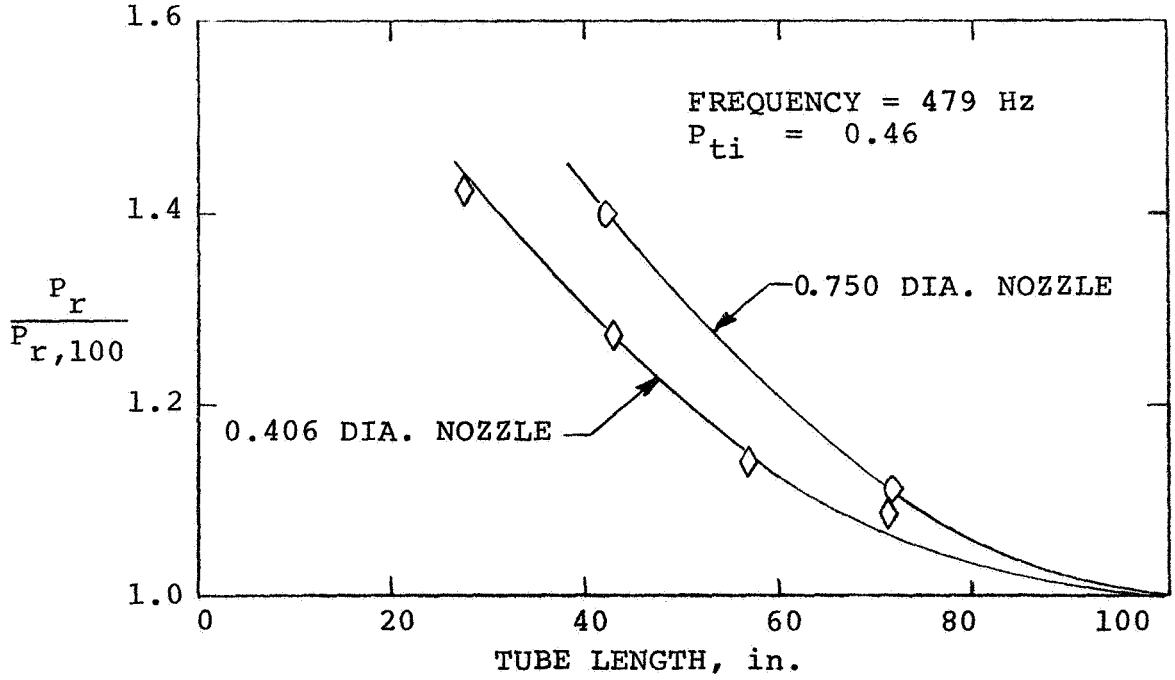

Fig. 3-8 Effect of the Resonant Tube Length on the Pressure Ratio Across the Wave for 0.406 and 0.750 in. Diameter Nozzles

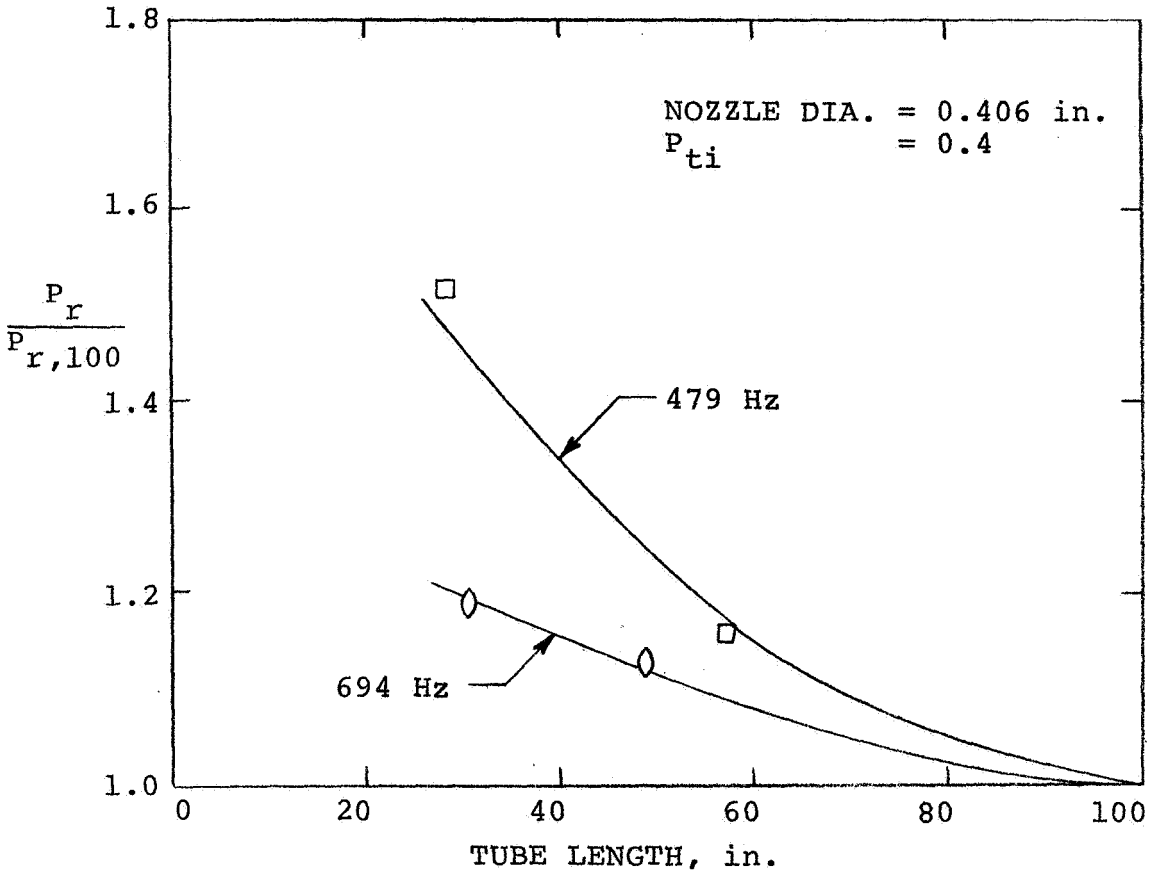

Fig. 3-9 Effect of the Resonant Tube Length on the Pressure Ratio Across the Wave for 479 and 694 Hz

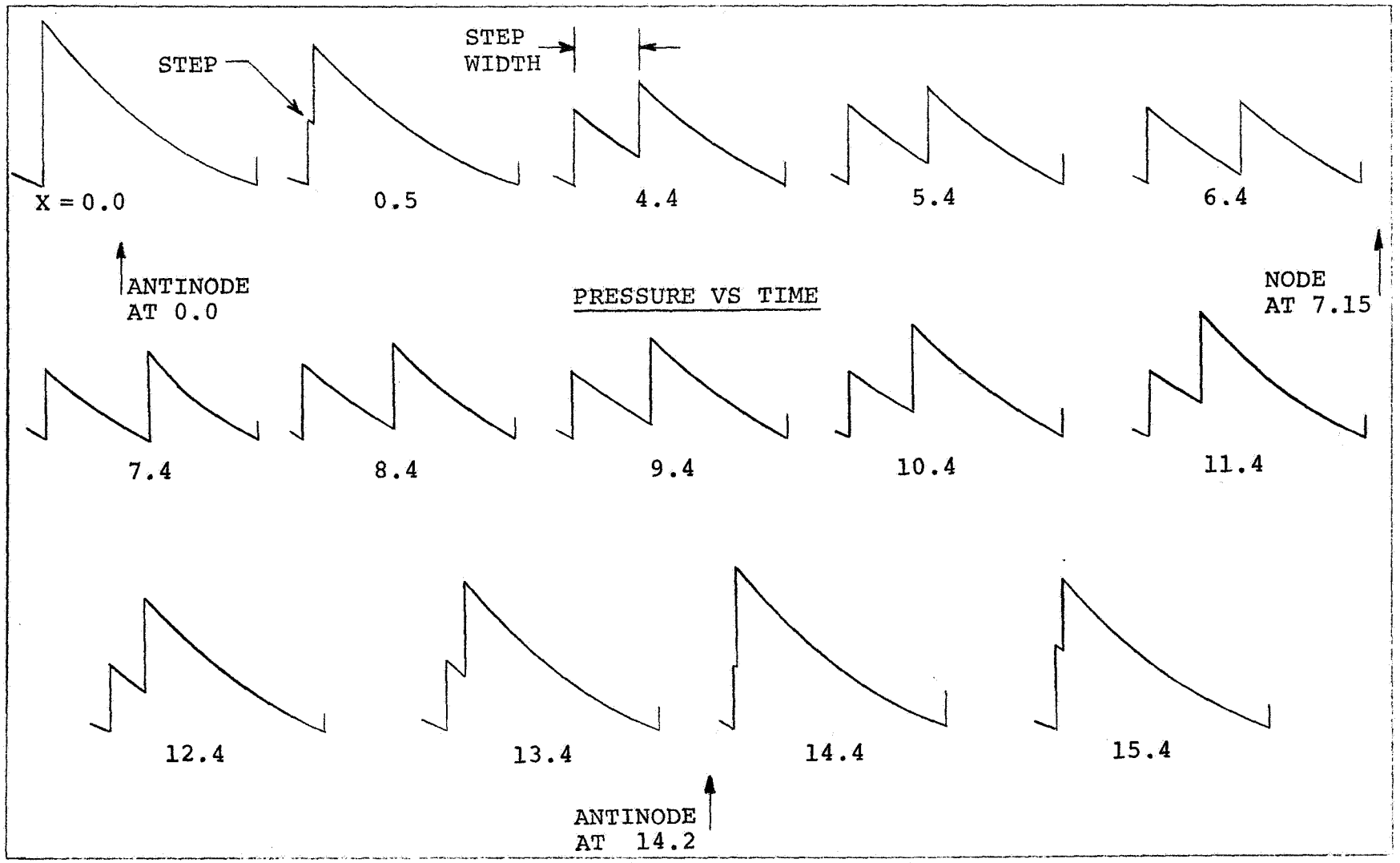

Fig. 3-10 Pressure Shapes at Various Locations in the Tube Near the Test Plate End - X Distance Measured in Inches from the Test Plate

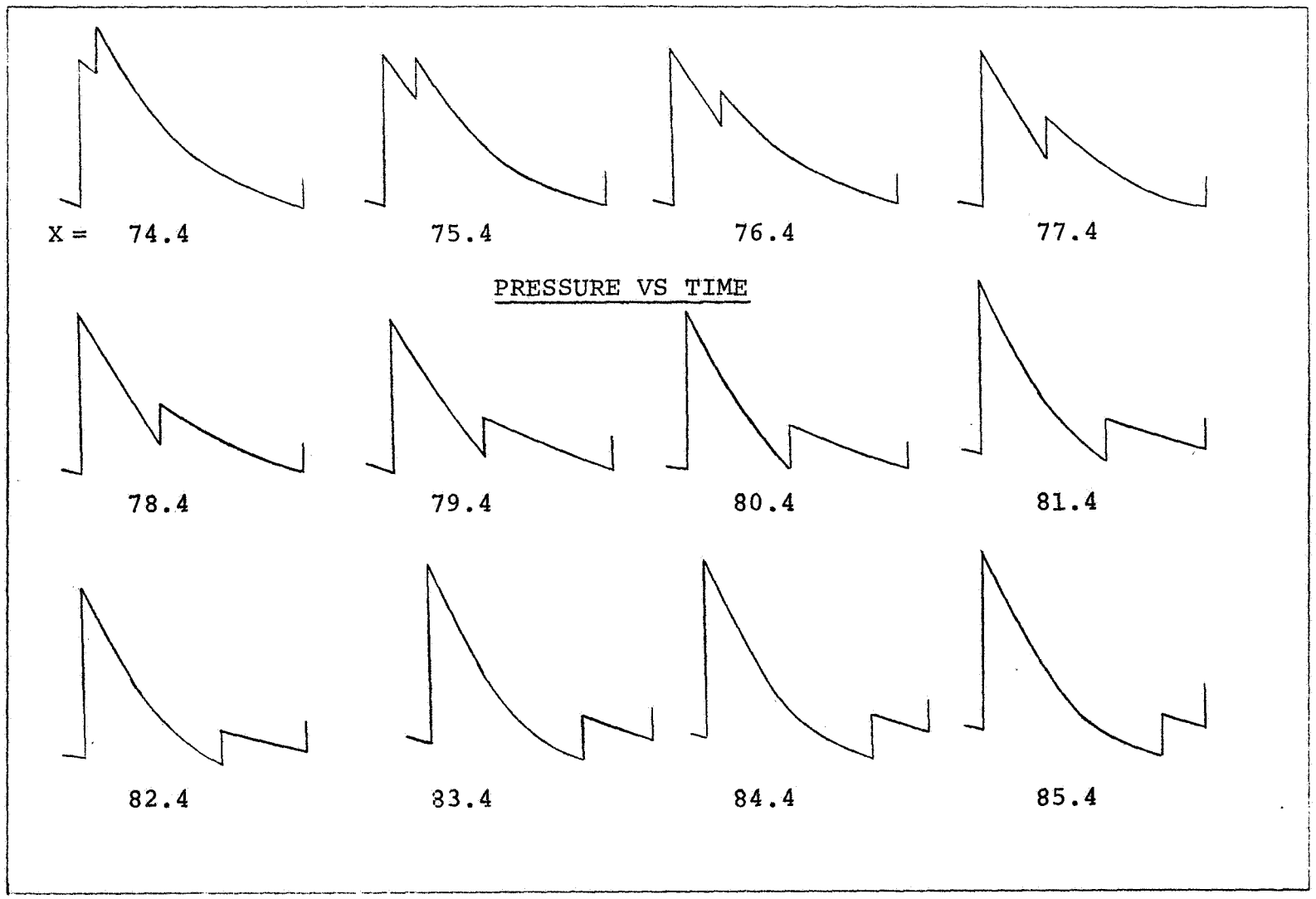

Fig. 3-11 Pressure Shapes at Various Locations in the Tube Near the Siren End - X Distance Measured in Inches from the Test Plate

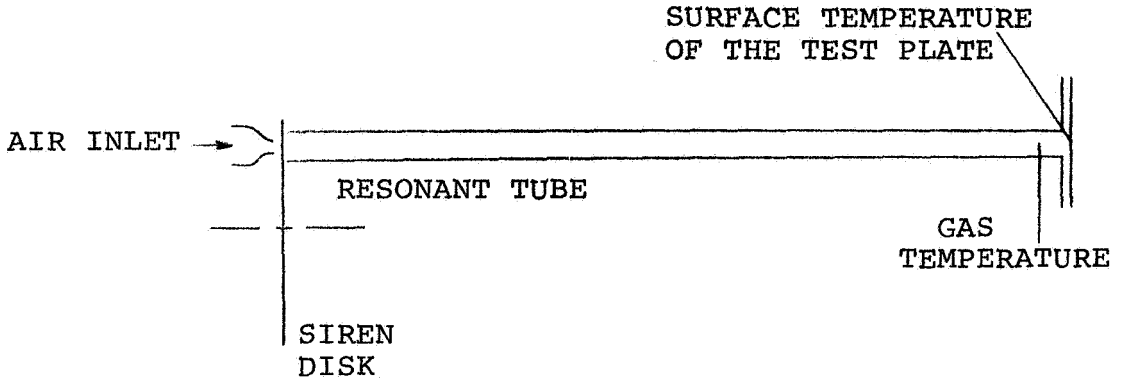

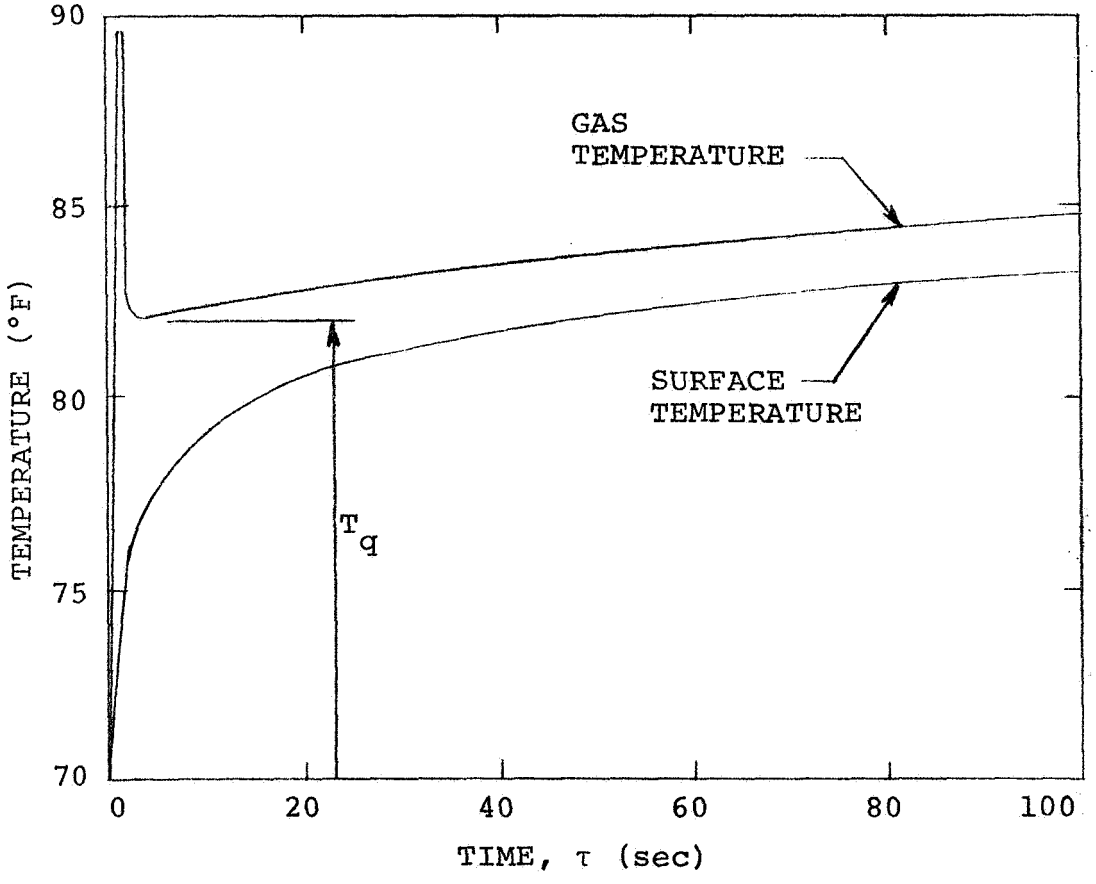

Fig. 3-12 Typical Gas Temperature and Surface Temperature Behavior

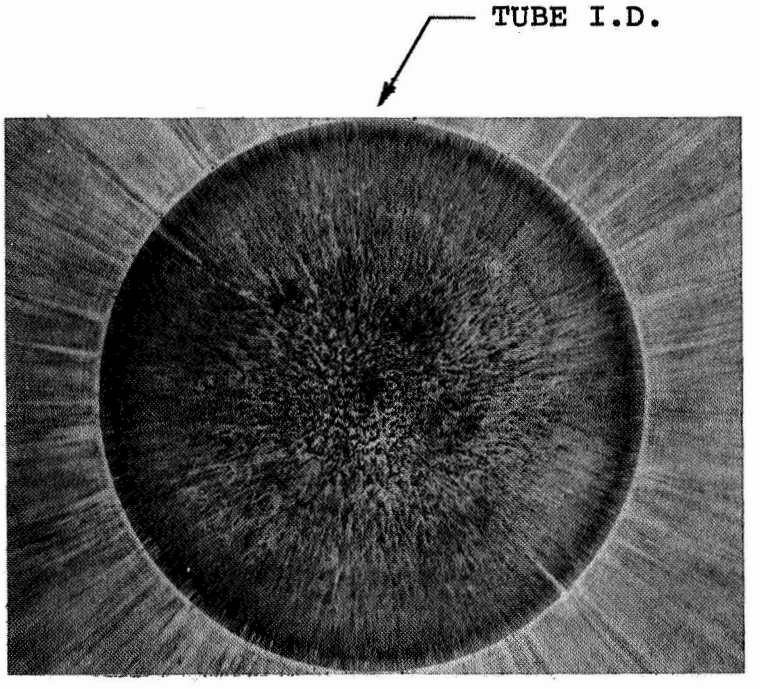

Fig. 3-13 Lampblack Pattern on Test Plate

CHAPTER FOUR

DATA REDUCTION

The experimental data consisted of instantaneous gas pressure and surface temperature measurements, which were displayed on an oscilloscope and photographically recorded. The data were then hand scaled from the photographs and instantaneous heat transfer rates numerically computed from the surface temperature measurements. The details of the data reduction process will now be discussed.

4-1 PRESSURE DATA

As was shown in Fig. 2-9, the fluctuations of the gas pressure were measured 0.5 in. upstream of the test plate. As was pointed out in Sec. 3-2, the pressure wave at that point exhibits a step in the pressure front which is not present in the wave front at the test plate. Simultaneous measurements of the pressure wave at the two locations are shown in Fig. 4-1.

The high frequency (130,000 Hz) noise which appears on the pressure signal results from the shock wave exciting the natural frequency of the pressure transducer. The lower frequency component of the noise results from vibration of the test plate holder in which the transducer was mounted.

Comparison of the two pressure waves in Fig. 4-1 shows that the shape of the pressure wave at the test plate can be obtained by extrapolation from the pressure measurement made 0.5 in. upstream. This extrapolation of the pressure data is shown in Fig. 4-2 by the dotted line. The absolute value of the pressure at any instant of time was then scaled from the photograph within three percent accuracy.

The rise time of the shock front was measured to be three microseconds - which is the rise time of the Kistler 601L pressure transducer used. Therefore, it is known that the rise time of the pressure wave is $\leq$ 3 microseconds, allowing it to be treated as a discontinuity.

4-2 SURFACE TEMPERATURE DATA

The surface temperature oscillations measured were quite small, ranging from 0.5 to 2.0 °F. Thus, the resulting temperature signals were also small, ranging from 0.1 to 0.4 mv, which made it necessary to amplify the signal one thousand times before it was displayed on the oscilloscope. A sample oscilloscope trace is shown in Fig. 4-3. In order to maintain an acceptable signal-to-noise ratio an Astrodata Model 885[1] wideband differential DC amplifier was used.

---

[1] Specifications:
Frequency response: Flat ± 0.5% DC to 1 kHz, down to 3 db at 10 kHz
Settling time: < 300 μsec to within ± .05% of final value
Noise: < 2 μv rms referred to the input and 250 μv referred to the output

Although the noise level of the amplifier was good, its frequency response was not great enough to follow the rapid rise of the surface temperature as caused by the arrival of the shock wave.

In an attempt to measure the rise time of the temperature signal, a Kintel Model 112A[1] DC amplifier was used. Although the shape of the temperature oscillation could not be discerned because of the high noise level of this amplifier, a rise time of approximately 10 microseconds could be measured. This was the rise time of the Kintel amplifier as well as the rise time of the platinum thin film. Therefore, the rise time of the temperature signal could only be determined to be $\leq$ 10 microseconds. As was done with the pressure signal, the surface temperature rise was treated as a discontinuity. The surface temperature signal was extrapolated as shown in Fig. 4-3. The overshoot in the surface temperature rise seen in Fig. 4-3 is a characteristic of the Astrodata amplifier and is not part of the temperature signal. The accuracy of the temperature measurements is estimated to be within five percent.

Due to the compression and expansion of the gas, the gas temperature fluctuates above and below the average plate temperature. Consequently, during a portion of the cycle,

---

[1]Specifications:
Frequency response: ± 0.5% to 2 kHz, ± 3% to 10 kHz, < 3 db down at 40 kHz
Rise time: <10 μsec to within 1%, 20 μsec to 0.1% of final value
Noise: 0-750 Hz, <5 μv rms; 0-50 kHz, <12 μv rms

heat is transferred to the plate, while during the remainder of the cycle, heat is transferred from the plate to the gas. During a test run, a net amount of heat was transferred to the plate - as was explained in Sec. 3-4.

The heat flux variation with time can be separated into two portions, as illustrated in Fig. 4-4: (1) a fluctuating portion where the net heat transfer per cycle is zero and (2) a positive, non-fluctuating portion. This separation into two portions is permissible because the differential equation governing the temperature distribution in the test plate is linear. There was only a small net heat transfer per cycle to the surface since the insulating properties of Pyrex caused its average temperature to approach the average gas temperature. The non-fluctuating portion of the heat flux was obtained by measuring the average surface temperature and subtracting from this the temperature of the Pyrex measured 0.062 in. from the surface. The non-fluctuating portion of the heat flux was then calculated from this temperature difference since the temperature profile in the Pyrex was linear. This temperature difference was only 2-3°F and therefore could not be accurately obtained from subtraction of the two separately measured temperatures. However, the above measurements did show that the magnitude of the non-fluctuating heat flux component ranged from 0.15-0.40 BTU/ft^2-sec, which was small compared to the fluctuating component.

The present investigation is limited to determining only the fluctuating portion of the heat flux since the non-fluctuating portion was small and could not accurately be determined with the present instrumentation. The method of calculation of the instantaneous heat transfer rates from the surface temperature measurements is described in the following section.

4-3 HEAT FLUX CALCULATIONS

In order to calculate the heat flux at the surface of the test plate from the measured surface temperature fluctuation, it is necessary to determine the time dependent temperature distribution in the Pyrex. The temperature gradient at the surface is then used to calculate the heat flux there. Since the temperature oscillations do not penetrate beyond 0.005 in. from the surface, the temperature distribution can be obtained by solving the heat conduction problem outlined in Fig. 4-5, where the thickness of the slab, ℓ, is greater than the thermal penetration depth. The experimentally measured surface temperature oscillation is applied to one side of the slab while the other side is held constant at the average temperature, $\bar{T}$, of that oscillation. From the periodic solution obtained, the instantaneous heat flux at the surface can be calculated. The partial differential equation describing the above one-dimensional, unsteady heat conduction problem is

$$\frac{1}{\alpha}\frac{\partial T}{\partial t} = \frac{\partial^2 T}{\partial x^2} \tag{4-1}$$

The boundary conditions for this problem are

$$\begin{aligned} T(0,t) &= f(t) \\ T(\ell,t) &= \bar{T} \end{aligned} \tag{4-2}$$

with the initial condition

$$T(x,0) = \bar{T}. \tag{4-3}$$

This problem was numerically solved by the Crank-Nicolson implicit method. In this method, Eq. 4-1 is approximated by

$$\frac{T_{i,j+1} - T_{i,j}}{\alpha\Delta t} = \frac{1}{2}\left\{\frac{T_{i+1,j+1} - 2T_{i,j+1} + T_{i-1,j+1}}{(\Delta x)^2} + \frac{T_{i+1,j} - 2T_{i,j} + T_{i-1,j}}{(\Delta x)^2}\right\} \tag{4-4}$$

where

subscript (i) is the distance index and

subscript (j) is the time index.

For N increments in x Eq. 4-4 yields N equations at each time increment - with N unknowns, as is readily seen by rearranging Eq. 4-4.

$$-r\,T_{i-1,j+1} + (2+2r)T_{i,j+1} - r\,T_{i+1,j+1} =$$

The above temperatures are to be determined at the future time (j+1)

(4-5)

$$r\,T_{i-1,j} + (2-2r)T_{i,j} + r\,T_{i+1,j}$$

The above temperatures are known at the present time (j)

where

$$r = \frac{\alpha\Delta t}{(\Delta x)^2} \qquad i = 1,2, \ldots, N \qquad j = 1,2, \ldots, M$$

For each time increment the set of N equations was solved by the Gauss elimination method, which results in the Thomas algorithm (Bruce). The heat flux was determined by

$$q_{w,j+1} = k\left(\frac{T_{0,j+1} - T_{1,j+1}}{\Delta x}\right) \quad j = 1,2, \ldots, M \qquad (4\text{-}6)$$

In all of the calculations the thickness of the slab was taken to be 0.0115 in., which was approximately twice the penetration depth. Near the surface at x=0, where the temperature gradients are largest, the slab was divided into 0.05×10^{-3} in. increments. At a depth of 0.0015 in., where the temperature gradients are small, the increment size was changed to 0.5×10^{-3} in.

Initially, the temperature of the slab was set equal to the average surface temperature, $\bar{T}$. The surface temper-

ature at x=0 was then cycled until a steady periodic temperature variation was established in the slab.

In order to avoid instability in the solution, it was necessary to divide each cycle into 400 time increments, yielding a value of r equal to 2.24. This division resulted in a time increment of 5.2 microseconds at a frequency of 479 Hz. An estimation of the accuracy of the numerical solution was obtained by progressively decreasing the x increment size and extrapolating to an increment size of zero. For the increment sizes that were used for all of the data reduction, the heat flux was found to be calculated within an accuracy of one percent.

The thermal diffusivity and the thermal conductivity for No. 7740 Pyrex is needed for Eqs. 4-5 and 4-6. G.T. Skinner, at the Cornell Aeronautical Laboratory, and others have developed a technique for experimentally determining the quantity $(k\rho c)^{1/2}$. Skinner found that

$$(k\rho c)^{1/2} = 0.0743 \pm 5\% \text{ BTU/ft}^2\text{-°F-sec}^{1/2} \qquad (4\text{-}7)$$

The value of the thermal diffusivity, $\alpha = 0.00107$ in.^{2}/sec, was taken from the Corning Glass Works Property Data Sheet on No. 7740 Pyrex. Using the above two values, the thermal conductivity, k, can be calculated

$$k = \alpha^{1/2} (k\rho c)^{1/2} = 0.729 \text{ BTU/hr-ft-°F}$$

The cyclic heat flux variation calculated in the above manner for Run 220 is shown for one cycle in Fig. 4-6. The normalized time against which the heat flux, q_w, is plotted is obtained by dividing the actual time in the cycle by the period of that cycle. The shock arrives at the wall at time zero, after which the compressed gas transfers heat to the wall. As expansion of the gas takes place the heat flux decreases, passes through zero, and becomes negative for the remainder of the cycle. As was previously discussed in Sec. 4-2, only the fluctuating portion of the heat flux is being considered, and therefore, the net heat transferred per cycle is zero.

The two quantities τ_c and Q_{pos} are used to characterize the unsteady heat flux variation. The normalized time, τ_c, denotes the fraction of the cycle during which heat is transferred from the gas to the wall. During this part of the cycle, the heat flux, q_w, is taken to be positive. The amount of energy transferred to the wall during the τ_c fraction of the cycle is denoted as Q_{pos} and can be calculated from:

$$Q_{pos} = \frac{1}{f}\int_0^{\tau_c} q_w \, d\tau \qquad (4\text{-}8)$$

where

f = frequency

q_w = heat flux at the wall

τ = normalized time.

Although the heat flux rates are large in Fig. 4-6, Q_{pos} is only 1.93×10^{-3} BTU/ft^2. The reason for the small value of Q_{pos} is that, at the frequencies used in this investigation, the time available for heat transfer is small. It was found that typically the heat was transferred to the surface during the first third of the cycle and then returned to the gas during the remainder of the cycle. As would be expected, the maximum heat flux occurs immediately after the shock wave strikes the surface. The heat flux then decreases rather sharply due to the expansion of the gas. The surface temperature fluctuation scaled from the data and used to calculate the above heat flux variation is given in Fig. 4-7. The calculated temperature distributions in the slab at several times during the cycle are plotted in Fig. 4-8. From this figure it can be seen that the temperature fluctuations are damped out within 0.005 in. of the surface.

The calculations were performed on a CDC 1604 computer, with a resulting computation time of thirty seconds per cycle. It was necessary to cycle the program ten times before a steady periodic solution was obtained. Each run required about five minutes of computer time.

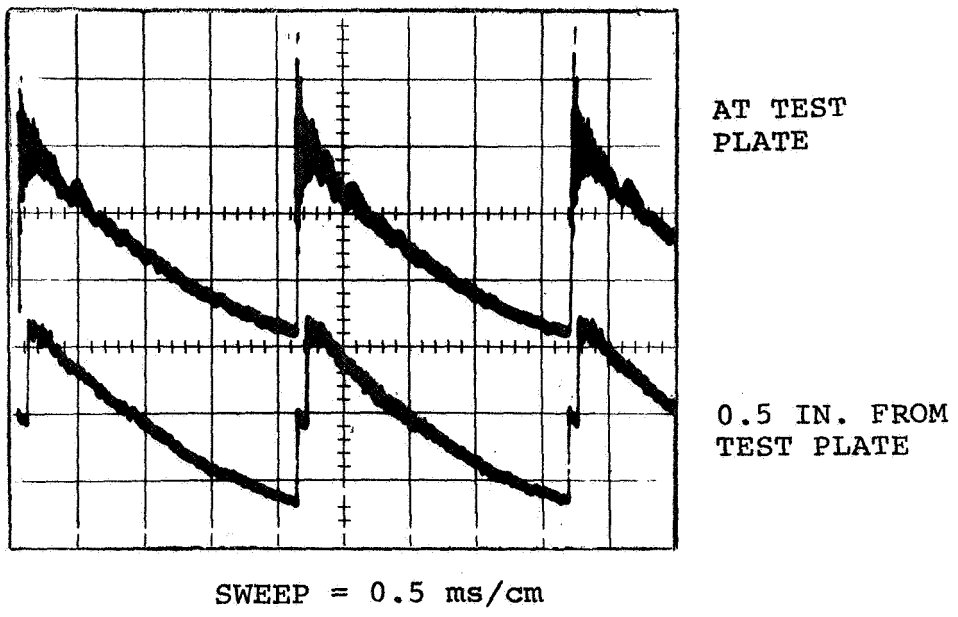

Fig. 4-1 Experimental Pressure Traces

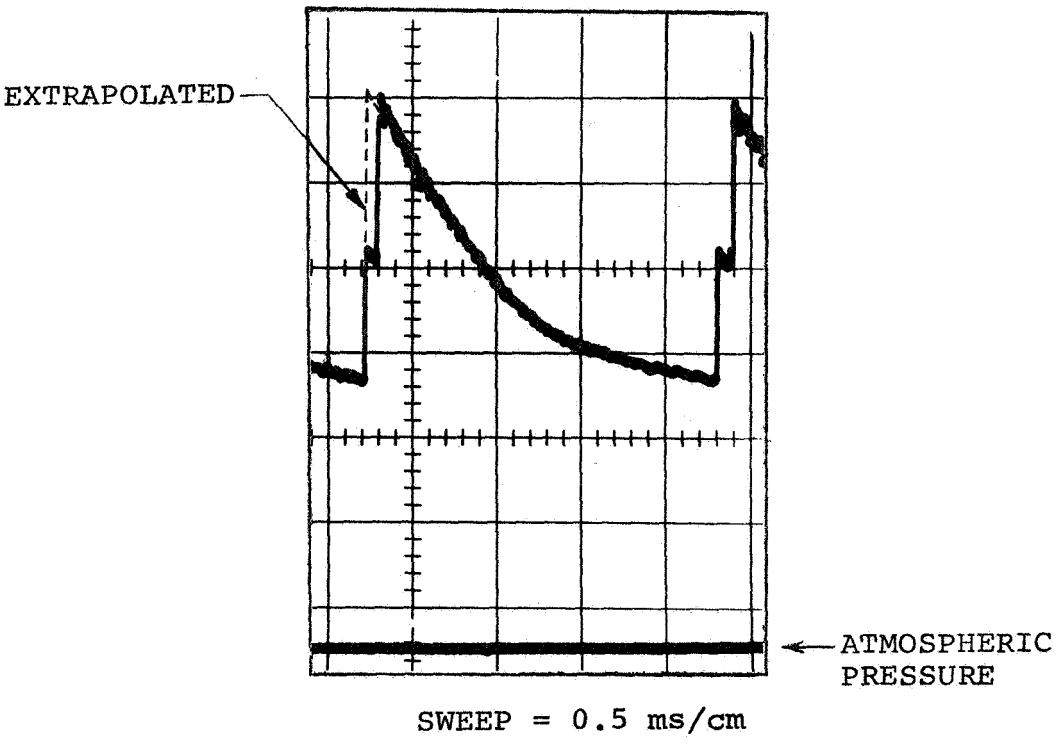

Fig. 4-2 Experimental Pressure Data with Extrapolation

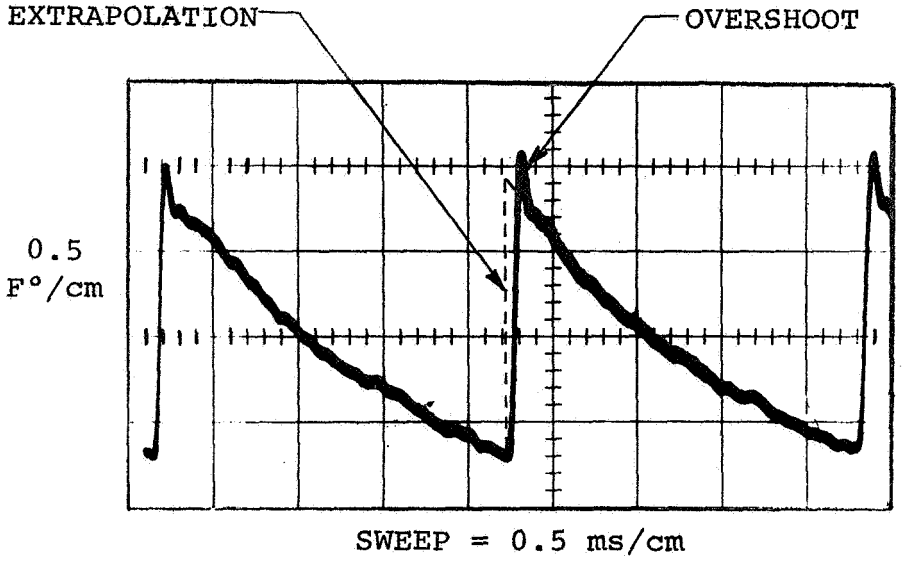

Fig. 4-3 Experimental Surface Temperature Oscillation

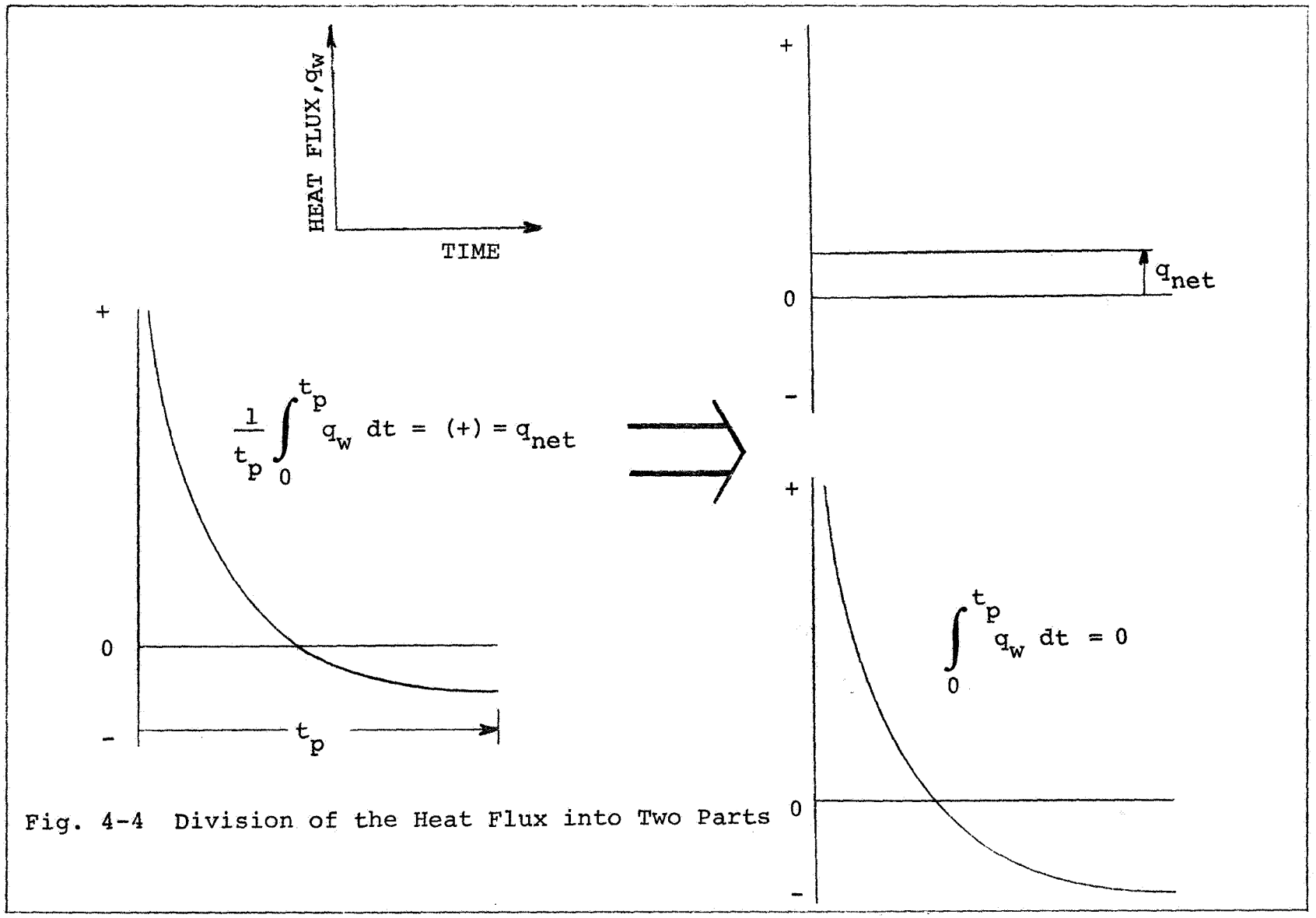

Fig. 4-4 Division of the Heat Flux into Two Parts

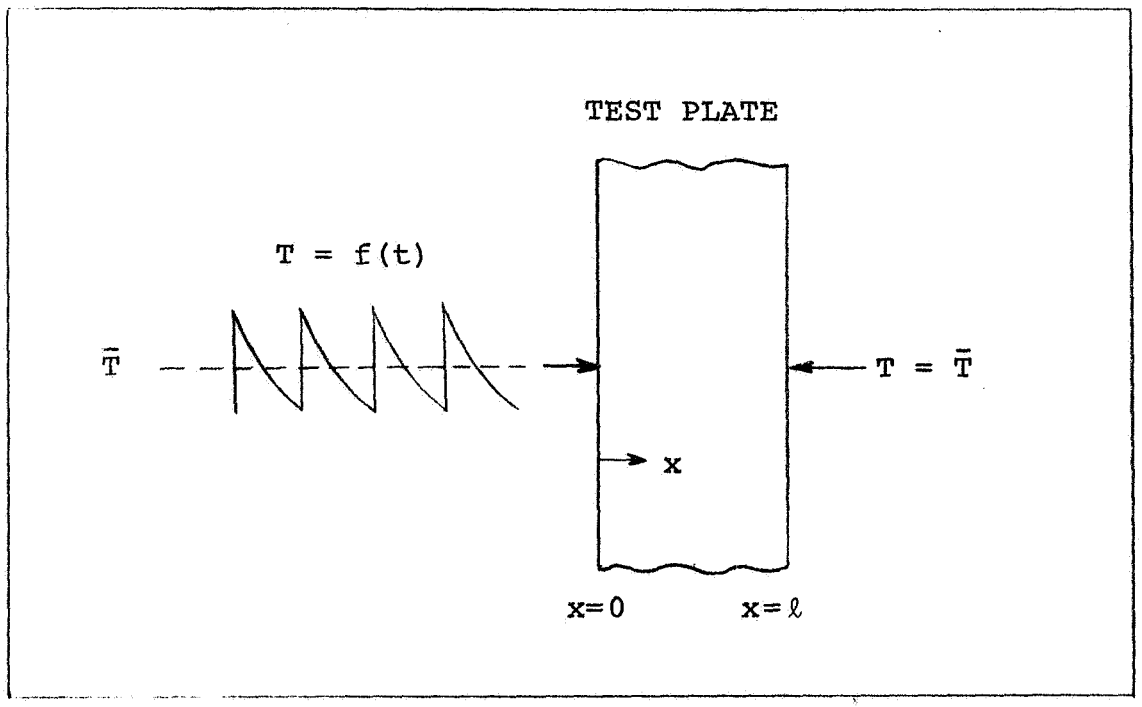

Fig. 4-5 Heat Conduction Problem in the Test Plate

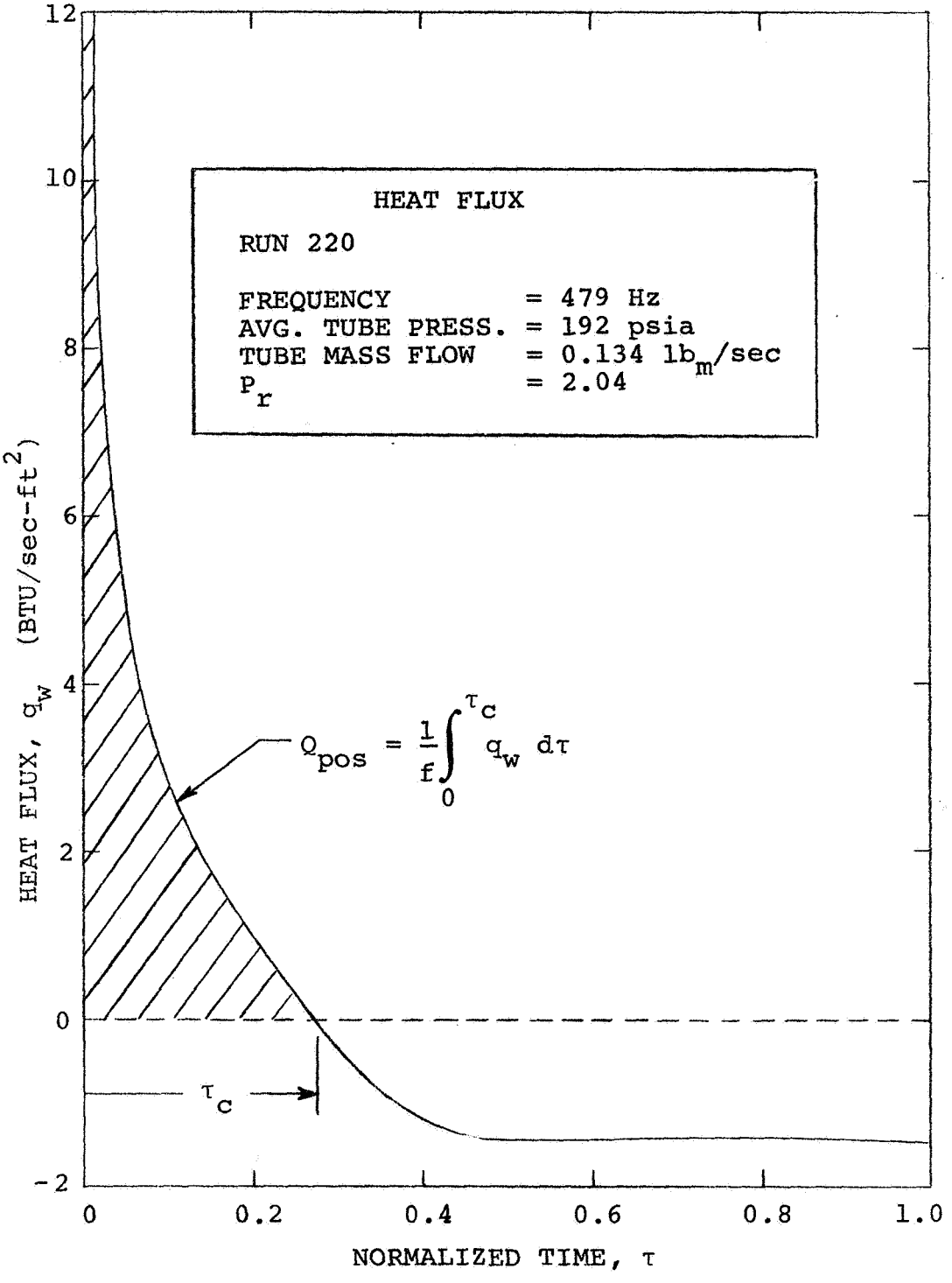

Fig. 4-6 Heat Flux Variation for Run 220

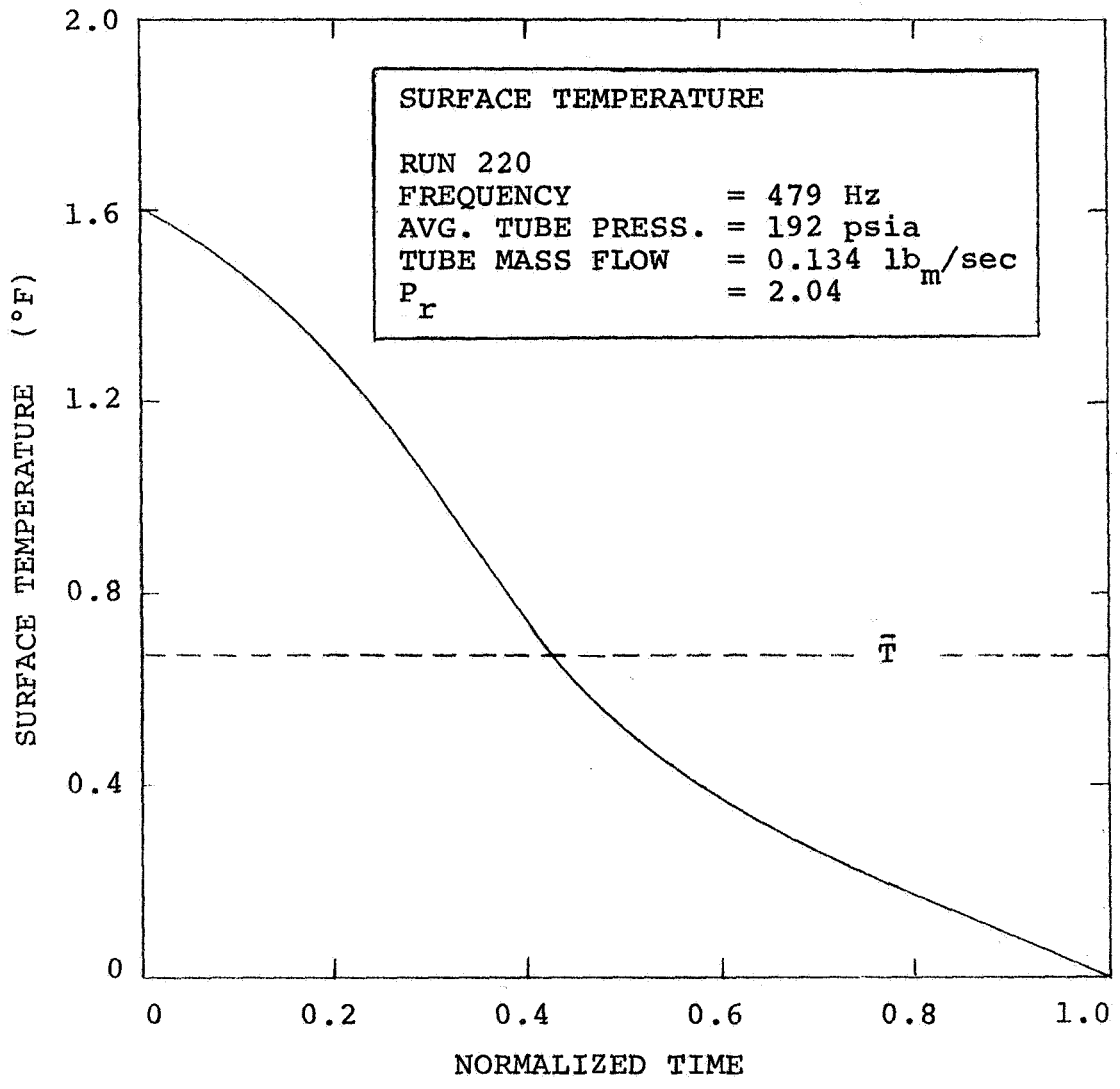

Fig. 4-7 Surface Temperature Oscillation for Run 220

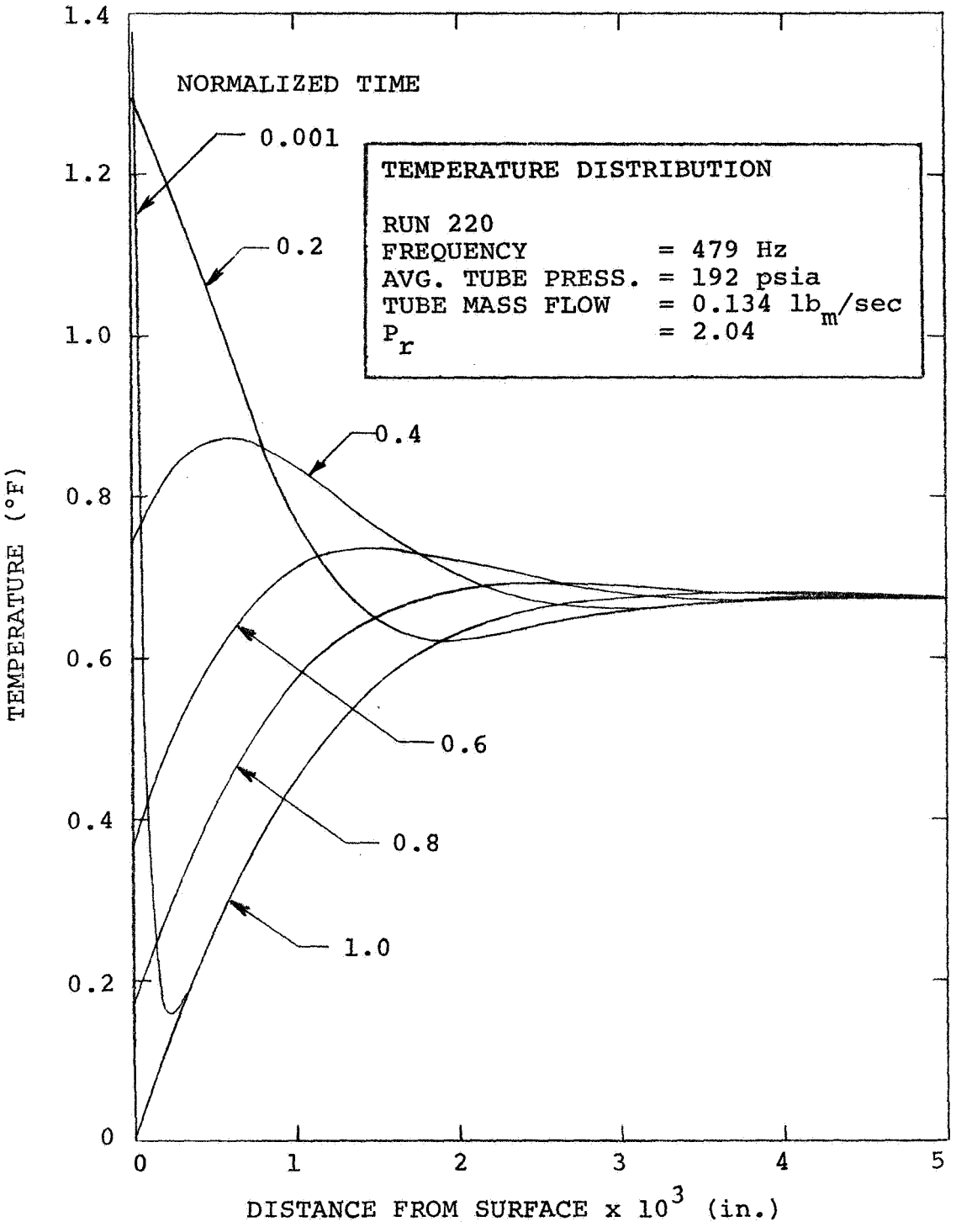

Fig. 4-8 Temperature Distribution in the Test Plate for Run 220

CHAPTER FIVE

THEORETICAL MODEL

A theoretical model was developed to predict the cyclic variation of the heat flux at the test plate which forms the end-wall of the tube. The heat flux variation with time is calculated so that there is no net heat transfer per cycle. The solution of the governing differential equations was numerically obtained by use of a finite difference predictor-corrector method. The assumptions used in the analysis are similar to those made by B.T. Chao for heat transfer at the end of rarefaction wave tubes.

5-1 ANALYSIS

As previously discussed, the test plate is located normal to the tube outlet (see Fig. 5-1). The pressure at the plate fluctuates at a frequency in the range of 479-881 Hz causing the gas next to the plate to alternately experience a compression and expansion. Air is bled from the tube at its periphery by maintaining a small gap between the test plate and the end of the tube. It is intuitive that, for small plate gaps, the presence of the air bleed does not significantly alter the fluid flow near $x = 0$ from what it would be if the end were closed.

Therefore, the flow near $r = 0$ is assumed to be one-dimensional. Moreover, it will be shown in Chapter Six that for the plate gaps used in this investigation, the unsteady portion of the heat flux can be predicted by a one-dimensional mathematical model of the system. The ratio of the tube radius to the gap thickness varied from 12 to 50 in this investigation.

For an ideal gas, with negligible dissipation, the one-dimensional, unsteady energy equation for laminar flow is:

$$c_p\rho \left(\frac{\partial T}{\partial t} + u \frac{\partial T}{\partial x}\right) = \frac{\partial P}{\partial t} + u \frac{\partial P}{\partial x} + \frac{\partial}{\partial x}\left(k \frac{\partial T}{\partial x}\right) \qquad (5\text{-}1)$$

where x is the distance measured from the surface of the test plate. Since the equations are applied to a thin thermal boundary layer next to the test plate - where the turbulent velocity fluctuations should be small, laminar equations can be used.

For a thin boundary layer the pressure can be assumed to be independent of x. In addition, the specific heat, c_p, and the thermal conductivity, k, are assumed constant. With the above assumptions, Eq. 5-1 becomes

$$c_p\rho \left(\frac{\partial T}{\partial t} + u \frac{\partial T}{\partial x}\right) = \frac{dP}{dt} + k \frac{\partial^2 T}{\partial x^2} \qquad (5\text{-}2)$$

The process outside the thermal boundary layer is considered to be isentropic so that the temperature there can be expressed as

$$T_\infty = T_0 (P/P_0)^{\frac{\gamma-1}{\gamma}} \tag{5-3}$$

where P_0 and T_0 are the minimum gas pressure and gas temperature for the cycle. The subscript ∞ has been dropped from P in Eq. 5-3 since the pressure is considered to be independent of x. Once the pressure variation with time is prescribed, the gas temperature variation with time outside the thermal boundary layer is determined by Eq. 5-3. Because the surface temperature measured at the test plate never fluctuated more than 2°F and the gas temperature fluctuation is on the order of 100°F, the surface temperature, T_w, can safely be considered constant in this analysis. The boundary conditions can then be summarized as

$$T(0,t) = T_w, \qquad T(\infty,t) = T_\infty = T_0 (P/P_0)^{\frac{\gamma-1}{\gamma}} \tag{5-4}$$

Because the pressure variation is cyclic and the steady periodic solution is desired, the initial condition can be replaced by

$$T(x,t) = T(x,\ t + t_p) \tag{5-5}$$

where t_p is the period of the cycle.

An expression for the velocity, u, in Eq. 5-2 is obtained from the one-dimensional continuity equation.

$$\frac{\partial \rho}{\partial t} + \frac{\partial (\rho u)}{\partial x} = 0 \tag{5-6}$$

An approximate expression for u can be obtained from Eq. 5-6 by assuming that the density, ρ, is independent of x and equal to the gas density at the outer edge of the boundary layer, ρ_∞. The validity of this assumption is discussed in Sec. 6-6. Therefore, for the continuity equation only, the density in Eq. 5-6 may be replaced by the isentropic relationship

$$\rho_\infty = \rho_0 (P/P_0)^{1/\gamma} \tag{5-7}$$

Using the boundary condition that u = 0 at x = 0, Eq. 5-6 (with Eq. 5-7) may be integrated to yield the following velocity distribution:

$$u = -\frac{1}{\gamma}\frac{\dot{P}}{P} x \tag{5-8}$$

Since the coefficient of x is a function of time alone, Eq. 5-8 describes, at any given time, a linear velocity profile in x. For an ideal gas,

$$\rho = P/(RT) \tag{5-9}$$

$$\frac{R}{c_p} = \frac{\gamma-1}{\gamma} \tag{5-10}$$

Substitution of Eqs. 5-8, 5-9, and 5-10 into Eq. 5-2 and rearrangement gives

$$\frac{\partial}{\partial t}\left[\ell n (T/P^{\frac{\gamma-1}{\gamma}})\right] - \frac{1}{\gamma}\frac{\dot{P}}{P}\frac{x}{T}\frac{\partial T}{\partial x} = \frac{R}{c_p}\frac{k}{P}\frac{\partial^2 T}{\partial x^2} \tag{5-11}$$

The following dimensionless variables can be defined:

$$y = T/T_\infty = (T/T_0)(P/P_0)^{\frac{1-\gamma}{\gamma}}, \quad z = x/\delta, \quad \tau = tf \qquad (5\text{-}12)$$

where f is the frequency of the pressure oscillation and δ is a distance, at this point not yet defined, that is a function of time. At any given time, the dimensionless variable, y, is the ratio of the gas temperature in the boundary layer, T(x,t), to the gas temperature outside the boundary layer, $T_\infty = T(\infty,t)$. Therefore, y is the ratio of the gas temperature to the gas temperature that would be obtained isentropically.

Introducing the new variables into Eq. 5-11 and applying the chain rule[1] to the partial derivatives yields

$$\frac{f}{y}\frac{\partial y}{\partial \tau} - \left(\frac{\dot{\delta}}{\delta} + \frac{1}{\gamma}\frac{\dot{P}}{P}\right)\frac{z}{y}\frac{\partial y}{\partial z} = \frac{R}{c_p}\frac{k}{\delta^2}\left(\frac{T_0}{P_0}\right)\left(\frac{P}{P_0}\right)^{-\frac{1}{\gamma}}\frac{\partial^2 y}{\partial z^2} \qquad (5\text{-}13)$$

where $\dot{\delta}$ and $\dot{P}$ are first derivatives with respect to t. To eliminate the second term on the left-hand side of Eq. 5-13,

---

[1]The chain rule gives

$$\left.\frac{\partial y}{\partial t}\right|_x = \left.\frac{\partial y}{\partial \tau}\right|_z \frac{d\tau}{dt} + \left.\frac{\partial y}{\partial z}\right|_\tau \left.\frac{\partial z}{\partial t}\right|_x$$

$$\left.\frac{\partial y}{\partial x}\right|_t = \left.\frac{\partial y}{\partial z}\right|_\tau \left.\frac{\partial z}{\partial x}\right|_t$$

$$\left.\frac{\partial^2 y}{\partial x^2}\right|_t = \frac{\partial}{\partial z}\left(\left.\frac{\partial y}{\partial x}\right|_t\right)\Bigg|_\tau \left.\frac{\partial z}{\partial x}\right|_t$$

δ is chosen to be defined as

$$\frac{\dot{\delta}}{\delta} \equiv -\frac{1}{\gamma}\frac{\dot{P}}{P} \tag{5-14}$$

An expression for δ can be obtained by integrating Eq. 5-14 and letting $\delta = \delta_0$ when $P = P_0$

$$\delta = \delta_0 \left(\frac{P}{P_0}\right)^{-1/\gamma} \tag{5-15}$$

The right-hand side of Eq. 5-13 can be simplified by noting that for an ideal gas

$$\rho_0 = P_0/(RT_0) \tag{5-16}$$

and that the thermal diffusivity (α_0) is defined as

$$\alpha_0 = k/(c_p\rho_0) \tag{5-17}$$

When Eqs. 5-14, 5-15, 5-16, and 5-17 are substituted into Eq. 5-13, the following form results

$$\frac{1}{y}\frac{\partial y}{\partial \tau} = \frac{\alpha_0}{f\,\delta_0^{\,2}}\left(\frac{P}{P_0}\right)^{1/\gamma}\frac{\partial^2 y}{\partial z^2} \tag{5-18}$$

Equation 5-18 can be further simplified by defining δ_0 such that

$$\alpha_0/(f\delta_0^{\,2}) \equiv 1 \tag{5-19}$$

With the above definition for δ_0, Eq. 5-15 can be written as

$$\delta = (\alpha_0/f)^{1/2}\,(P/P_0)^{-1/\gamma} \tag{5-20}$$

and Eq. 5-18 becomes

$$\frac{1}{y}\frac{\partial y}{\partial \tau} = \left(\frac{P}{P_0}\right)^{1/\gamma}\frac{\partial^2 y}{\partial z^2} \tag{5-21}$$

In terms of the dimensionless variables, the boundary conditions, Eq. 5-4, become

$$y(0,\tau) = (T_w/T_0)(P/P_0)^{\frac{1-\gamma}{\gamma}}, \quad y(\infty,\tau) = 1 \tag{5-22}$$

The periodicity condition, Eq. 5-5, becomes

$$y(z,\tau) = y(z,\tau + 1) \tag{5-23}$$

In addition, the heat flux at the wall is given by

$$q_w = -k\left.\frac{\partial T}{\partial x}\right|_{x=0} \tag{5-24}$$

and can be written in terms of the new variables as

$$q_w = -T_0 f^{1/2}(k\rho_0 c_p)^{1/2}\left(\frac{P}{P_0}\right)\left.\frac{\partial y}{\partial z}\right|_{z=0} \tag{5-25}$$

Equation 5-21 with the boundary conditions given by Eq. 5-22 and the periodicity condition given by Eq. 5-23 can be solved numerically by replacing the $y(\infty,\tau) = 1$ boundary condition by $y(z_\ell,\tau) = 1$ where z_ℓ is taken large enough to be outside the thermal boundary layer. The variation of the pressure with time, $P(\tau)$, in the boundary condition at $z = 0$ can be assumed or provided from experimental data.

Douglas and Jones modified the Crank-Nicolson procedure to obtain a predictor-corrector method applicable to such nonlinear parabolic differential equations. Their method of calculation was used to solve Eq. 5-21. The predictor equation is given by

$$y_{i-1,j+1} - \left(2 + \frac{B}{y_{i,j}}\right) y_{i,j+1} + y_{i+1,j+1} = -B \qquad (5\text{-}26)$$

where

$$B = \frac{2(\Delta z)^2}{\Delta\tau}\left(\frac{P}{P_0}\right)^{-1/\gamma}_{j+1}$$

with subscript (i) the z index and subscript (j) the τ index.

The corrector equation is given by

$$y_{i-1,j+2} - \left(2 + \frac{B}{y_{i,j+1}}\right) y_{i,j+2} + y_{i+1,j+2} = BC \qquad (5\text{-}27)$$

where

$$BC = -y_{i-1,j} + \left(2 - \frac{B}{y_{i,j+1}}\right) y_{i,j} - y_{i+1,j}$$

The equations given by Eq. 5-26 for a fixed value of j and

variable i form a tridiagonal matrix that can be solved by the Gauss elimination method, which results in the Thomas algorithm (Bruce). The predicted values of y are then corrected by application of Eq. 5-27, which again results in a tridiagonal matrix solved in the same manner as was Eq. 5-26. The $y_{i,j}$ values are known at $\tau = 0$. These $y_{i,j}$ values are then used to predict the $y_{i,j+1}$ values at $\tau = \Delta\tau/2$. The corrected values, $y_{i,j+2}$, can then be calculated at $\tau = \Delta\tau$ utilizing the values of $y_{i,j}$ and $y_{i,j+1}$. By repeated use of Eqs. 5-26 and 5-27 the solution for y can be obtained at each of the $\Delta\tau$ increments. The problem is cycled until a steady periodic solution is obtained.

Douglas and Jones proved that if y is bounded through its fourth derivative, the above predictor-corrector method is uniformly convergent, with an error that is $O(\Delta z^2 + \Delta\tau^2)$. However, in the present case, because of the discontinuity in the shock front, the numerical solution was unstable unless a fine $\Delta\tau$ increment was used. The thermal boundary layer was divided into fifty increments giving $\Delta z = 0.055$. In order to obtain stability with this choice of Δz, it was necessary to use $\Delta\tau = 0.001$ for $0 \leq \tau \leq 0.05$, and $\Delta\tau \leq 0.003$ for $0.05 \leq \tau \leq 1.0$. Using the above increment sizes, no instabilities were encountered. The time increments were taken such that the pressure was increased from its minimum value at $\tau = 0$ to its maximum value at $\tau = 0.001$. Based on this time increment, the rise time of the pressure wave in the finite difference solution was

2.1 microseconds at a frequency of 479 Hz, which is within the three microseconds rise time that was measured. For all of the calculations presented in Chapter Six, z_ℓ was taken to be equal to 2.75 which was found to always be large enough to be outside the thermal boundary layer.

In the theoretical model there are no means provided by which a net amount of energy can be exchanged between the system and its surroundings. The outer boundary of the system is adiabatic since y approachs the value of one asymptotically and therefore $\left.\frac{\partial y}{\partial z}\right|_{z=z_\ell}$ approaches zero. In the continuity equation, to obtain an approximate expression for the velocity, u, the gas density was assumed independent of x and equal at any time to the density at the outer boundary of the system, where the gas is assumed to be undergoing an isentropic compression and expansion. As a consequence of this assumption, the motion of the outer boundary of the system is prescribed as if the entire gas within the system were undergoing an isentropic compression and expansion process. Since the compression and expansion process is along the same path, the net pressure work at the outer boundary of the system is zero. Therefore, to be consistent with the theoretical model, which does not allow for any energy addition to the system at the outer boundary, T_0 must be chosen so that the net amount of heat transferred at the wall per cycle is zero.

The assumption of a density independent of x in the continuity equation enters directly into the energy equation only through use of an approximate expression for the velocity, u. Indirectly, the assumption enters into the energy equation by requiring that T_0 be chosen so that there is no net heat transfer at the wall. The limitation of the theoretical model to the case of a zero net heat transfer at the wall is more fully discussed in Sec. 6-6.

A good estimate for T_0 can be obtained by choosing T_0 such that the time-averaged gas temperature outside the thermal boundary layer is equal to the wall temperature. The time-averaged gas temperature, $\bar{T}_\infty$, outside the boundary layer is given by

$$\bar{T}_\infty = T_0 \int_0^1 (P/P_0)^{\frac{\gamma-1}{\gamma}} \, d\tau \tag{5-28}$$

Substituting $\bar{T}_\infty = T_w$ into Eq. 5-28, and solving for T_0 yields

$$T_0 = \frac{T_w}{\int_0^1 \left(\frac{P}{P_0}\right)^{\frac{\gamma-1}{\gamma}} d\tau} \tag{5-29}$$

This estimate for T_0 was found to be within 25°R of the T_0 value necessary for a zero net heat transfer per cycle.

The computing time amounted to 50 seconds per cycle on a CDC 1604 computer. The initial condition $y(z,0) = 1$ was used to start the computer program. The program was cycled until a steady periodic solution developed, which usually required six to eight cycles.

The theoretical model is compared with the experimental data in Chapter Six.

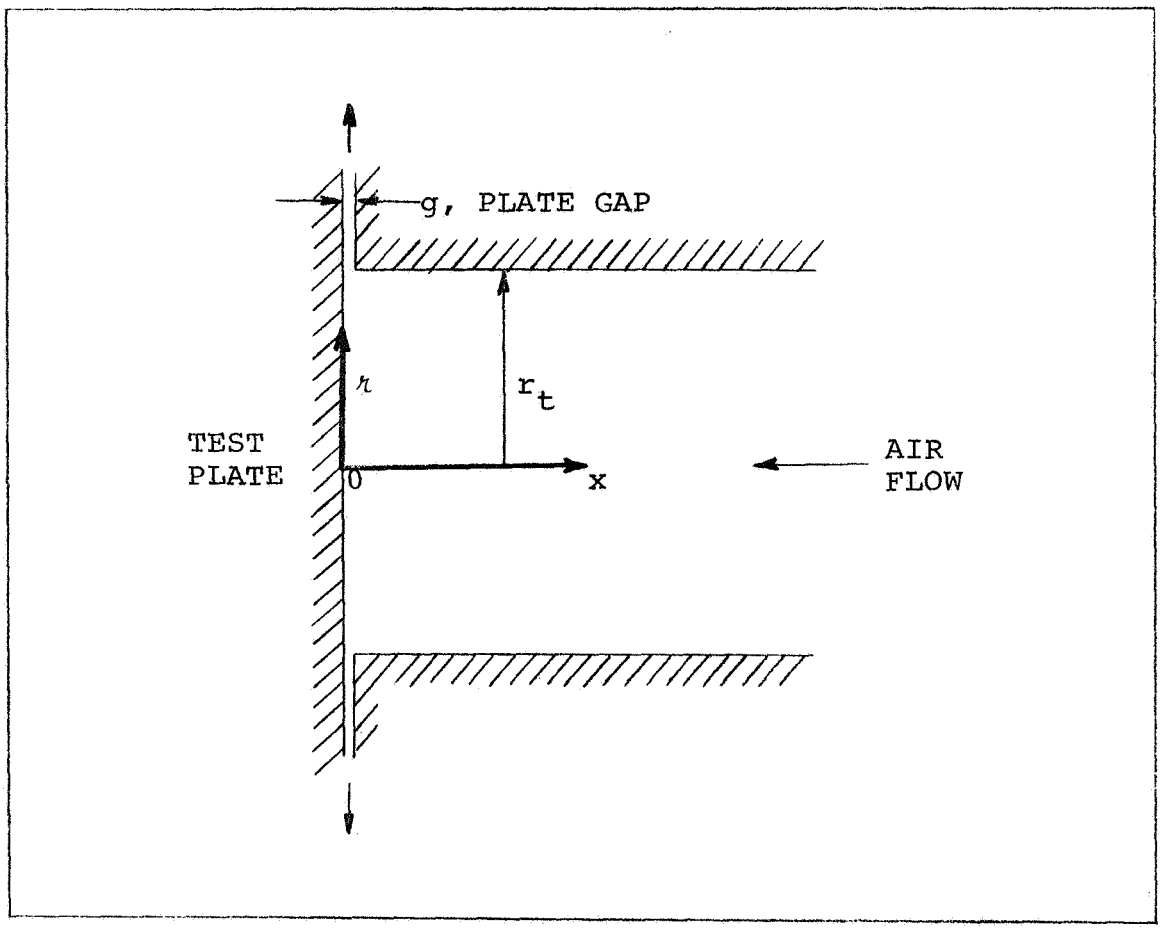

Fig. 5-1 Test Section Coordinates

CHAPTER SIX

COMPARISON OF THE THEORETICAL MODEL WITH EXPERIMENTAL DATA AND CONCLUSIONS

In this chapter, the results of the theoretical model are compared with the experimental data. The effects of the average[1] tube pressure, $\bar{P}$, the pressure ratio across the wave, P_r, and the frequency of the wave, f, on the heat flux at the end-wall are discussed. The validity of the assumptions made in the theoretical model are then discussed and the chapter ends with a summary of the conclusions.

6-1 TYPICAL SET OF EXPERIMENTAL DATA

The experimental heat flux variations with time are shown in Fig. 6-1 for a typical set of three data runs at different values of P_r. For these data runs the average tube pressure, frequency, and mass flow rate were fixed. The heat flux variations shown in Fig. 6-1 were calculated from the experimentally measured surface temperature fluctuations given in Fig. 6-2. The magnitude of the heat flux increases with an increase in P_r, resulting in an increase in the amplitude of the surface temperature fluctuations. The corresponding measured gas pressure oscillations are shown in Fig. 6-3. The shapes of the gas pressure and the

---

[1] In this discussion all averages refer to time-averages.

surface temperature oscillations are compared in Fig. 6-4. As was previously mentioned in Sec. 3-2, the shape of the pressure wave varied from one run to another. However, the shapes of the pressure waves and the surface temperature fluctuations varied within a narrow band, as is shown in Fig. 6-4. This data set is compared in Fig. 6-9 with two other data sets, which were obtained at different average tube pressures.

6-2 PREDICTED HEAT FLUX VARIATION WITH TIME

In Fig. 6-5 the predicted heat flux variation with time is compared with that experimentally obtained for Run 213. It can be seen that the theoretical model adequately predicts the heat flux variation. The heat flux at time zero is infinite if the pressure wave is considered to be discontinuous at that point in the cycle. However, the heat flux predicted from the theoretical model at that time in the cycle was finite because a finite difference solution requires that a finite rise time be used. As previously discussed in Sec. 5-2, the rise time of the pressure wave used in the finite difference solution was quite small - being 2.1 microseconds for a frequency of 479 Hz.

The normalized gas temperature profiles, y vs z, computed for Run 213 are shown in Fig. 6-6. Notice that the oscillations in y are damped out at the outer boundary, $z = 2.75$; at which point the wall no longer has an influence

on the gas temperature. The gas temperature profiles are plotted in dimensional coordinates in Fig. 6-7. At the end of the cycle the gas temperature profile is as shown at $\tau = 0.99$. The boundary layer is compressed at $\tau = 0.001$ as the shock wave arrives. The pressure work is distributed throughout the boundary layer, causing the entire level of the gas temperature profile to rise. Since the wall temperature is fixed, a maximum in the gas temperature profile at $\tau = 0.001$ occurs 0.3×10^{-3} in. from the wall.

During the period of time between $\tau = 0.23$ and $\tau = 0.44$ gas temperature profiles are encountered which have the shape shown in Fig. 6-8. The shape is such that, although the gas temperature at the outer edge of the boundary layer is greater than the wall temperature, heat is transferred from the wall to the gas. If at this point in the cycle a heat transfer coefficient, h, is calculated based on the usual difference between the gas temperature at the outer edge of the boundary layer, T_∞, and the wall temperature, T_w, a negative value of h is obtained. It is immediately apparent that the driving force for heat transfer is not represented by $T_\infty - T_w$, but rather by $T_w - T_d$, as shown in Fig. 6-8. When the instantaneous heat transfer coefficients are calculated throughout the cycle it is found that h varies widely - attaining positive, negative, and infinite values at different points during the cycle. Since in the present solution the heat flux is obtained directly from the computed temperature profile, there is no need to introduce h;

therefore only heat flux rates are discussed.

In Fig. 6-7 there are several observations that can be made. The most noticeable is that the thermal boundary layer is thin - being less than 0.007 in. for this case. Notice that the outer boundary of the system, $x = x_\ell$, is a function of time. Since the value of z is fixed at the outer boundary, Eq. 5-20, along with the definition of z given in Eq. 5-12, yields

$$x_\ell = x_{\ell max} (P/P_0)^{-1/\gamma} \tag{6-1}$$

which specifies the motion of the outer boundary of the system. It can also be seen from Fig. 6-7 that, although the amplitude of the gas temperature fluctuation is small (50-75°F), the temperature gradients at the wall are large - approximately 0.4×10^6 °F/in. at $\tau = 0.001$. This large temperature gradient occurs because the temperature profile exhibits a maximum near the wall as was previously discussed.

6-3 EFFECT OF AVERAGE TUBE PRESSURE

In Fig. 6-9, Q_{pos} is plotted against P_r for three different average tube pressures, $\bar{P}$. Q_{pos} (see Fig. 4-5) is the amount of energy alternately being exchanged between the wall and the gas

$$Q_{pos} = \frac{1}{f}\int_0^{\tau_c} q_w \, d\tau \tag{4-8}$$

or since the net heat transferred per cycle is zero

$$Q_{pos} = \frac{1}{2f}\int_0^1 |q_w|\, d\tau \qquad (6\text{-}2)$$

The variation of the shape of the pressure wave from one run to another necessitated that an average pressure shape be used for the theoretical calculations at each of the three average tube pressure levels presented in Fig. 6-9. This variation from run to run accounts for some of the scatter in the experimental data. The average pressure shape that was used at each of the tube pressure levels is shown by the insert in Fig. 6-9. As can be seen, the variation in the average pressure shape was small.

The instantaneous heat flux, q_w, and Q_{pos} both increase as P_r and $\bar{P}$ increase. The increase in heat flux is caused by the increase in the rate at which pressure work is done on the gas. In the energy equation, Eq. 5-2, the pressure work is given by $(1/\rho)dP/dt$. Therefore, the pressure work is proportional to dP/dt. An increase in either P_r or $\bar{P}$ will increase the value of dP/dt and ultimately increase the heat flux because of the larger temperature gradients. The increase in dP/dt is apparent from Fig. 6-10a, in which the average pressure of the cycle is given by $\bar{P} = C_1\Delta P + P_0$, with ΔP being the amplitude of the oscillation. The constant, C_1, is only dependent on the shape of the pressure wave, and is therefore fixed when the pressure shape is fixed. When P_r is introduced into the above equation, P_0 is eliminated and the following expression results:

$$\Delta P = \bar{P} \left(\frac{1}{(P_r - 1)} + C_1 \right)^{-1} \qquad (6\text{-}3)$$

Equation 6-3 shows that an increase in P_r or $\bar{P}$ increases ΔP which results in an increase in dP/dt, as was shown in Fig. 6-10a.

The theoretical model agrees with the experimental data except at the lowest average tube pressure of 40 psia, where the experimental data lie above that predicted from the model. This difference is attributed to the departure of the flow near the center of the test plate from one-dimensional flow. A velocity component parallel to the wall would increase the heat flux to the wall. In order to lower the average tube pressure to 40 psia, it was necessary to use a plate gap thickness of 0.035 in. For a gap as large as this, the flow near the center of the test plate is affected by the exhausting air and departs from one-dimensional flow.

The dependence of the heat flux on the average tube pressure can be obtained from Eq. 5-25:

$$q_w = -T_0 \, f^{1/2} \, (k\rho c_p)^{1/2} \left(\frac{P}{P_0} \right) \left. \frac{\partial y}{\partial z} \right|_{z=0} \qquad (5\text{-}25)$$

which by substitution of $\rho_0 = P_0/(RT_0)$ becomes

$$q_w = -P_0^{1/2} \left(\frac{fkT_0 c_p}{R} \right)^{1/2} \left(\frac{P}{P_0} \right) \left. \frac{\partial y}{\partial z} \right|_{z=0} \qquad (6\text{-}4)$$

If the values of c_p, k, f, R, and T_0 are held constant in

Eq. 6-4

$$\frac{q_{w1}}{q_{w2}} = \left(\frac{P_{01}}{P_{02}}\right)^{1/2} \frac{\left[\frac{P}{P_0}\left.\frac{\partial y}{\partial z}\right|_{z=0}\right]_1}{\left[\frac{P}{P_0}\left.\frac{\partial y}{\partial z}\right|_{z=0}\right]_2} \tag{6-5}$$

Now, if γ, T_w, P_r, and the shape of the pressure wave are also constant, it follows that

$$\left[\frac{P}{P_0}\left.\frac{\partial y}{\partial z}\right|_{z=0}\right]_1 = \left[\frac{P}{P_0}\left.\frac{\partial y}{\partial z}\right|_{z=0}\right]_2 \tag{6-6}$$

When P_r and the pressure shape are constant, the P/P_0 distribution with time is constant and if, in addition, T_w, T_0, and γ are constant, the solution for y is fixed because the differential equation and the boundary conditions given by Eqs. 5-21 and 5-22 are fixed. Therefore, the solution for y is fixed and Eq. 6-6 is satisfied. Substitution of Eq. 6-6 into Eq. 6-5 gives

$$\frac{q_{w1}}{q_{w2}} = \left(\frac{P_{01}}{P_{02}}\right)^{1/2} \tag{6-7}$$

However, when P_r and the shape of the pressure wave are constant the minimum pressure in the cycle is proportional to the average pressure of the cycle

$$\frac{P_{01}}{P_{02}} = \frac{\bar{P}_1}{\bar{P}_2} \tag{6-8}$$

Therefore

$$\frac{q_{w1}}{q_{w2}} = \left(\frac{\bar{P}_1}{\bar{P}_2}\right)^{1/2} \tag{6-9}$$

which shows that the heat flux rate is proportional to the square root of the average tube pressure. It can also be shown that

$$\frac{Q_{pos1}}{Q_{pos2}} = \left(\frac{P_{01}}{P_{02}}\right)^{1/2} = \left(\frac{\bar{P}_1}{\bar{P}_2}\right)^{1/2} \tag{6-10}$$

Equation 6-10 is only approximately satisfied in Fig. 6-9 because a slightly different pressure shape was used at each of the three tube pressures. The pressure shape used for each set of runs is the average pressure shape for that set.

6-4 EFFECT OF FREQUENCY

The effect of frequency on Q_{pos} at an average tube pressure of 104 psia is shown in Fig. 6-11. In a manner completely analogous to that used in the previous section, Eq. 6-2 and Eq. 5-25 yield, for fixed T_w, T_0, P_0, k, c_p, γ, P_r, and pressure shape:

$$\frac{q_{w1}}{q_{w2}} = \left(\frac{f_1}{f_2}\right)^{1/2}, \quad \frac{Q_{pos1}}{Q_{pos2}} = \left(\frac{f_2}{f_1}\right)^{1/2} \tag{6-11}$$

An increase in the frequency increases the value of dP/dt as shown in Fig. 6-10b. As discussed in Sec. 6-3, an increase in dP/dt in Eq. 5-2 results in an increased heat flux. However, because of the decrease in the time available for the heat transfer per cycle at the higher frequencies, the value of Q_{pos} decreases with increasing frequency, as is apparent in Fig. 6-11.

6-5 EFFECT OF MASS FLOW RATE

In the theoretical model it was assumed that the fluid flow near the center of the test plate was one-dimensional and therefore independent of the average mass flow rate through the tube. The validity of this assumption was verified experimentally by taking a set of data runs at three different mass flow rates: 0.133, 0.276, 0.480 lb_m/sec - while frequency and average tube pressure were maintained constant. As shown in Fig. 6-12, Q_{pos} was experimentally found to be independent of the mass flow rate.

6-6 DISCUSSION OF THE ASSUMPTIONS IN THE THEORETICAL MODEL

For the range of variables used in this investigation, the boundary layer thickness was never greater than 0.020 in. This is small compared to the wavelength of the pressure oscillation which is 2.3 ft. at 479 Hz. Therefore, the assumption of a thin boundary layer that was used throughout this analysis is justified.

The thermal conductivity of the gas was taken to be constant in this analysis and was evaluated at the wall temperature. From the resulting solution it was found that the gas thermal conductivity deviation from that at the wall was never greater than 25 percent. The variation of the thermal conductivity can be approximately accounted for by use of a mean value between the thermal conductivity at the wall and the thermal conductivity at the outer edge of the boundary layer. Use of this mean value of the thermal conductivity changed the predicted heat flux at the wall by less than two percent. Therefore, the use of a constant thermal conductivity is a suitable approximation.

In the continuity equation only, the gas density was assumed to be independent of x and equal to the gas density at the outer edge of the boundary layer. This assumption yielded an approximate expression for the gas velocity, u, given by Eq. 5-8, which describes - at any given time - a linear velocity profile in x. Once the solution of the energy equation has been obtained through use of the u expression given by Eq. 5-8, that solution can be used to calculate a new u profile by integration of the continuity equation. That is

$$u(x,t) \simeq - \frac{1}{\rho(x,t)} \int_0^x \frac{\partial \rho}{\partial t} \, dx \qquad (6\text{-}12)$$

The u profile calculated by Eq. 6-12 is an approximate one since the values of ρ and $\partial\rho/\partial t$ used were obtained from an

approximate solution of the energy equation. In this manner, the u profile was obtained at several different times in the cycle and the results are shown in Figs. 6-13 and 6-14. The solid lines are the velocity profiles given by Eq. 5-8 and the dotted lines are the velocity profiles obtained from Eq. 6-12. From the figures it can be seen that at $\tau = 0.001$ and 0.04 the velocity profiles differ greatly while at $\tau = 0.12$, 0.35, and 0.75 the agreement is quite good. The density variation with x is greatest during the cycle at $\tau = 0.001$ as indicated by the large difference in the u profiles. Since the velocities are negative everywhere in the boundary layer, mass is being added to the boundary layer.

From the above discussion, it can be seen that for $\tau < 0.05$ the assumption of a density independent of x is a poor one while at later times the assumption is a good one. The importance of u in the solution of the energy equation, Eq. 5-2

$$c_p \rho \left(\frac{\partial T}{\partial t} + u \frac{\partial T}{\partial x}\right) = \frac{dP}{dt} + k \frac{\partial^2 T}{\partial x^2} \qquad (5\text{-}2)$$

depends on the magnitude of the $u\ \partial T/\partial x$ term compared to the magnitude of $\partial T/\partial t$. When the magnitudes of these two terms were calculated, it was found that there are only small regions of the boundary layer where $u\ \partial T/\partial x$ and $\partial T/\partial t$ are of the same order of magnitude. Outside these regions, $\partial T/\partial t$ is at least an order of magnitude larger

than u $\partial T/\partial x$. The inaccuracy of the values used for u at small times ($0 < \tau < 0.05$) does not have a significant effect on the solution of the energy equation as is confirmed by the fact that the model agrees reasonably well with the experimental data.

When the pressure ratio across the wave is very large or the gas temperature level is much greater than the wall temperature, there are substantial variations in the gas density in the thermal boundary layer. A large density variation would cause an expansion wave to be formed and dP/dx would not necessarily be zero as assumed in the present theoretical model. To account for the dP/dx variation, the momentum equation would have to be included.

For the case of a large net heat transfer at the wall, the continuity, momentum, and energy equations must be solved simultaneously. It has already been shown that when the continuity equation is solved separately from the energy equation to obtain an approximate expression for the velocity u, one is restricted to the case of a zero net heat transfer at the wall. In addition, when there is a net transfer of energy at the outer boundary of the system, the boundary condition there must be obtained by calculation of the upstream gas dynamic behavior. To further complicate the problem there may be some regimes in which the effects of turbulence are important.

These effects would be difficult to predict and one would probably have to resort to an empirical correlation.

6-7 SUMMARY OF CONCLUSIONS

This investigation has shown that for periodic shock-fronted pressure waves the instantaneous heat flux rates from the gas can be quite large, even when the net heat transferred to the surface is zero. The maximum heat flux in the cycle occurs immediately after the shock-front strikes the surface. For a short time thereafter the heat flux is greater than 40,000 BTU/hr-ft^2.

The rapid compression of the boundary layer by the arrival of the shock-front causes the temperature profile to have a maximum value within the thermal boundary layer a short distance from the wall. This temperature profile has a steep gradient at the wall of up to 2×10^6 °F/in., which results in a large heat flux there. Sinusoidal pressure waves would not result in such large heat flux rates. The lower rate of compression of the boundary layer would allow more time for heat conduction to occur in the gas, which would result in a smoother temperature profile with the peak eliminated. The temperature gradient, and consequently the heat flux, at the wall would be smaller with these sinusoidal pressure waves than with the shock-fronted pressure waves where the compression of the gas is more rapid.

The instantaneous heat flux was found to increase as the square root of the product of the frequency and the time-averaged pressure of the oscillation $[(f\bar{P})^{1/2}]$. The

heat flux also increased with an increase in the pressure ratio across the wave. These trends are explained by the increase in the rate at which pressure work is done on the gas in the boundary layer.

The present investigation has shown that there can be a large variation in the instantaneous heat flux rate at the surface when the net heat transferred at the surface is zero. The same would also be true when there is a large net heat transfer at the surface. Because the variation in the heat flux is large, any heat transfer analysis performed in such an oscillatory pressure environment should account for the instantaneous rates rather than accounting only for the time-averaged heat flux rates. It is apparent that additional investigations into the instantaneous heat flux rates would be helpful in understanding the heat transfer in oscillatory flows.

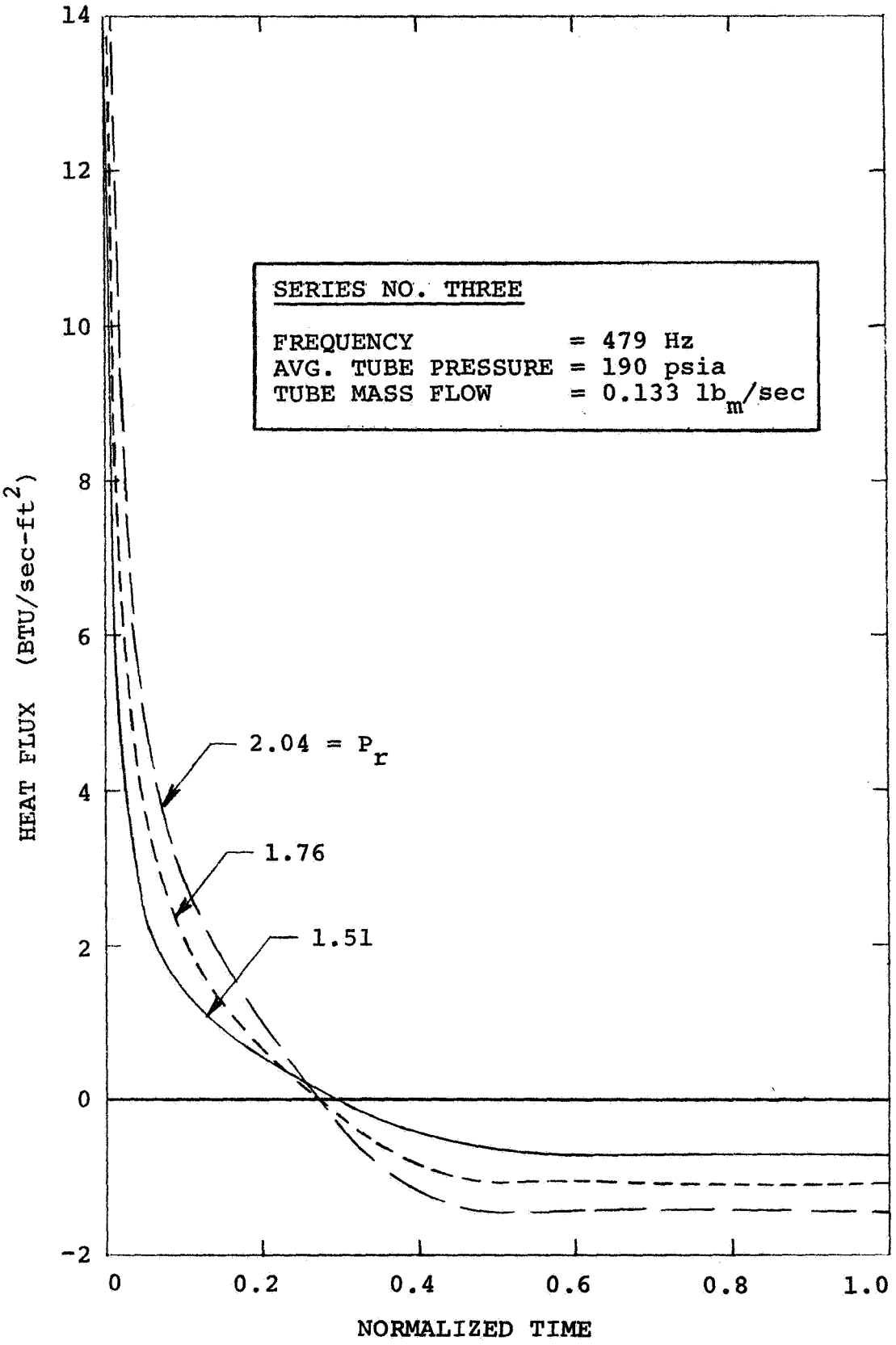

Fig. 6-1 Experimental Heat Flux Variation - Series No. Three

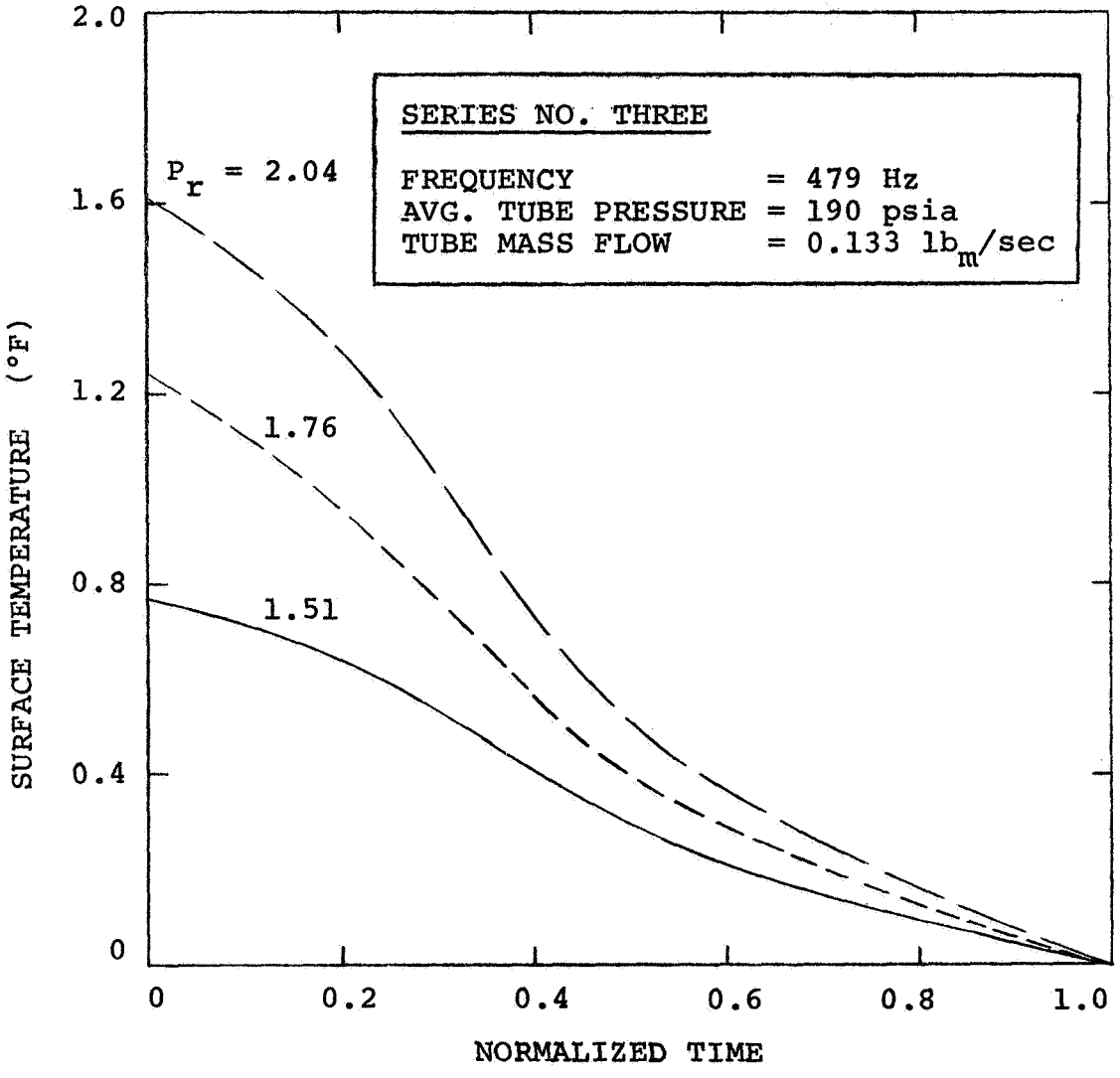

Fig. 6-2 Experimental Surface Temperature Oscillations - Series No. Three

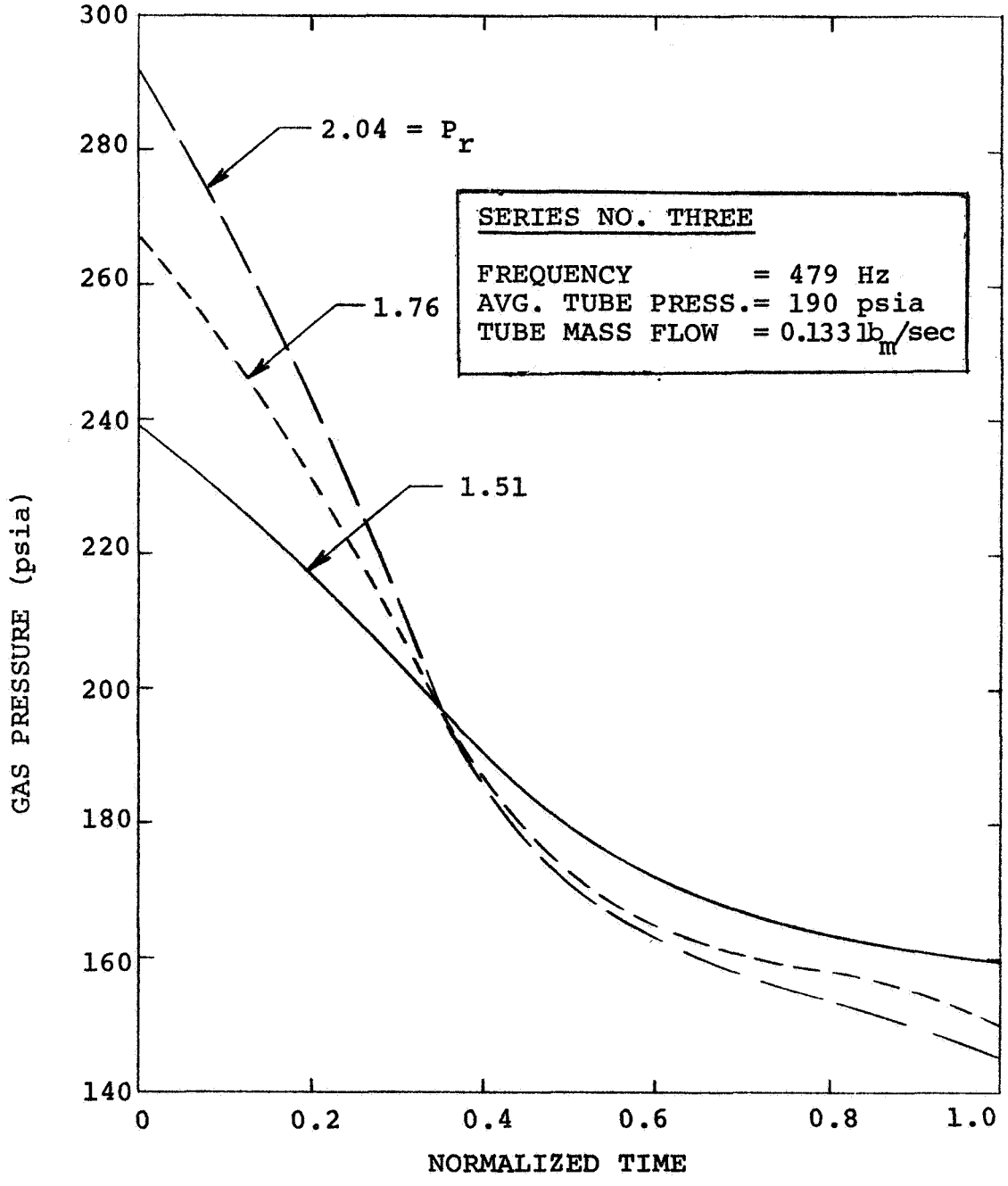

Fig. 6-3 Experimental Gas Pressure Oscillations - Series No. Three

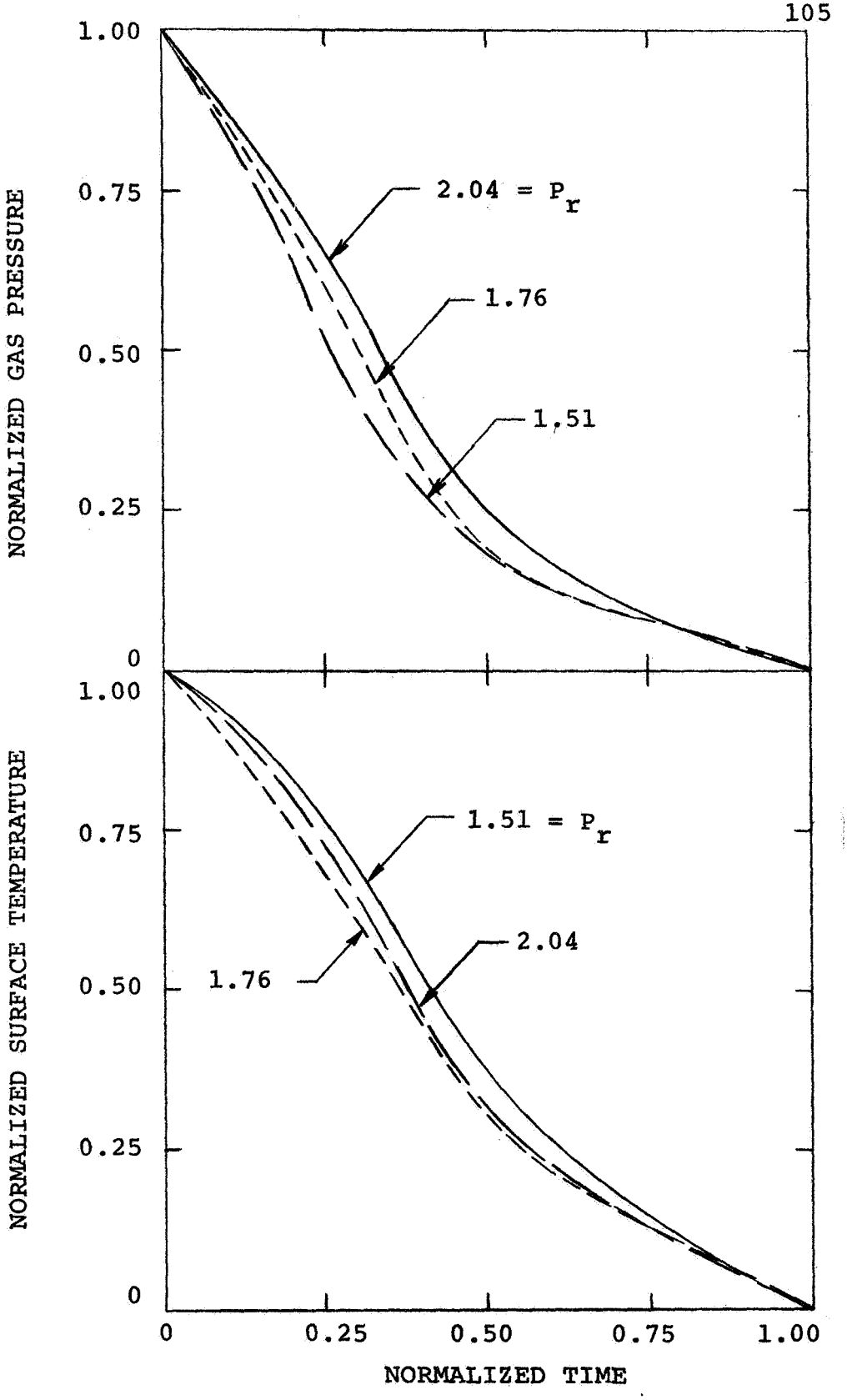

Fig. 6-4 Normalized Gas Pressure and Surface Temperature Oscillations - Series No. Three

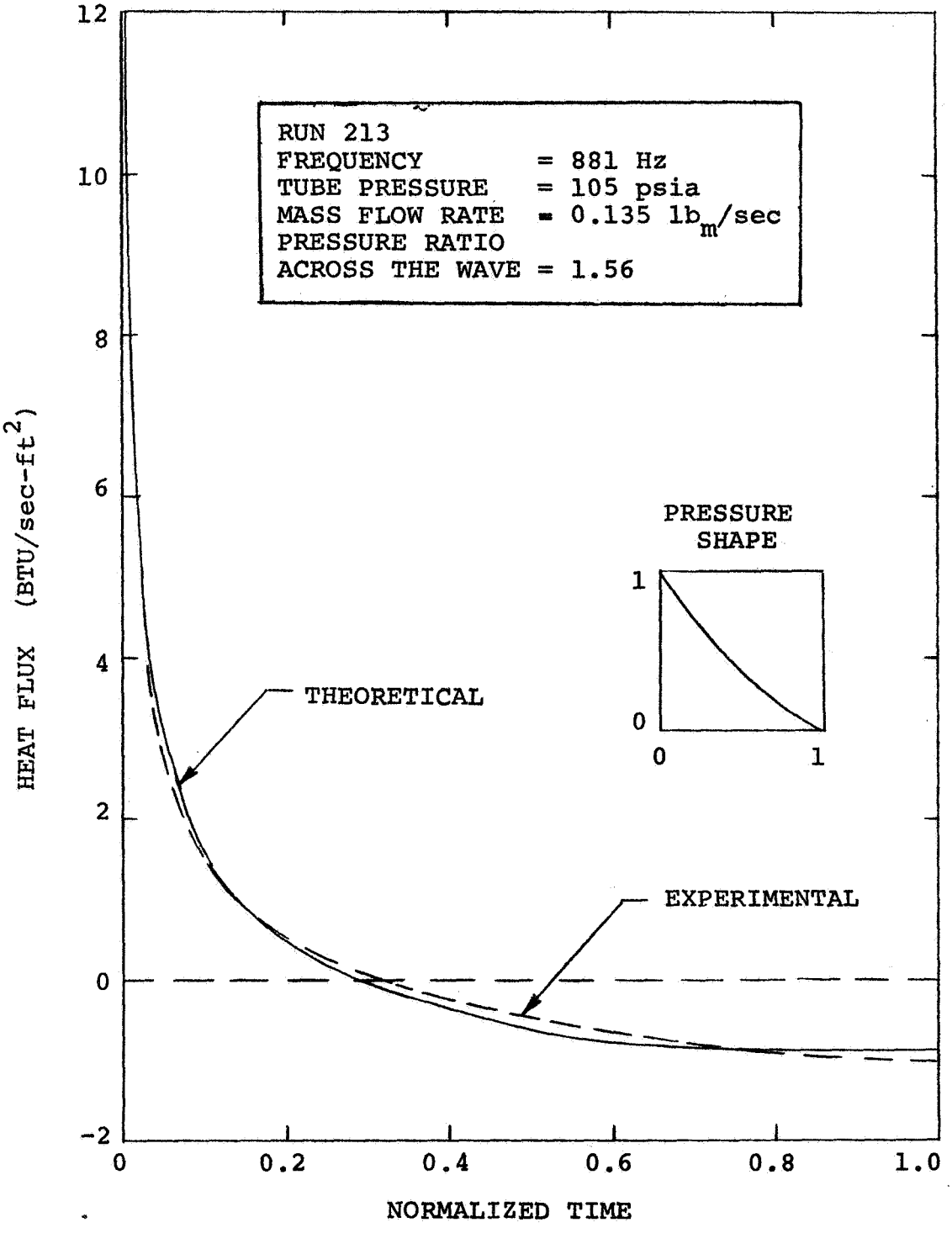

Fig. 6-5 Heat Flux Variation - Comparison of Theoretical Model with Experimental Results - Run 213

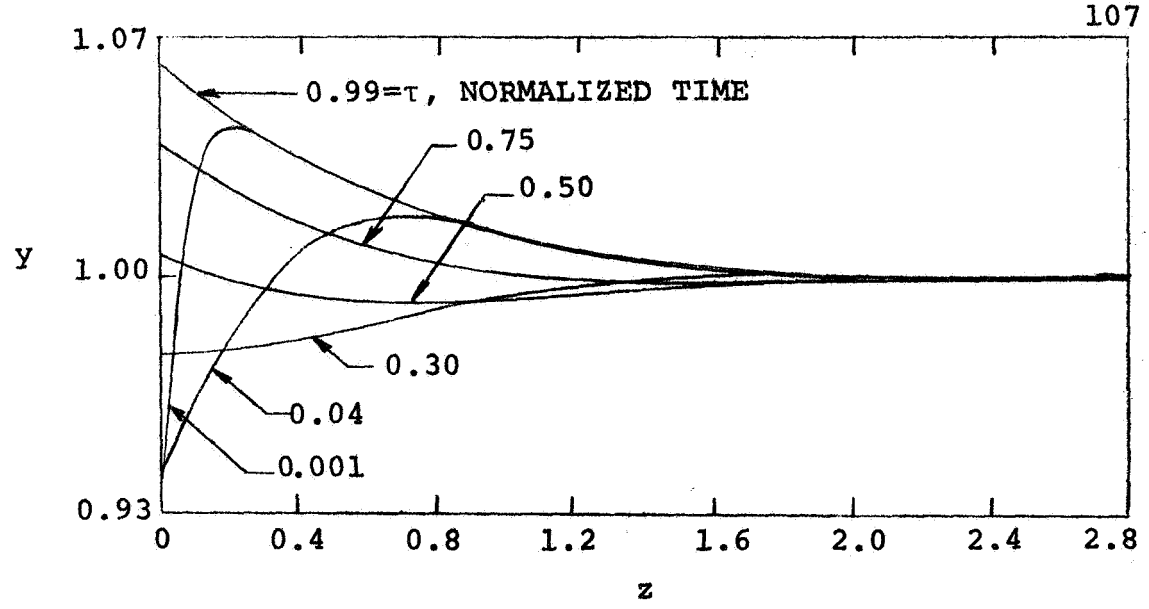

Fig. 6-6 Predicted y vs z Profiles - Run 213

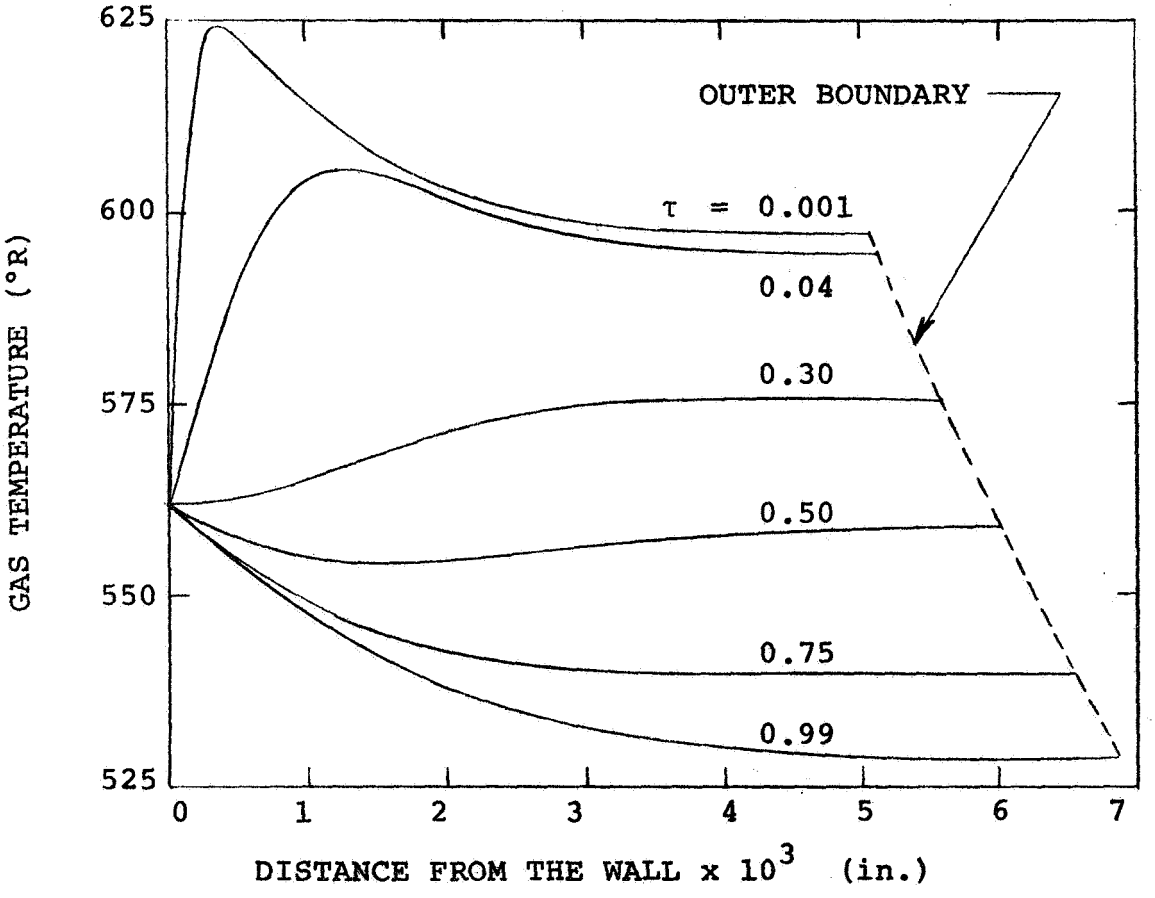

Fig. 6-7 Predicted Gas Temperature Profiles - Run 213

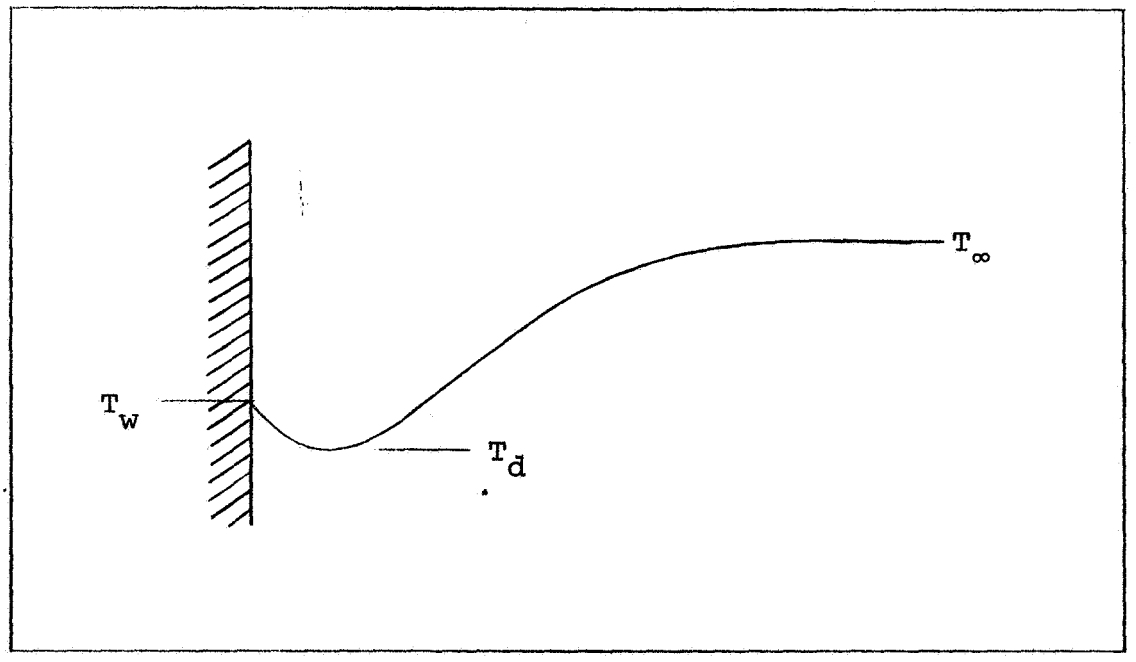

Fig. 6-8 Gas Temperature Profile Which Results in A Negative Heat Transfer Coefficient

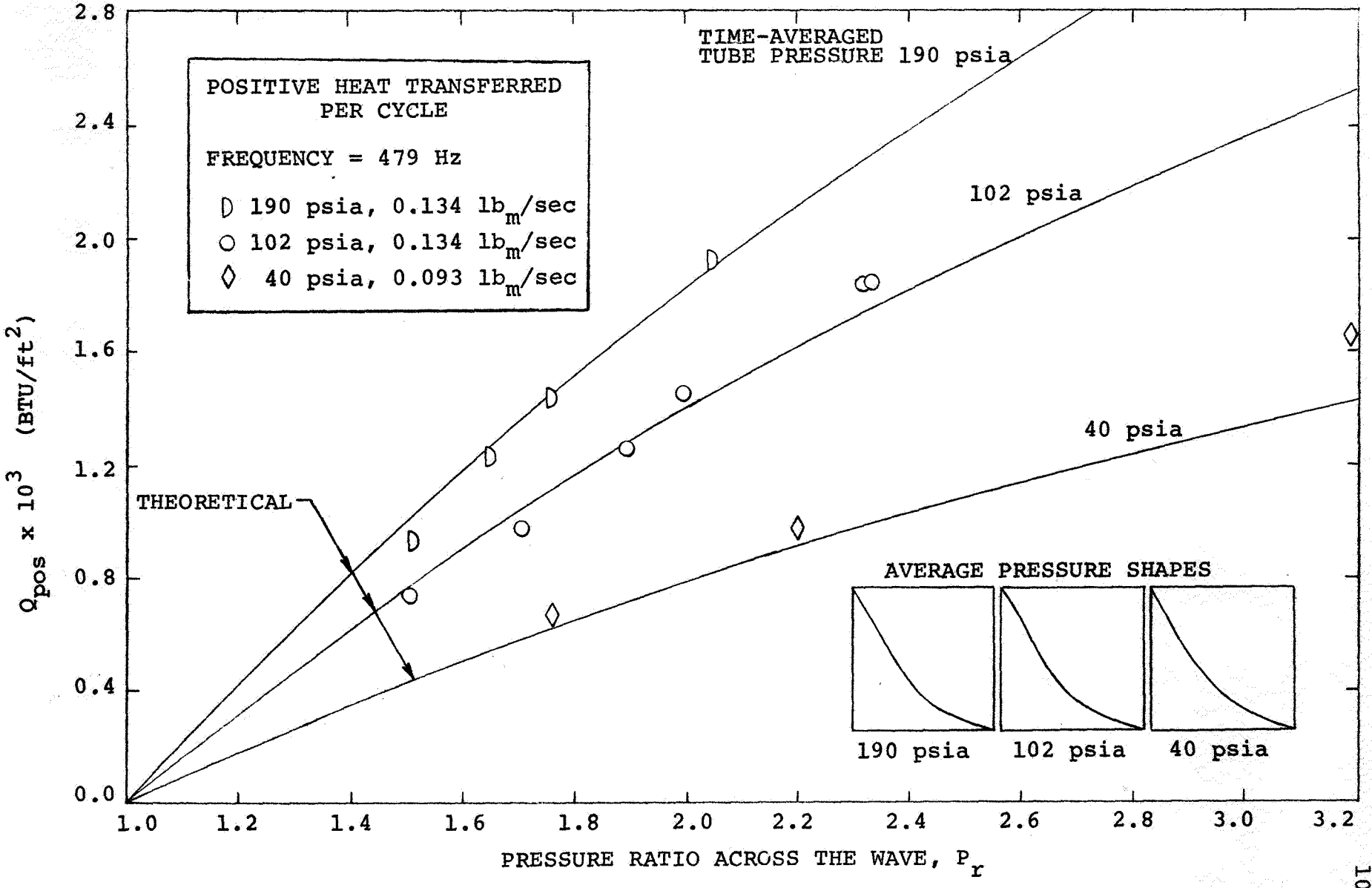

Fig. 6-9 Positive Heat Transferred Per Cycle at Three Different Tube Pressures

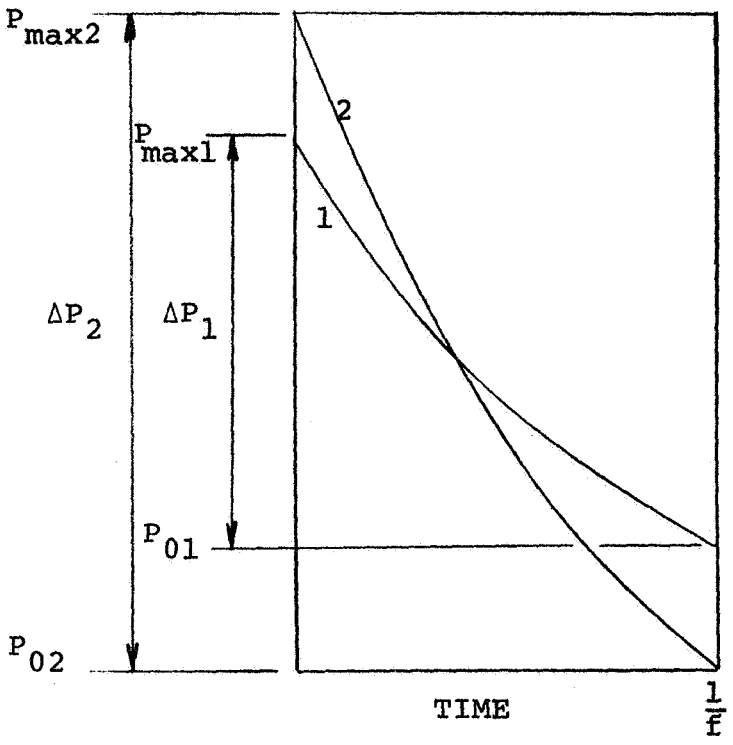

(a)

$$\Delta P = \bar{P}\left(\frac{1}{(P_r - 1)} + C_1\right)^{-1}$$

WHEN $\bar{P}_1 > \bar{P}_2$; P_r, f, & SHAPE ARE FIXED

OR $P_{r2} > P_{r1}$; $\bar{P}$, f, & SHAPE ARE FIXED

THEN

$\Delta P_2 > \Delta P_1$

AND

$$\left.\frac{dP}{dt}\right|_2 > \left.\frac{dP}{dt}\right|_1$$

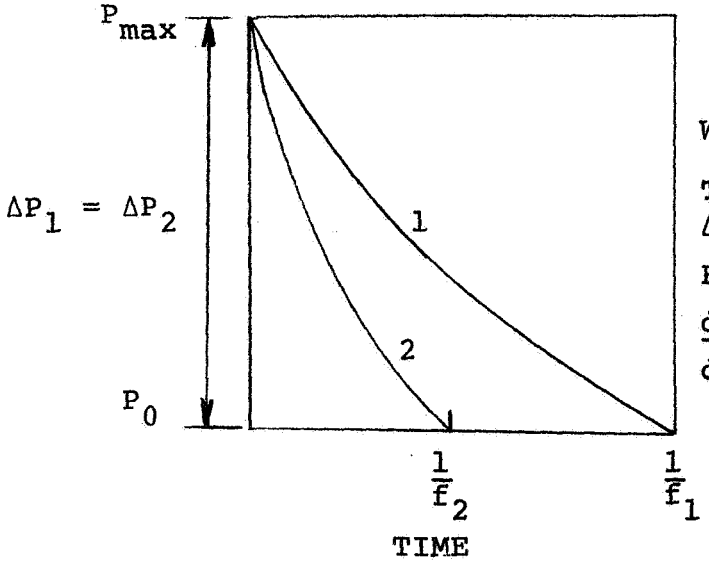

(b)

WHEN $f_2 > f_1$; P_r, $\bar{P}$, & SHAPE ARE FIXED

THEN

$\Delta P_2 = \Delta P_1$

BUT

$$\left.\frac{dP}{dt}\right|_2 > \left.\frac{dP}{dt}\right|_1$$

Fig. 6-10 Illustration for dP/dt Increase With $\bar{P}$, P_r, and f

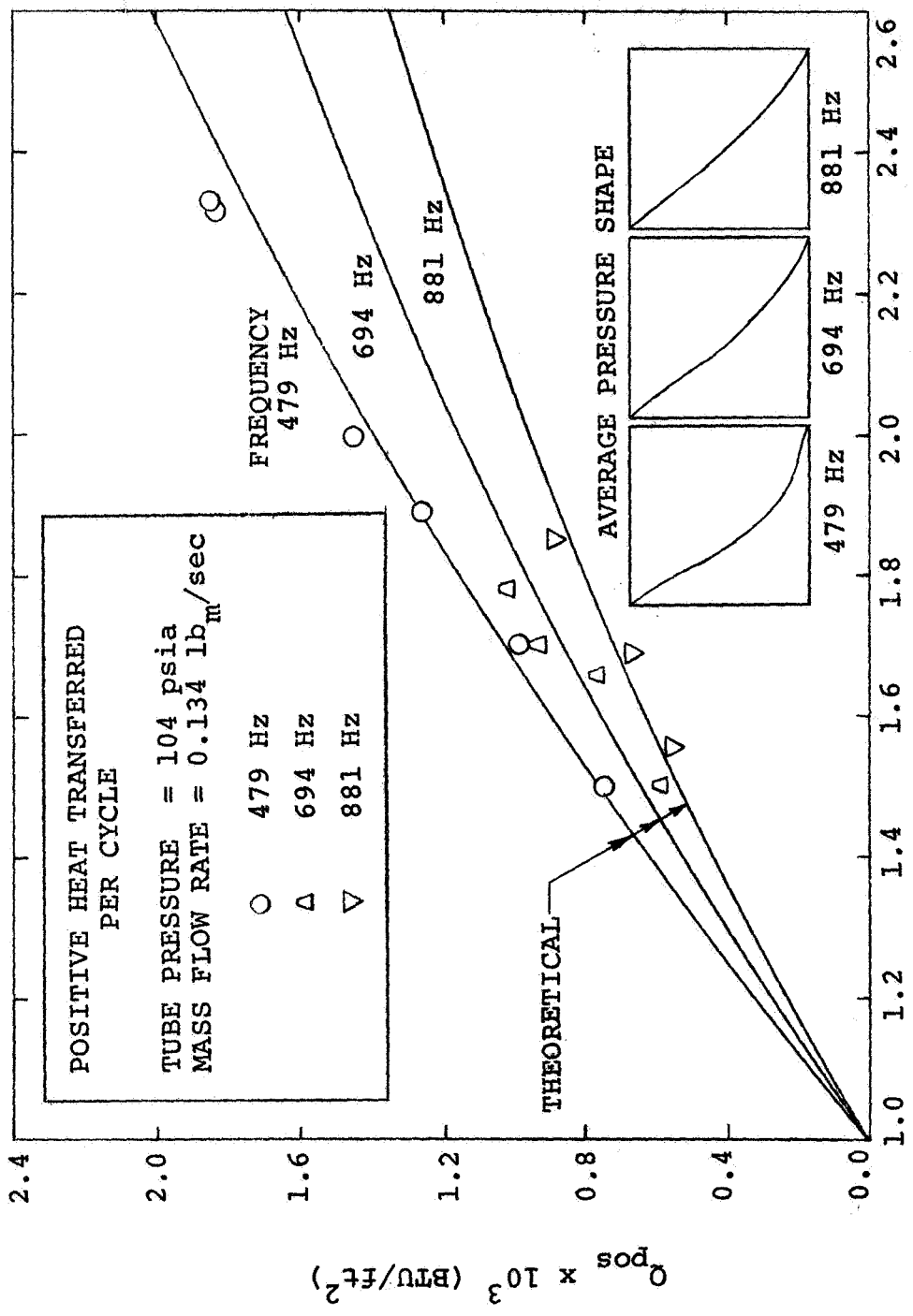

Fig. 6-11 Positive Heat Transferred Per Cycle at Three Different Frequencies

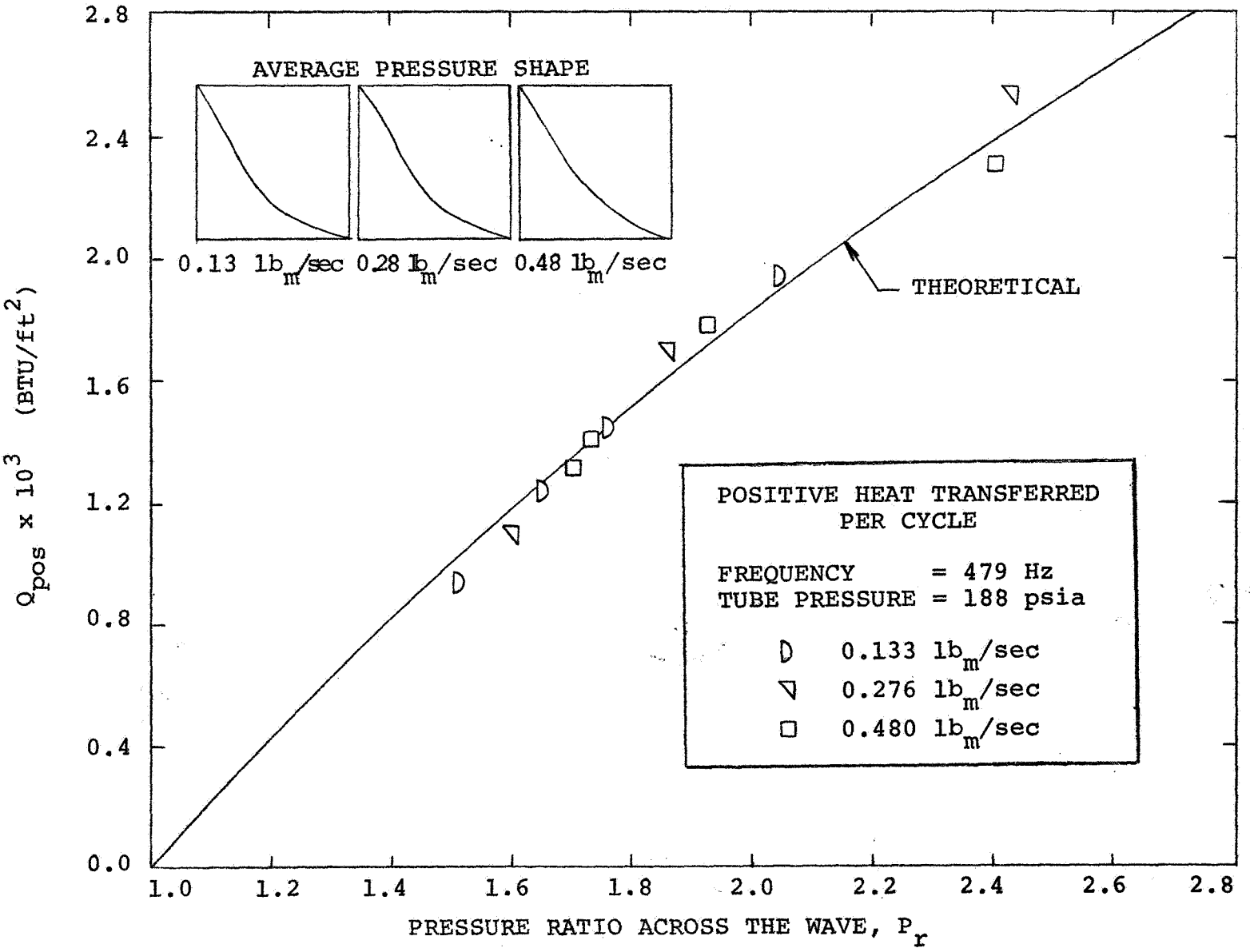

Fig. 6-12 Positive Heat Transferred Per Cycle at Three Different Tube Mass Flow Rates

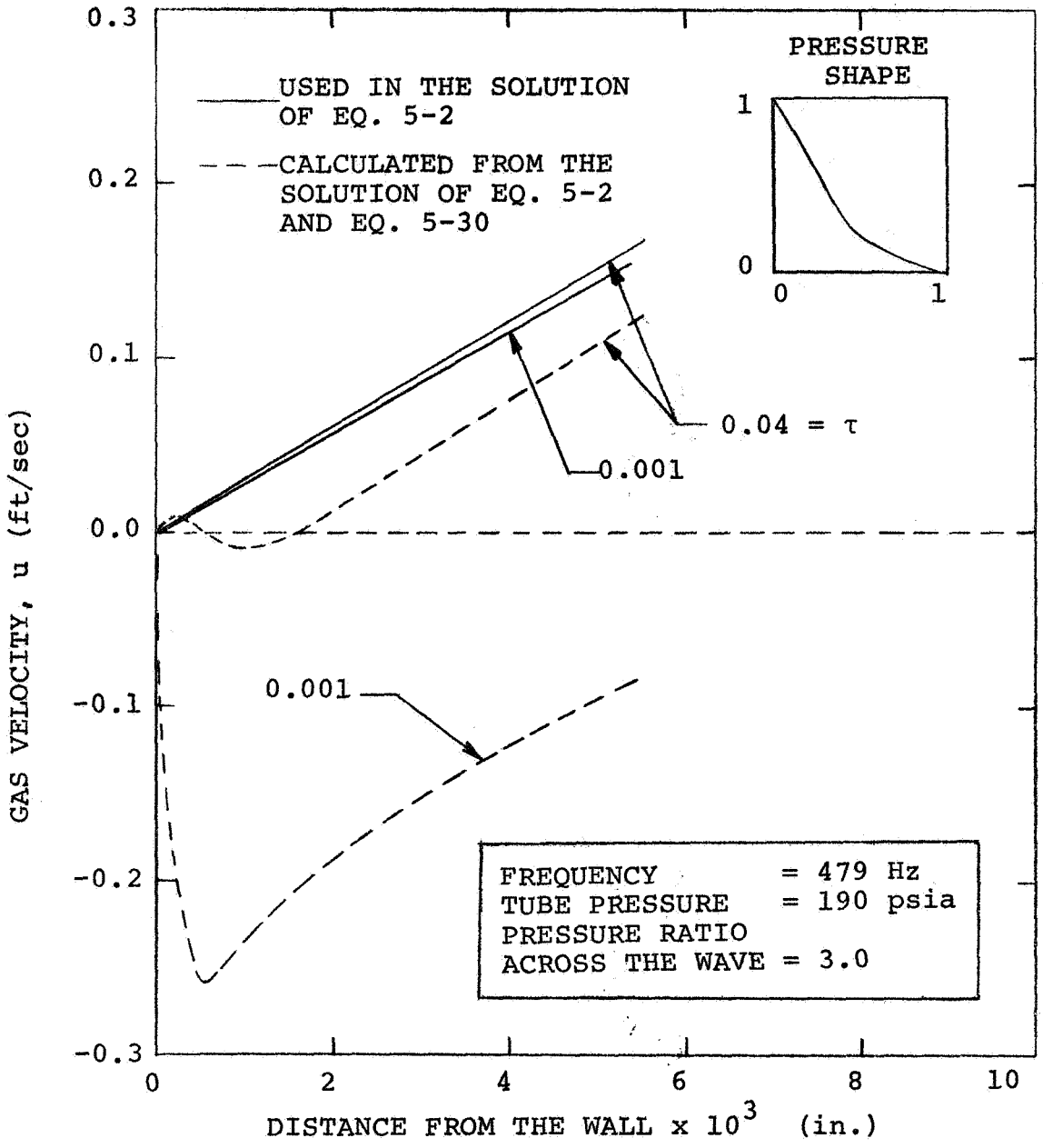

Fig. 6-13 Gas Velocity Profiles at τ = 0.001 and 0.04

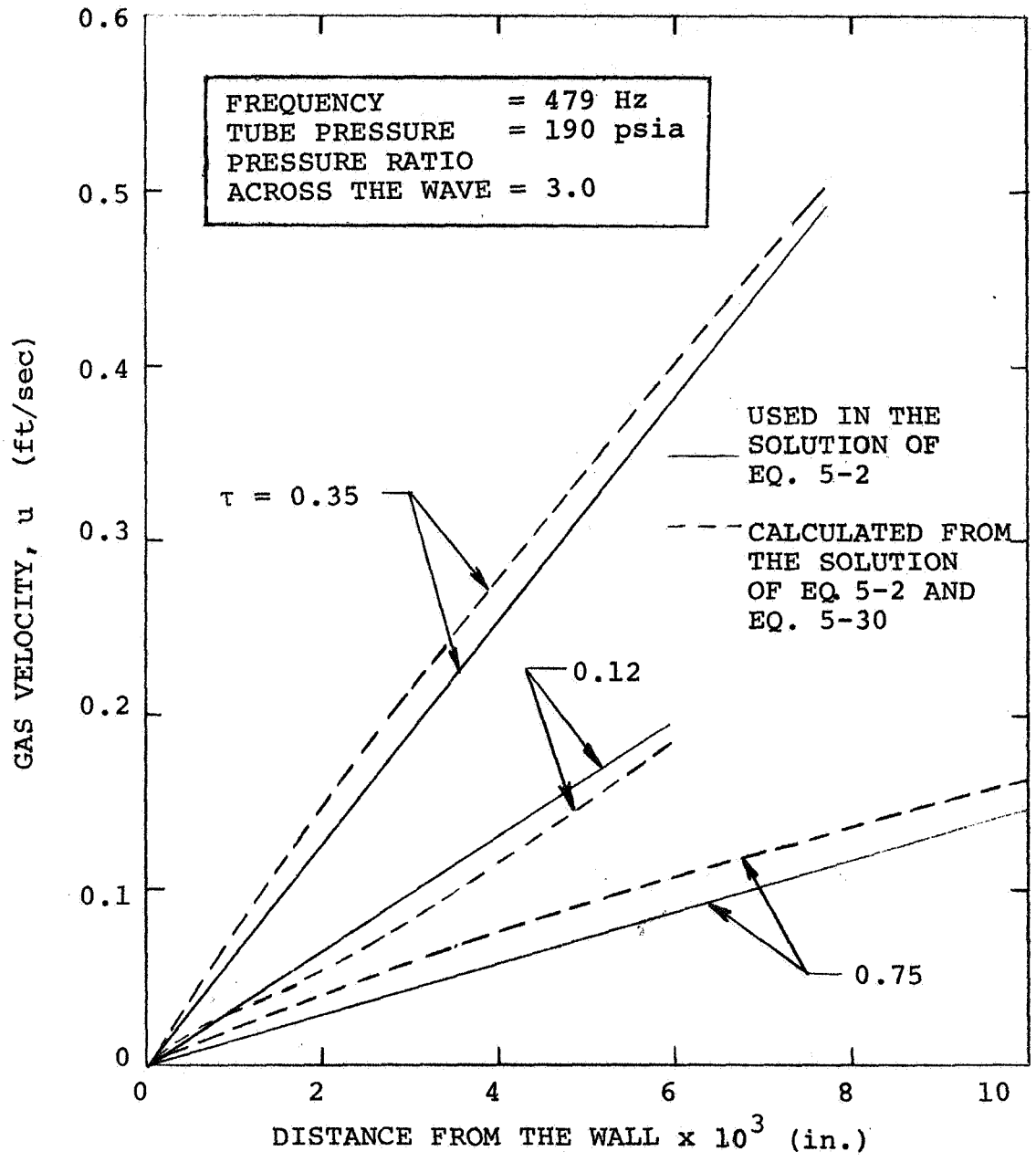

Fig. 6-14 Gas Velocity Profiles at τ = 0.12, 0.35, and 0.75

CHAPTER SEVEN

RECOMMENDATIONS FOR FUTURE INVESTIGATIONS

As was discussed in Chapter Six, the theoretical model is only applicable to the case in which the net heat transferred to the wall is zero. The minimum gas temperature, T_0, was chosen so that this condition was satisfied. However, in many cases of practical interest T_0 is much larger than the wall temperature, causing a net amount of heat to be transferred to the wall. It is therefore recommended that a second generation investigation be performed with this apparatus wherein a substantial temperature difference is maintained between the wall temperature and the oscillating gas temperature. This would necessitate heating the air and developing a heat flux gauge which could accurately measure the absolute value of the heat flux oscillations. The heat flux gauge used in the present investigation could only accurately measure the fluctuating portion of the heat flux shown in Fig. 4-4. Since the governing differential equations for the gas are nonlinear, the problem cannot be divided into a fluctuating and a non-fluctuating portion, and each solved independently. Therefore, a modified theoretical model must be developed for the case where a net amount of heat is transferred at the wall as discussed in Sec. 6-6.

In the present experimental apparatus there are several other types of flow conditions where instantaneous heat flux measurements could be made. The present investigation was undertaken at position A in Fig. 7-1, where the longitudinal pressure waves are normal to the surface - as are the fluid velocity fluctuations. The effects of velocity components parallel to the surface could be determined at a position B, located near the air gap. It would be expected that the velocity component parallel to the wall would increase the heat flux above that obtained at position A where this velocity component is zero.

As was previously mentioned, Harrje and others at Princeton have studied the mechanism by which heat is transferred to the tube wall in the presence of high frequency, steep-fronted pressure waves. Their investigations were concerned only with the time-averaged heat flux rates. An investigation of the instantaneous heat flux rates at the tube wall, such as at position C in Fig. 7-1, would complement Princeton's study.

The effect of pressure oscillations on instantaneous mass transfer rates is of great interest to those concerned with rocket combustion instability. In the present investigation it has been shown that the arrival of the shock-front causes extreme temperature gradients at the wall - with the gas temperature profile reaching a maximum value at a point inside the thermal boundary layer, such as occurs

at $\tau = 0.001$ and 0.04 in Fig. 6-7. A temperature profile such as this would have a considerable effect on the instantaneous mass transfer, which would not be predicted by a quasi-steady type analysis. The present apparatus can provide the environment for the instantaneous mass transfer studies needed in this most challenging area.

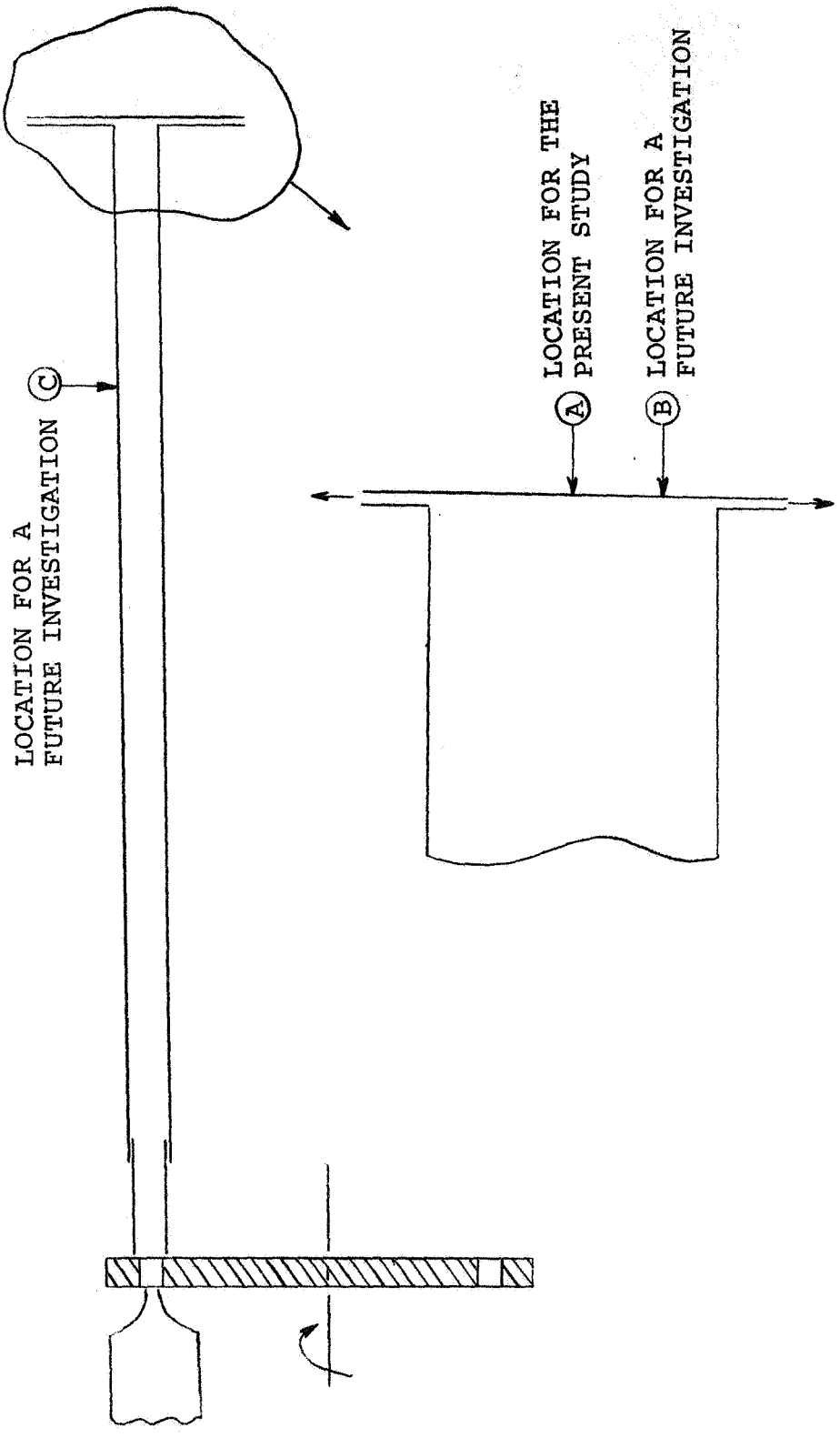

Fig. 7-1 Possible Locations for Future Investigations with the Apparatus

BIBLIOGRAPHY

Ames, W.F. Nonlinear Partial Differential Equations in Engineering. New York: Academic Press, 1965.

Barrere, M., Jaumotte, A., DeVeubeke, B.F., and Vandenkerckhove, J. Rocket Propulsion. New York: Elsevier Publishing Co., 1960.

Baumeister, Theodore (ed.). Marks' Mechanical Engineers' Handbook. 6th ed., New York: McGraw-Hill Book Co., 1958, p. 5-106.

Bayley, F.J., Edwards, P.A., and Singh, P.P. "The Effect of Flow Pulsations on Heat Transfer by Forced Convection from a Flat Plate," International Developments in Heat Transfer, 1961-62, pp. 499-509.

Bendersky, D. "A Thermocouple for Measuring Transient Temperatures," Mechanical Engineering, Vol. 75, No. 2, Feb. 1953, pp. 117-121.

Bennethum, J.E. Heat Transfer and Combustion Chamber Deposits in a Spark Ignition Engine. Ph.D. thesis, University of Wisconsin, 1960.

Berman, K. and Cheney, S.H. "Combustion Studies in Rocket Motors," Journal of the American Rocket Society, Vol. 23, No. 2, 1953, p. 89.

Bogdan, L. High-Temperature, Thin-Film Resistance Thermometers for Heat Transfer Measurement. NASA CR-26, April 1964.

Bogdanoff, D.W. A Study of the Mechanisms of Heat Transfer in Oscillating Flow. Princeton University Dept. of Aerospace and Mechanical Sciences Technical Report 483f, Oct. 1967.

Bollinger, L.E., Goldsmith, M., and Lemmon, A.W. Jr. (ed.). Liquid Rockets and Propellants. Progress in Astronautics and Rocketry, Vol. 2. New York: Academic Press, 1960.

Bruce, G.H., Peaceman, D.W., Rachford, H.H., and Rice, J.D. "Calculation of Unsteady-State Gas Flow Through Porous Media," Journal of Petroleum Technology, Trans. AIME, Vol. 198, 1953, p. 79.

Bushing, J.R., and Clarke, J.F. "Shock Reflection and Surface Effects in the Shock Tube," Recent Advances in Aerothermochemistry, (I. Glassman, ed.), Vol. 1, 1967, pp. 165-190.

Chalitbhan, V. Effect of Longitudinal Pulsations on Heat Transfer. Ph.D. thesis, University of Texas, Jan. 1959.

Chao, B.T. "End-Wall Heat Transfer in a Rarefaction Wave Tube," Journal of Heat Transfer, Trans. ASME, Series C, Vol. 87, 1965, pp. 349-352.

Clarke, J.F. On the Problem Involving Heat Conduction Through a Polyatomic Gas. The College of Aeronautics, Cranfield, Great Britain, Rept. No. 149, May 1961, AD 260624.

Crank, J., and Nicolson, P. "A Practical Method for Numerical Evaluation of Solutions of Partial Differential Equations of the Heat Conduction Type," Proceedings of the Cambridge Philosophical Society, Vol. 43, 1947, pp. 50-67.

Crocco, L., and Harrje, D.T. "Combustion Instability in Liquid Propellant Rocket Motors," Experimental Methods in Combustion Research (J. Surugue, ed.), Section 3.4. New York: Pergamon Press for AGARD, 1964.

Douglas, J., Jr., and Jones, B.F., Jr. "On Predictor-Corrector Methods for Nonlinear Parabolic Differential Equations," Journal for Industrial and Applied Mathematics, Vol. 11, 1963, p. 195.

Eastwood, I., Jackson, T.W., Oliver, C.C. and Purdy, K.R. Heat Transfer Threshold Values for Resonant Acoustic Vibrations in a Horizontal Isothermal Tube. Aeronautical Research Laboratories Report No. ARL-62-326, April 1962.

Feiler, C.E., and Yeager, E.B. Effect of Large-Amplitude Oscillations on Heat Transfer. NASA TR-142, 1962.

Frieman, H.S., and Fay, J.A. Heat Transfer from Argon and Xenon to the End-Wall of a Shock Tube. Fluid Mechanics Lab, Dept. of M.E., M.I.T., May 1965, AD 617055.

Hackemann, P. Method for Measuring Rapidly Changing Surface Temperatures and Its Application to Gun Barrels. British Theoretical Research Tr. 1/46, Armament Research Dept.

Hall, J.G., and Hertzberg, A. "Recent Advances in Transient Surface Temperature Thermometry," Jet Propulsion, Nov. 1958, pp. 719-723.

Harrje, D.T. Heat Transfer in Oscillating Flow, Progress Report for the Period Oct. 1959 to 30 Sept. 1960. Princeton University Aeronautical Engineering Report No. 483b, AD 249670.

Harrje, D.T. Heat Transfer in Oscillating Flow - Final Report, Princeton University Dept. of Aerospace and Mechanical Sciences Technical Report 483g, Oct. 1967, AD 664303.

Harrje, D.T., and Crocco, E.J. Heat Transfer in Oscillating Flow, Progress Report for the Period 1 July 1959 to 1 Oct. 1959, Princeton University Aeronautical Engineering Report No. 483, Ad 235083.

Hartunian, R.A., Russo, A.L., Marrone, P.V. Boundary Layer Transition and Heat Transfer in Shock Tubes. CAL Rept. No. AD1118-A-3, Dec. 1959, AD234728.

Hwu, C. The Effect of Vibration on Forced Convective Heat Transfer. Ph.D. thesis, University of Cincinnati, 1959.

Jackson, T.W., Harrison, W.B., and Boteler, W.C. "Free Convection, Forced Convection, and Acoustic Vibrations in a Constant Temperature Vertical Tube," Journal of Heat Transfer, Trans. ASME, Series C, Vol. 83, 1959, pp. 68-74.

Jackson, T.W., and Johnson, H.L. Convective Flow Due to Acoustic Vibrations in Horizontal Resonant Tubes. Georgia Institute of Technology, Final Report, Contract No. AF 49(638)-459, March 1961.

Jackson, T.W., Oliver, C.C., and Eastwood, I. The Effects of Resonant Vibrations on Heat Transfer at High Reynolds Numbers. UCRL-13016, Dec. 1961.

Jackson, T.W., Purdy, K.R., Keith, H.G., and Rudland, R.S. Investigations of the Effect of Acoustic Vibrations on Convective Heat Transfer - Final Report. Aerospace Research Laboratories Rept. No. ARL 65-97, 1965.

Jackson, T.W., Purdy, K.R., and Oliver, C.C. "The Effects of Resonant Acoustic Vibrations on the Nusselt Number for a Constant Temperature Horizontal Tube," International Developments in Heat Transfer, 1961-1962, pp. 483-489.

Jackson, T.W., Purdy, K.R., Oliver, C.C., and Johnson, H.L. The Effects of Resonant Acoustic Vibrations on the Local and Overall Heat Transfer Coefficient for Air Flowing Through an Isothermal Horizontal Tube. Aeronautical Research Laboratories, ARL Technical Report 60-322, 1960.

Kudryavtsev, Y.V., et al. Unsteady State Heat Transfer. London: Iliffe Books Ltd., 1966.

Lauver, M.R. Evaluation of Shock-Tube Heat-Transfer Experiments to Measure Thermal Conductivity of Argon from 700° to 8600°K. NASA TN D-2117, Feb. 1964.

Levy, M.J., and Potter, J.H. "Some Transient Measurements in a Rarefaction Wave Tube," Journal of Engineering for Industry, Trans. ASME, Series B Vol. 86, 1964, pp. 365-370.

Marec, J.P., and Harrje, D.T. Heat Transfer in Oscillating Flow. Progress Report for the Period to 30 June 1963. Princeton University Aeronautical Engineering Report No. 483e, AD 421188.

Miller, H.R. Heat Transfer Techniques and Measurements in the Douglas Aerophysics Laboratory Hypervelocity Impulse Tunnel. Douglas Rept. SM-43066, Dec. 1964, AD 616924.

Overbye, V.D. Variation of Instantaneous Wall Temperature, Heat Transfer, and Heat Transfer Coefficients in a Spark Ignition Engine. Ph.D. thesis, University of Wisconsin, 1960.

Peng, T., and Ahtye, W.F. Experimental and Theoretical Study of Heat Conduction for Air up to 5000°K. NASA TN D-687, Feb. 1961.

Pless, L.G. The Effect of Selected Operating Variables on Instantaneous Combustion-Chamber Surface Temperature. M.S. thesis, University of Wisconsin, 1956.

Priem, R.J., and Guentert, D.C. Combustion Instability Limits Determined by a Non-Linear Theory and a One-Dimensional Model. NASA TN D1409, Oct. 1962.

Purdy, K.R., Jackson, T.W., and Gorton, C.W. "Viscous Fluid Flow under the Influence of a Resonant Acoustic Field," Journal of Heat Transfer, Trans. ASME, Series C, Vol. 86, 1964, pp. 97-106.

Roark, R.J. Formulas for Stress and Strain. New York: Mc Graw-Hill, 4th ed., 1965, p. 366.

Saunders, R.C., and Harrje, D.T. Heat Transfer in Oscillating Flow, Progress Report for the Period 1 Oct. 1960 to 30 Sept. 1961. Princeton University Aeronautical Engineering Report No. 483c, AD 273274.

Saunders, R.C., and Harrje, D.T. Heat Transfer in Oscillating Flow, Princeton University Aeronautical Engineering Report No. 483d, 1 July 1963, AD 413452.

Skinner, G.T. A New Method of Calibrating Thin Film Gauge Backing Materials. Rept. No. CAL-105, June 1962, AD 282409.

Smith, G.D. Numerical Solution of Partial Differential Equations. London: Oxford University Press, 1965.

Spurlock, J.M., Jackson, T.W., Purdy, K.R., Oliver, C.C., and Johnson, H.L. The Effects of Resonant Acoustic Vibrations on Heat Transfer to Air in Horizontal Tubes, WADC Technical Note 59-330, June 1959.

Sutton, G.P. Rocket Propulsion Elements. 3rd ed., New York: John Wiley & Sons, 1963.

Timoshenko, S., and Woinowsky-Krieger, S. Theory of Plates and Shells. 2nd ed., New York: McGraw-Hill, 1959.

Timoshenko, S., and Young, D.H. Vibration Problems in Engineering. 3rd ed., New York: D. VanNostrand Co., Inc., 1955, pp. 450-458.

Victory Engineering Corp. Veco Å Thinistors, Product Bulletin MFN172, 1967.

Vidal, R.J. Model Instrumentation Techniques for Heat Transfer and Force Measurements in a Hypersonic Shock Tunnel, CAL Rept. No. AD-917-A-1, Feb. 1956, AD 97238.

Vidal, R.J. "Transient Surface Temperature Measurements," ASME Symposium on Measurement in Unsteady Flow, May 1962, pp. 90-99.

Vidal, R.J. Transient Surface Temperature Measurements, CAL Rept. No. 114, March 1962, AD 275818.

Wendland, D.W. The Effect of Periodic Pressure and Temperature Fluctuations on Unsteady Heat Transfer in a Closed System. Ph.D. thesis, University of Wisconsin, 1968.

Zucrow, M.J., and Osborn, J.R. "An Experimental Study of High Frequency Combustion Pressure Oscillations," Jet Propulsion, Vol. 28, No. 10, Oct. 1958, p. 654.

Zucrow, M.J., Osborn, J.R., and Pinchak, A.C. "Luminosity and Pressure Oscillations Observed with Longitudinal and Transverse Modes of Combustion Instability," Journal of the American Rocket Society, Vol. 30, No. 8, Aug. 1960, pp. 758-761.